LIST OF FIGURES

LIST OF TABLES

CHAPTER 1

INTRODUCTION

CHAPTER 1

INTRODUCTION

1.1 Background

Al-Si casting alloys are widely used in several industrial applications due to their outstanding properties such as high fluidity, low shrinkage, high corrosion resistance, good weldability, easy brazing, and low coefficient of thermal expansion (CTE) [1-3]. The elevated content of Si in these alloys, giving hypereutectic casting alloy types, enhances the wear resistance at the expense of machinability. The hypereutectic Al-Si alloys are used extensively in automotive applications, which require high wear resistance and excellent thermal shock resistance, such as engine block, pistons, brake rotors, and cylinder liners [4-5].

The solidification sequences of hypereutectic Al-Si alloys begin by the precipitation of primary Si particles, followed by the formation of α-Al in dendritic morphology, and then end by eutectic precipitation. In eutectic reactions, eutectic Si and α-Al as well as β-Al_5FeSi phases precipitate first then θ-Al_2Cu and Mg_2Si phases form in the last solidification stage, below a temperature of 510 °C [6]

The presence of primary Si particles in hypereutectic Al-Si alloys enhances their wear resistance and hardness properties at the expense of the tensile properties. Many studies [7-10] have been proposed that the applying of grain refinement and high cooling rate can refine the size and the morphology of the primary Si particles, and thus improve the overall mechanical properties.

Increasing Mg content in hypereutectic Al-Si alloys gives new hypereutectic Al-Si-Mg alloying system having superior potential for wear resistance. These alloys can also be considered as *in-situ* aluminum matrix composites containing a large amount of Mg_2Si particles and seem to be potential candidates to replace hypereutectic Al-Si alloys in engine block applications. Such Al-Si-Mg alloys show high reliability as automobile brake disc materials due to the presence of the Mg_2Si reinforcement characterized by high melting point (1085 ^{o}C), low density (1.99 x 10^{3}kg m^{-3}), high hardness of 4.5 x 10^{9} N m^{-2}, low thermal expansion coefficient (7.5 x 10^{-6} K^{-1}), and a reasonably high elastic modulus (120 GPa) [8].

The microstructures of hypereutectic Al-Si-Mg alloys with high Mg content are essentially composed of two components: (i) primary Mg_2Si particles and (ii) the Al-Si-Mg_2Si ternary eutectic. Adding of 4.5% Copper to these alloys leads to the precipitation of θ-Al_2Cu and Q-$Al_5Mg_8Cu_2Si_6$ intermetallic compounds [9]. When Mg is present together with iron, there is an increased tendency for the π-$Al_8Mg_3FeSi_6$ Chinese script phase to form [10].

Conventional metal casting processes encounter many potential problems. These include gas entrapment, hot cracking, and shrinkage porosity formation. Hot tearing occurs during the solidification stage as a result of tensile strain in a weak material region (hot spot region) just above the solidus temperature [11]. Shrinkage porosity may form due to the reduced feedability of liquid metal through the dendritic network. In order to overcome some of these drawbacks associated with these conventional casting techniques, a semi-solid metal processing technique has been developed.

Semi-solid metal processing has been used for about 40 years in the metal casting industry to produce better quality parts than conventional casting processes with lower cost. Semi-solid forming can be divided into two main processing routes, (i) thixocasting and (ii) rheocasting. Thixocasting can yield high quality parts with high mechanical properties. On the other hand, the cost of the aluminum feedstock billets, reheating system, and forming machines are quite high. However the recent and the most favoured semi-solid processing route is the rheocasting route [12]. This is because rheocasting can provide cost advantages over thixocasting. In the thixoforming, the prefabricated billet is reheated to the semi-solid state prior to casting. Rheoforming generally starts with molten metal that is processed directly into semi solid slurry by controlled cooling, resulting in an appropriate non-dendritic structure (slurry on demand) [13]. During the semi-solid slurry making, the variations in the microstructure and processability of semi-solid slurries can be characterized by rheological tests using the viscosity as the main indication. A lower viscosity induces better movement of materials through the die and allows intricate thin-wall near net shape components to be cast at lower applied pressures [14].

The rheological behavior of semi-solid-metal is strongly dependent on the viscosity of the semi-solid billet and its importance is equivalent to that of fluidity for liquid metal [10]. Viscosity is an indication of semi-solid forming capability in the mold filling and in determining the required force for metal flow. The viscosity of semi-solid metal alloy is dependent on a number of metallurgical parameters including the solid fraction, solid particle size and morphology, particle distribution, chemical composition and pouring temperature. The rheological behavior, which is generally described in term of viscosity,

has been investigated using a variety of test techniques. Amongst those, parallel plate compression viscometry has been extensively used to determine the viscosity of semi-solid slurries due to the simplicity of the test procedure [15]. In this technique, a semi-solid billet is compressed between two parallel plates at constant deformation rate and the apparent viscosity can be estimated by using Newtonian or Non-Newtonian fluid models.

1.2 Objectives

The main objective of the current study is to investigate the rheological behaviour and microstructural evolution of a number of hypereutectic 390 alloy and new Al-15Si-xMg-4Cu alloys using the ALCAN patented Swirled Enthalpy Equilibration Device semi-solid process. The general objective can be achieved by dividing study into four sub-projects having the following objectives:

1. Processability and microstructural characterisation of semi-solid A390 alloy

- Studying the effects of isothermal holding and the addition of solid alloy on the processability and microstructure of semi-solid 390 alloys.
- Investigating the influence of phosphorus on the microstructure of semi-solid 390 alloys.
- Investigating the feasibility of making semi-solid slurry of hypereutectic Al-Si-Cu 390 alloys using SEED and modified rheoforming process.

2. Solidification and microstructural evolution of hypereutectic Al-Si-Mg-Cu alloys with high Mg contents

- Investigating the effect of the addition of high magnesium content on the solidification behaviour and microstructure of hypereutectic Al-15Si-xMg-Cu alloys.
- Establishing the solidification sequences and reactions of hypereutectic Al-15Si-xMg-4Cu alloys.
- Comparison of the Thermo-Calc results with those obtained by thermal analysis and corresponding alloy microstructure.

3. Effects of individual and combined addition of P and Sr on the modification of the microstructure of Al-15Si-14Mg-4Cu alloy

- Studying the effect of phosphorus addition on the size and morphology of primary Mg_2Si.
- Investigating the influence of Sr addition on the modification of eutectic structure.
- Comparing the effect of combined addition of P and Sr on the microstructure of the studied alloy.
- Investigating the effect of Sr addition on the formation of π-$Al_8Mg_3FeSi_6$ phase.

4. Rheological behaviour of 390 alloy and two hypereutectic Al-15Si-xMg-4Cu alloys with variable Mg contents

- Examining the influence of shear rate, solid fraction and chemical composition on the apparent viscosity of two semi-solid 390 alloys and two hypereutectic Al-15Si-xMg-4Cu alloys.

- Investigating the P refinement on the apparent viscosity and microstructure of semi-sold 390 alloys.
- Studying the effect of Mg contents on the apparent viscosity of hypereutectic Al-15Si-xMg-4Cu alloys.

References

[1] L. Lasa, J. M. Rodriguez-Ibabe. Materials Science and Engineering A, 2003, 363: 193–202.
[2] G. Timmermans, L. Froyen. Wear, 1999, 230: 105–117.
[3] H.J. Kim. Materials Science and Technology, 2003, 19: 915–918.
[4] J.R. Davis. Aluminum and Aluminum Alloys, ASM Specialty Handbook, ASM International, Materials Park, OH, U.S.A., 1993.
[5] J.G. Kaufman, E. L. Rooy. Aluminum Alloy Castings Properties, Processing, and Applications, ASM International, Materials Park, OH, U.S.A., 2004.
[6] L. Bäckerud, G. Chai and J. Tamminen. Solidification Characteristics of Aluminum Alloys, American Foundrymen's. SkanAluminium, Universitetsforlaget AS. Oslo, Norway: 1986.
[7] J. Jorstad, D. Apelian. International journal of metalcasting, (2009) Vol.3, Issue 3: 13-43.
[8] J. Zhang, Z. Fan, Y. Q. Wang, B. L. Zhou. Materials Science and Engineering A, 2000, A281: 104-112.
[9] Alireza Hekmat-Ardakan, Frank Ajersch. Acta Materialia, 2010, 58: 3422-3428.
[10] C. T. Wu, S. L. Lee, M. H. Hsieh, J. C. Lin. Metallurgical and Materials Transactions A, 2010, 41A: 751-757.
[11] S. A. Metz, M. C. Flemings. AFS Transaction, 1970, 78: 453.
[12] J. L. Jorstad. SSM processes-an overview, the 8th international conference on semi solid processing of alloys and composites, Limassol, Cyprus, 2004.
[13] Z. Fan. International Materials Reviews, 2002, 47: 49-84.
[14] S. Nafisi, O. Lashkari, R. Ghomashchi, F. Ajersch, A. Charrette. Acta Materialia, 2006, 54: 3503-3511.
[15] V. Laxmanan, M. C. Flemings. Metallurgical and materials Transactions A, 1980, 11: 1927-1937.

CHAPTER 2

LITERATURE REVIEW

CHAPTER 2

LITERATURE REVIEW

2.1 Semi-solid Metal Processing

2.1.1 Introduction

Semi-solid metal processing (SSM) is a promising process for the near net shaping of complex products. The original semi-solid forming process was invented at Massachusetts Institute of Technology (MIT), USA, in 1971 by Spencer and Flemings [1]. Spencer was investigating the shear stress of semi-solid slurry in order to illustrate the hot tearing mechanisms in solidifying Sn-15Pb alloy. He observed that the shearing clearly modified the microstructure, changing the morphology of the primary phase from dendritic to a more spherical shape resulting in a significant decrease in the viscosity of the alloy.

Semi-solid forming can be divided into two main processing methods: (1) thixoforming, where the prefabricated billet is reheated to the semi-solid region prior to forming, and (2) rheoforming, which involves molten metal that is processed directly into semi-solid slurry with appropriate non-dendritic structure. The rheocasting process has many obvious advantages over the thixocasting process by using a simple process step to attain a semi-solid material directly from liquid metal at small investment cost, and a large capability to use all possible material sources (primary, secondary, and particular process scrap).

Several techniques to transform liquid metals into semi-solid slurries have been developed in recent years. These techniques use different means of mixing, such as pouring,

stirring, and vibration, or by adding grain refiner to achieve a final cast structure with fine globular particles.

2.1.2 Mechanisms of spheroid formation

Semi-solid processing is based on forming metal components from unique non-dendritic structures. This can be produced by applying shear deformation to a metal alloy cooled through the temperature interval between its liquidus and solidus [2]. Conventional solidification without mixing or stirring results in the formation of dendrites, whereas the structure of sheared semi-solid slurry is characterized by rosette and/or globular primary particles dispersed in liquid matrix [2]. Over the last few decades, there have been several theories proposed to describe the formation of the non-dendritic structures during semi-solid processing. This includes enhanced nucleation and dendrite fragmentation [3,4,5,6]. The nucleation mechanism is obtained as a result of increasing the nucleation sites which is achieved by rapid and continuous heat extraction and melt convection. Li *et al.* [3] have investigated the microstructural evolution during the solidification of succinonitrile-5 at. % water transparent alloy and Sn-15wt. % Pb alloy using mechanical stirring, quenching and in-situ observations. They observed that without stirring/shearing, nucleation takes place on the walls of the container, leading to the formation of dendrites. However, with continuous stirring above the liquidus temperature, globular particles form directly from the melt. Consequently, the authors concluded that strong melt convection, induced by stirring in the semi-solid state promotes the formation of nucleation sites and makes the microstructure grow with a globular morphology. Wu *et al.* [4] obtained a semi-solid slurry of an Al-Si alloy by introducing mechanical vibration during isothermal holding for 5min. They

proposed that numerous nuclei are formed due to the undercooling. Jian *et al.* [7] studied the influence of ultrasonic vibration on the nucleation and growth during the solidification of aluminum alloy A356. The authors reported that the principal mechanism for the formation of globular structure was likely not due to the fragmentation mechanism, but due to heterogeneous nucleation induced by cavitation. On the other hand, the fragmentation mechanism proposes that the high density of solid grains is formed from detached secondary or tertiary dendrite arms due to solute enrichment and thermo-solutal convection near the dendrite root. Flemings [8] has listed a number of possible mechanisms for fragmentation of dendrite arms, which may be summarised in three types: (1) dendrite arms break off at their roots due to shear force; (2) dendrite arms melt off at their roots; (3) and dendrite arms bend under flow stresses creating boundaries within the bent dendrites followed by complete wetting of high angle, high energy grain boundaries by the liquid phase leading to eventual break-up of the dendrites. Hellwell *et al.* [9] presented a detailed discussion on dendrite fragmentation and the influence of fluid flow in casting. They suggested that remelting of dendrite arms at their roots, rather than breaking off by a mechanical force, might be the cause of grain multiplication.

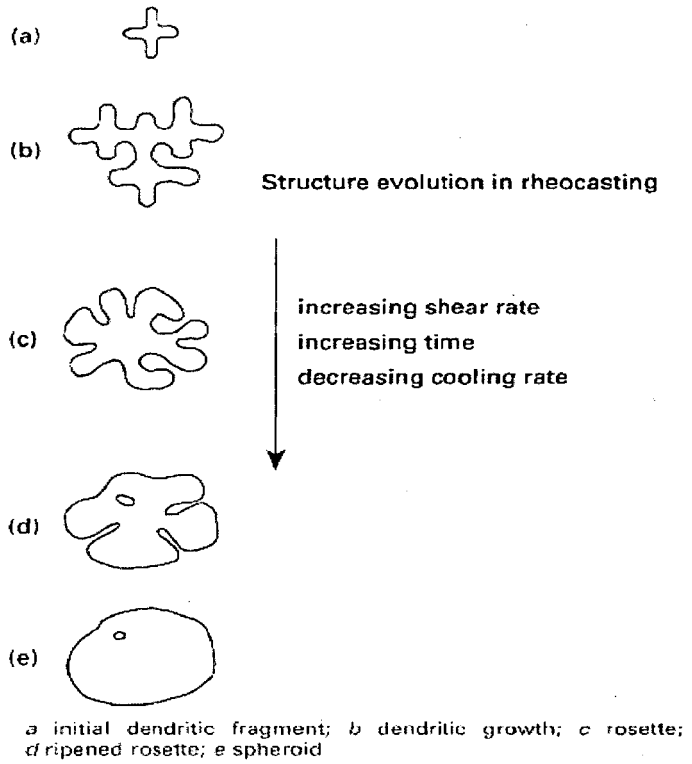

Fig. 2.1 Schematic illustration of structure evolution during solidification with forced convection: (a) initial dendritic fragment, (b) equiaxed dendrite, (c) rosette, (d) ripened rosette, and (e) globule [10].

2.1.3 Techniques of semi-solid forming

In this section, we review various techniques developed for semi-solid forming. Most of them are for the rheoforming process which is the focus of the present study. Some other semi-solid forming routes are also described.

2.1.3.1 Agitation processing

Mechanical stirring

Over the years, numerous devices have been devised to produce SSM slurries with non-dendritic microstructures. Mechanical stirring during solidification has been developed and used to produce the SSM slurry and to form components. In this process, the liquid alloy is

cooled below the eutectic temperature, where it is continuously stirred for periods of time as shown in Figure 2.2a and b. A stirring device is usually inserted into the semi-solid alloy. Mechanical stirring generally involves simple equipment. Specifically designed stirring equipment can be used to measure the viscosity of the slurries using either a rotating spindle (Searle type) or rotating crucible (Couette type). However, this technique can have serious limitations depending on the alloy-stirrer reactivity, the most important being the erosion of the stirrer, melt contamination by debris and oxides, gas entrainment and low productivity.

Electromagnetic stirring

In order to overcome the problems associated with direct mechanical stirring, a magnetohydrodynamic stirring (MHD) process was developed by ITT in the USA, and is described in a series of patents [11]. In this process, local shear is produced by rotating electromagnetic fields inside the continuous casting mould, using an induction coil around the ingot mold to generate strong electromagnetic stirring which break the dendrites into fine granular crystals. This fine structure can be cast directly or can be further spheroidized by reheating to the semi-solid state.

This method can be achieved through three different modes of induced flow: vertical, horizontal, and helical. In the vertical flow mode or linear stirring, dendrites are fragmented at the solidification front but are recycled to the hotter zone of the stirring chamber and partially remelted. In this case thermal processing is dominant over mechanical shearing (Figure 2.3b). In the case of the horizontal flow or rotational stirring, the solid particles move in a quasi-isothermal plane so that mechanical shearing is probably the dominant

mechanism for spheroidization (Figure 2.3a). The helical mode is a combination of the vertical and horizontal mode (Figure 2.3c).

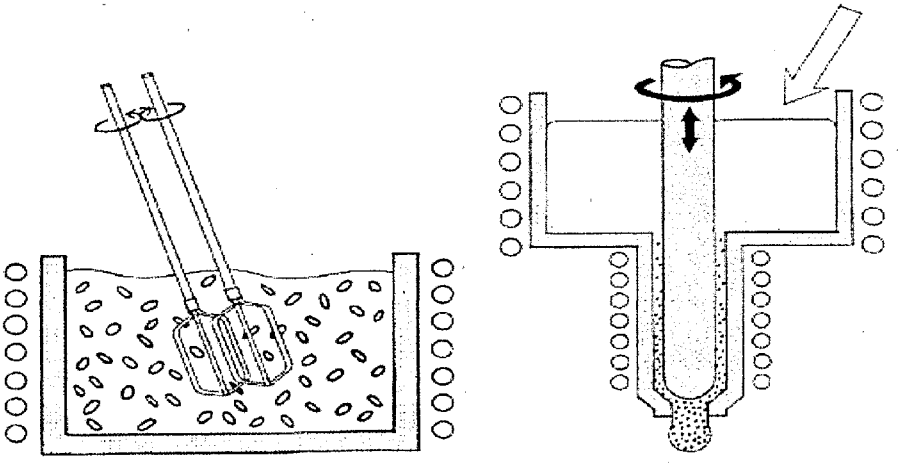

(a) (b)

Fig. 2.2 Schematic diagram of apparatus of producing globular structures: (a) batch, (b) continuous [10].

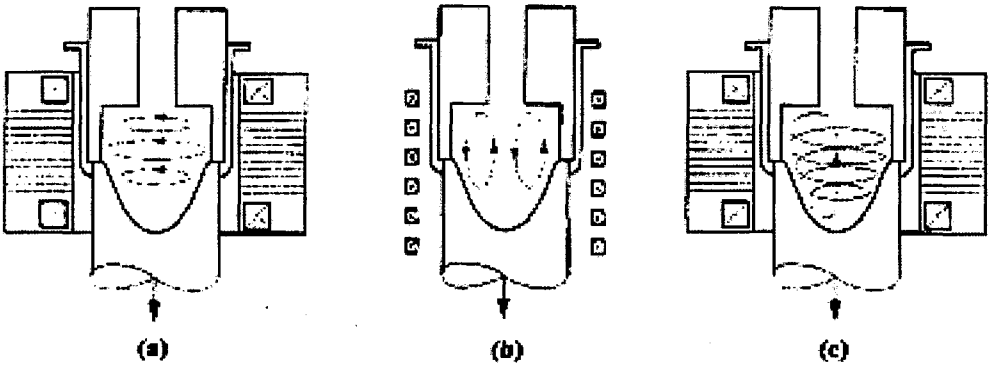

Fig. 2.3 Schematic representation of electromagnetic coils for MHD stirring: (a) Horizontal agitation, (b) Vertical agitation, (c) Helicoidal stirring [12].

Semi-solid rheocasting (SSR)

Semi-solid rheocasting (SSR) is a process recently developed at MIT by Flemings *et al.* [13]. This process has been shown to produce suitable slurry directly from molten metal, where globular primary phase particles are essentially free of entrapped liquid. In this process, non-dendritic slurries are obtained by combining agitation over very short times with localized heat extraction and isothermal holding or a short time of slow cooling in the mushy zone. As shown in Figure 2.4, a stirrer that also provides the cooling action is introduced in the melt held a few degrees above the liquidus. After some seconds of stirring, the temperature decreases to a value which corresponds to a fraction solid of only few percent, and the stirrer is removed. The rapid cooling and convection of the alloy as it cools through the liquidus temperature promotes formation of fine globular primary phase.

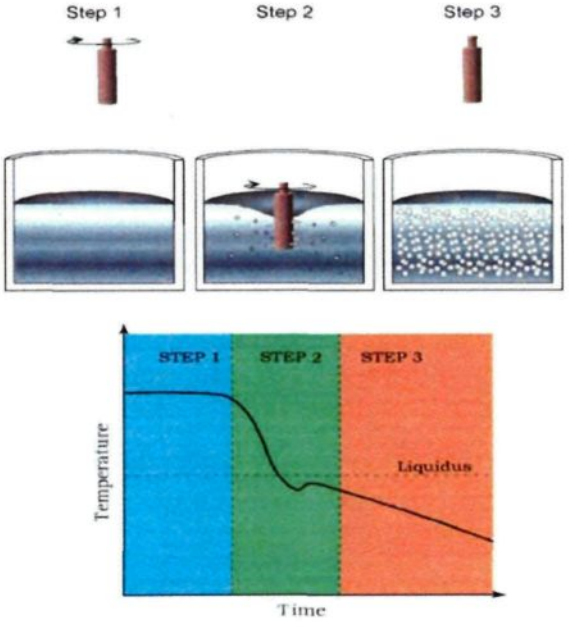

Fig. 2.4 (a) Sequence of steps employed in the « new MIT process »; (b) Melt thermal history [13].

The SEED process

The SEED process (Swirl Enthalpy Equilibration Device) is a slurry-on-demand process that involves applying mechanical mixing (swirling), which allows extraction of a controlled amount of heat from the molten metal to generate a solid-liquid mixture, and then draining away the excess liquid leaving behind a compact self-supporting slug. After drainage, the semi-solid slug can be transferred into a high pressure die casting machine. Figure 2.5 shows the schematic illustration of the SEED process. This process helps to overcome problems with high costs of feedstock. A large range of alloy compositions (A356/357, A206, A319, AA6061 and AA6082) can be processed by this technology. In addition, the process can produce different slug dimensions and weights.

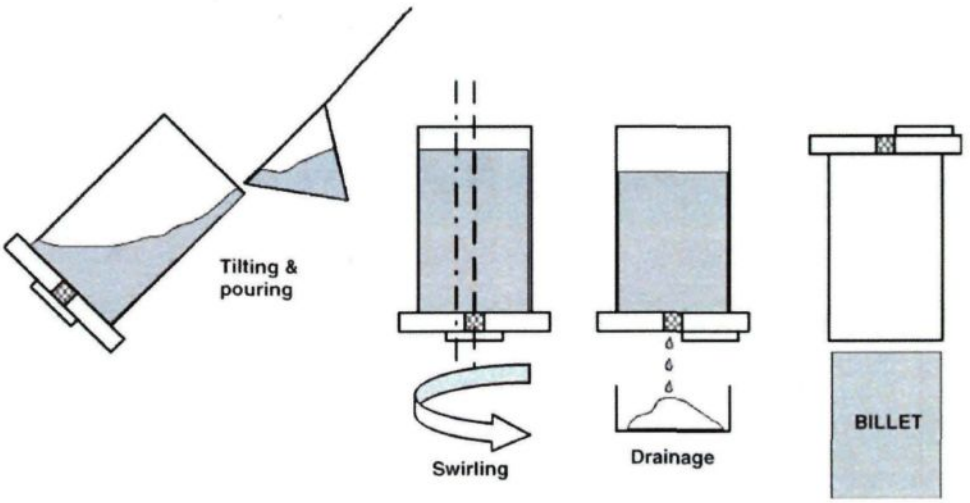

Fig. 2.5 Schematic illustration of the SEED process [14].

Twin screw rheomolding process

Figure 2.6 illustrates a twin-screw rheomolding apparatus developed by Ji *et al.* [15] that make use of concepts from injection molding of polymers. It consists of a liquid metal feeder, a twin-screw extruder, a shot assembly and a central control unit. The liquid metal feeder is designed to provide controlled volumes of metal at the desired temperature for a specified metal component. The design of the screws allows self-wiping, in addition to the positive pumping action of the slurry. The profile of this twin extruder is such that a high rate of shear and intense turbulence are achieved. The liquid metal is poured into the twin extruder and then quickly cooled to a predetermined processing temperature to adjust the volume fraction of the resulting slurry, which is then transferred to the die-casting mold. This apparatus consists of one step and is relatively simple. The production of the SSM slurry and parts casting are integrated into one single operation. In addition, the shear rate and high intensity of turbulence generated by the specially designed twin-screw extruder will provide a fine particle size and a spherical morphology.

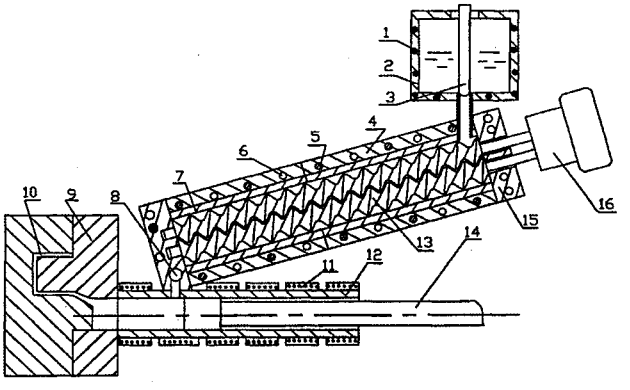

Fig. 2.6 Schematic illustration of the twin-screw rheomoulding process.1, Heating elements; 2, crucible; 3, stopping rod; 4, barrel; 5, heating elements; 6, cooling channels; 7, barrel liner; 8, transfer valve; 9, die; 10, mould cavity; 11, heating elements; 12, shot sleeve; 13, twin-screw; 14, piston; 15, end cup; 16, driving system [15].

2.1.3.2 Non-agitation processing

New rheocasting process (NRC)

This process, developed in Japan by UBE industries, Ltd. transfers the molten metal from the holding furnace via a ladle then into a specially designed steel cup which is finally placed on a cooling carousel (slurry maker carousel) next to the NRC machine. The globular microstructure is achieved by controlled cooling of the melt in the semi-solid region. In the final position of the carousel the temperature is equalized over the cross-section of the cup. The semi-solid slurry is then poured into the inclined sleeve of a squeeze casting machine and the slug is cast into shape. The typical sequence of process steps is shown in Figure 2.7.

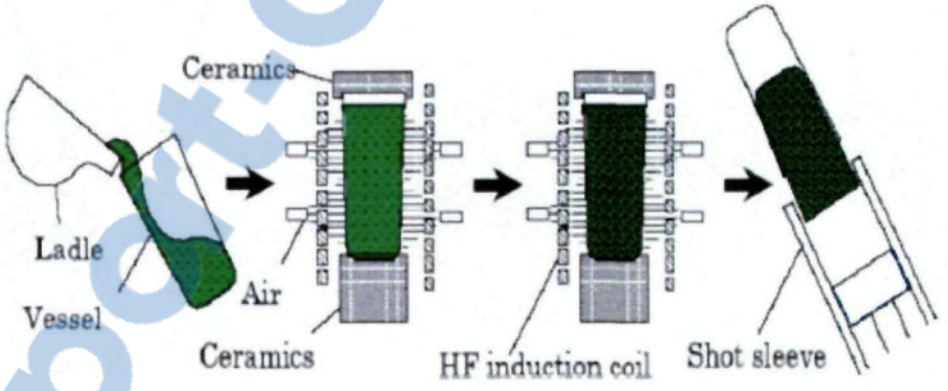

Fig. 2.7 Schematic of the NRC process (Courtesy of UBE Machineries) [16].

SIMA (Strain Induced Melt Activation)

The strain induced melt activation (SIMA) process was developed in UK by Kirkwood and co-workers [17]. In this process, a spheroidal grain structure is achieved by recrystallization of heavily deformed ingots and followed by a heat treatment in the semi-

solid zone. The apparatus has significant advantages of simplicity and low equipment cost. However, the temperature of heating, heating time and degree of cold working are critical factors in achieving the semi-solid microstructure in the SIMA process. This method can also use for high melting point alloys and was shown to be successful for many alloy systems including stainless steels and tool steels [18].

Spray casting

Spray forming is an advanced technique for the production of near net shape parts with improved properties and performance. In this method, a flow of liquid alloy is atomized by high velocity gas jets and a spray of atomized droplets is deposited upon a substrate, resulting in a bulk deposit. This method can be used for the production of tubes, bars and discs [19]. The resultant spray cast microstructure is quite similar to chemically grain refined billets. In this process, the semi-finished products are characterized by the elimination of macro-segregation with refined equiaxed grain structures, refinement of primary phase precipitates, with low oxygen contents, and enhanced hot workability [20]. Consequently, spray forming is capable of manufacturing semi-finished products with microstructures and properties that significantly outstrip those of conventional ingots or wrought materials. The schematic of the spray forming apparatus is shown in Figure 2.8.

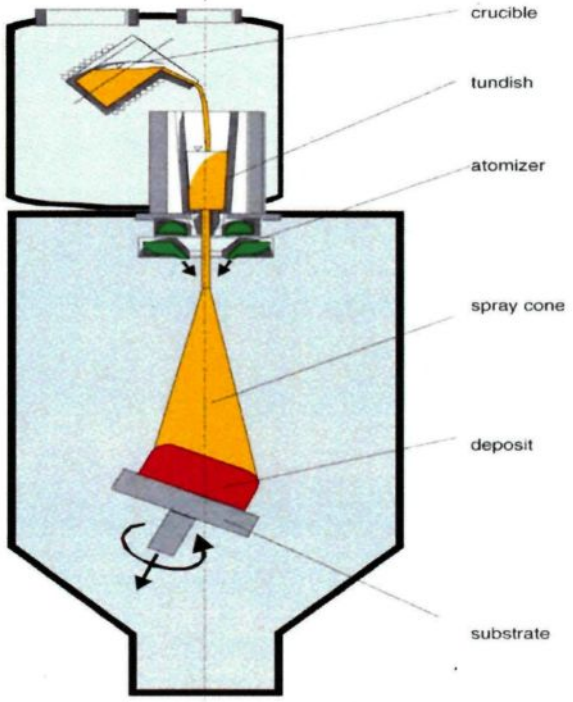

Fig. 2.8 A schematic of the spray forming apparatus [20].

Liquid casting

Recently, casting of an alloy near the liquidus was shown to produce fine equiaxed grains [21]. The molten metal is poured into a tilted crucible from near liquidus temperature, resulting in a microstructure with unusual non-dendritic grains.

Chemical grain refining

This promising alternative method is used for the production of slurries for thixocasting. In this method, a globular microstructure can be achieved by simply reheating chemically grain refined billets acquired from primary producers. Chemical grain refining is used jointly with other feedstock production methods, such as MHD stirring and liquidus casting [22]. With this method, however, it is difficult to ensure that the grain structure is uniformly

spheroidal and fine. In addition, the volume of liquid entrapped in spheroids tends to be relatively high.

Ultrasonic treatment

Application of ultrasonic treatment to a solidifying melt at a temperature just above its liquidus can effectively produce a fine and globular microstructure, which is suitable for subsequent reheating and thixoforming operations. Fine and non-dendritic microstructures are obtained when a high power ultrasonic vibration is applied to the solidifying alloy. The mechanism explaining microstructural changes is based on cavitation and acoustic streaming. Cavitation induces the formation, growth and collapsing of small bubbles in the melt. The high compression rate of these unsteady state bubbles generates hydraulic waves resulting in the creation of nucleation sites. Furthermore, the shock waves during the collapse of cavitation bubbles cause crystal breakage at the solidification front [23].

Thixoforming

The thixoforming or thixomolding process was developed by Dow Chemical and has become an important commercial process for semi-solid casting of magnesium alloys [24]. This process is similar to the injection molding of polymers; a schematic diagram of the process is shown in Figure 2.9. In this process solid chips or pellets of conventionally solidified alloys are introduced into a heated injection system equipped with a screw feeder and atmosphere control. The screw feeder is progressively heated and the metal chips are transformed by the shear action of the screw into a semi-solid slurry. The material, in the form of a low solid content slurry ($f_s \sim 0.3$), is then fed into the shot accumulator by the rotating screw. Once the accumulation chamber is filled, the slurry is injected into the

mold. This process avoids the safety problems associated with melting and handling molten magnesium. The concept of this process is also applicable to aluminum and zinc alloys.

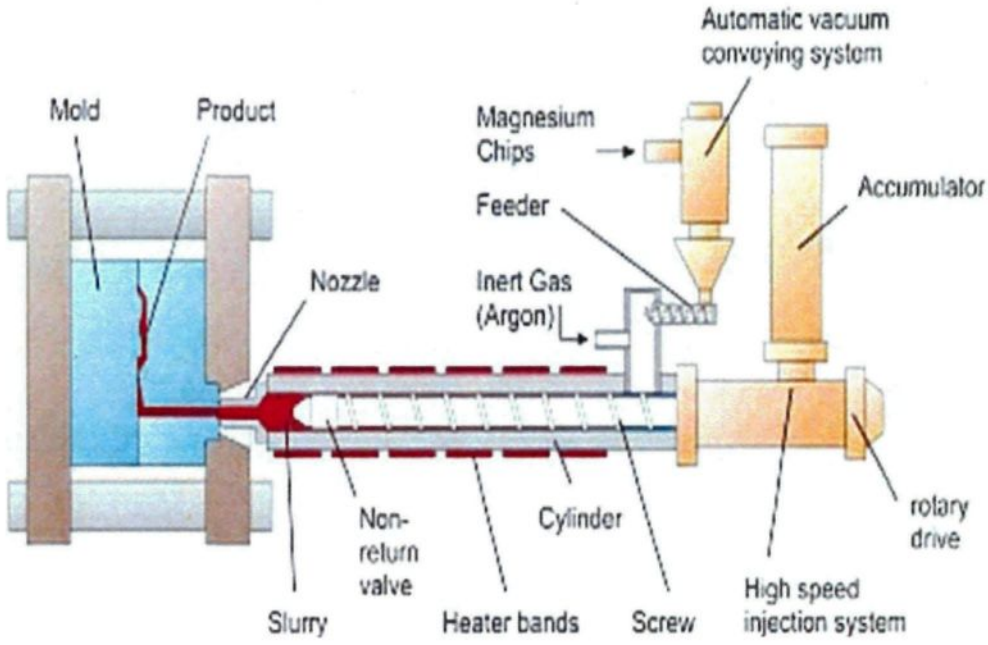

Fig. 2.9 Schematic diagram of a thixomolding machine [25].

2.1.4 Advantages of semi-solid processing

Semi-solid forming combines a number of advantages of both conventional casting and forging. These benefits are outlined in Table 2.1.

Table 2.1 Advantages of semi-solid forming.

Characteristics	Potential benefits and application
Lower heat content than liquid metal	Higher speed part forming Higher speed continuous casting Lower mold erosion Ferrous part forming Forming of high melting point materials Forming of reactive materials
Solid present at time of mold filling	Less shrinkage voids Less feeding required Less macrosegregation Fine grain structure
Viscosity higher than liquid metals and controllable	Less entrapped mold gases Reduced oxides Improved machinability Less mold attack Higher speed part forming Improved surface finishing Automation and new processes
Flow stress lower than solid metals	Forming of intricate parts High speed part forming Lower cost part forming High speed forming of continuous shapes New processes
Ability to incorporate other materials	Composites
Ability to separate liquid and solid	Purification

2.2 Rheology of Semi-solid Metals

2.2.1 Introduction

Rheology is defined as the science of the deformation and flow of materials. Generally, to study rheological properties, a controlled, well defined deformation or strain is applied to a material over a given time and the resulting force response is measured to give an indication of material parameters such as modulus, stiffness, viscosity, hardness, strength or toughness of the material.

The rheological behaviour of partially solidified metal alloys with equiaxed microstructure is important for SSM forming due to the complexity of the flow response that is encountered in the near net-shape forming of semi-solid slurries of various components. The rheological behaviour of semi-solid metal is strongly dependent on the viscosity of the slurry and its importance is equivalent to that of fluidity for liquid metal [26]. The viscosity of semi-solid metal alloy is dependent on a number of metallurgical parameters including the fraction solid, solid particle size and morphology, particle distribution, chemical composition, shear rate and pouring temperature. The fluid flow behaviour of semi-solid slurry has been investigated using a variety of characterization techniques. These include rotational viscometry [27], capillary rheometry [28-29], indentation [30-31], back extrusion [32-34], and compression between parallel plates [35].

2.2.2 Deformation behaviour of semi-solid slurries with dendritic structure

Metz *et al.* [36, 37] carried out shearing tests on semi-solid alloys with volume fraction solid up to about 0.5 at a deformation rate of $0.01s^{-1}$ using the block shearing technique. Spencer *et al.* [38] carried out similar experiments using a concentric cylinder technique at

a deformation rate of 0.16 s^{-1}. The results are shown in Figures 2.10 and 2.11. The authors observed that there is a certain point during the deformation test when the dendrites form a cohesive network and the slug develops strength. The stress required to shear the slurry at a constant rate increases until it reaches the maximum point or so called apparent yield stress as shown in Figure 2.12. Further deformation causes fissures at which the shearing is localized and decreases significantly. Laxmanan and Flemings [39] have also investigated the rheological behaviour of semi-solid Sn-15 wt% Pb using a parallel plate viscometer. Semi-solid samples with dendritric and non-dendritic structure were deformed under initial pressures up to 232 KPa and at solid fractions from 0.15 to 0.60. The authors found that the non-dendritic sample deforms homogeneously without cracking. However, dendritic alloys require much higher deformation loads and crack easily. In addition, the nondendritic and the dendritic alloys exhibit a pseudoplastic behaviour without any yield point.

Pinsky *et al.* [40] have also studied the deformation behaviour of semi-solid dendritic Sn-Pb alloys using a parallel plate apparatus. They arranged their experimental setup to simulate the situations encountered in applications, such as extrusion, and concluded that the deformation occurs in two distinct modes. The first mode is the compaction of solid during which the liquid is expelled without any significant flowing of the solid phase. The second mode follows when the stress reaches a value that remains stable thereafter. Suery *et al.* [41] investigated the deformation behaviour of ordinary dendritic semi-solid tin-lead alloys, and reported that, in the range of low deformation rate, bulk segregation of liquid and solid was observed, and the dendrite structure was seen to break down for strains greater than about 0.4.

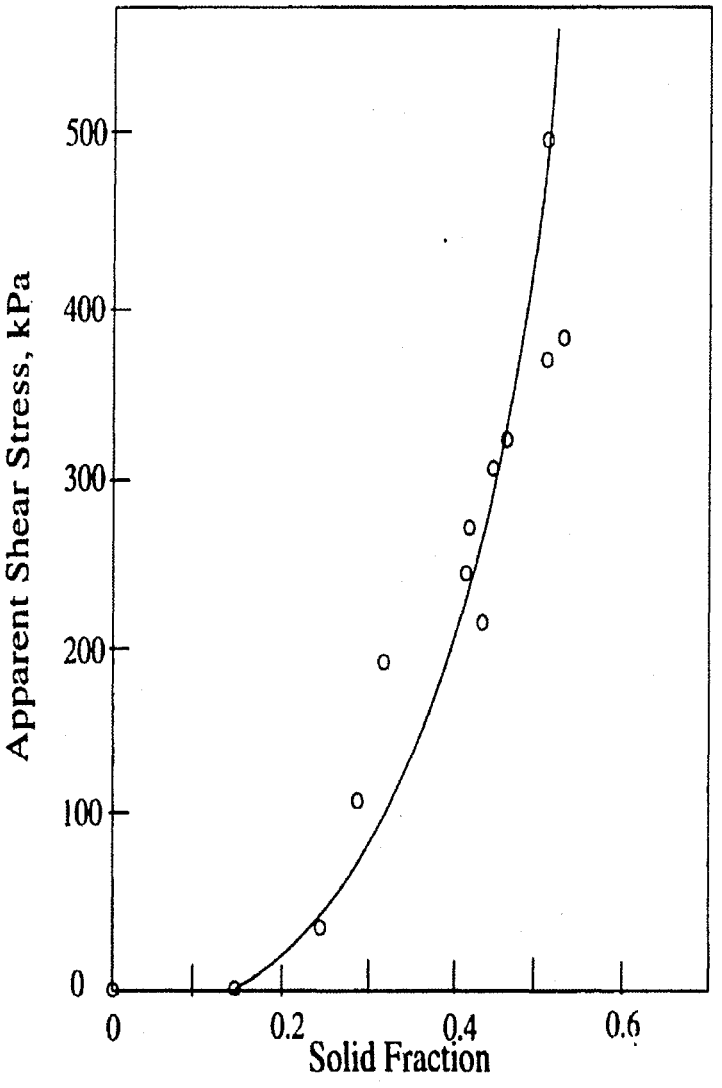

Fig. 2.10 Variation in yield stress with solid fraction for Sn-15%Pb alloy with dendritic structure [38].

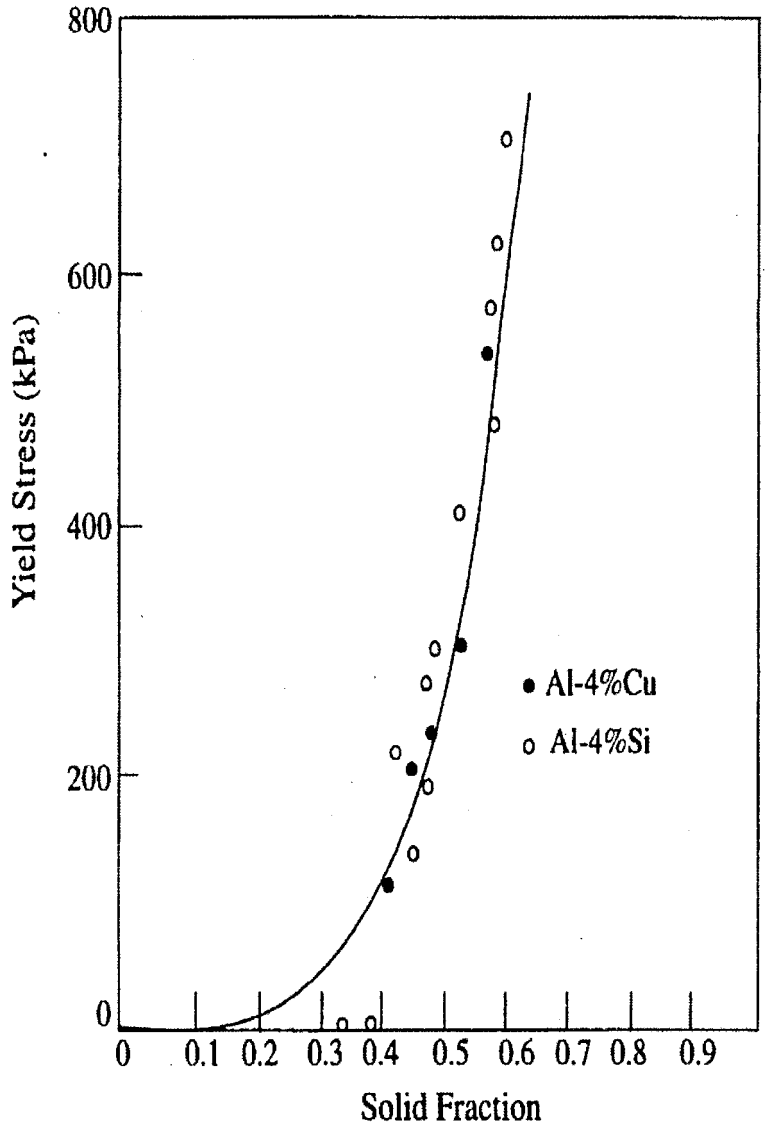

Fig. 2.11 Variation in yield stress under shear with solid fraction for dendritic Al-4%Cu and Al-4%Si alloys [37].

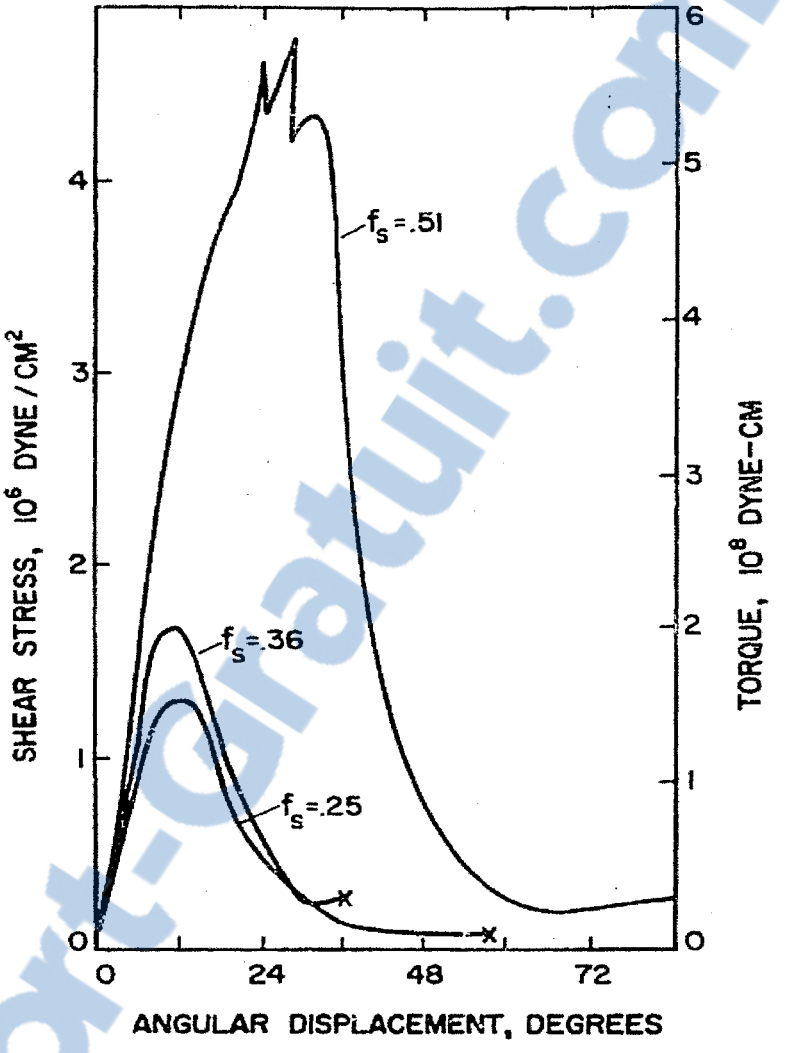

Fig. 2.12 Shear stress and torque versus versus angular displacement for various volume fraction solid values [38].

2.2.3 Deformation behaviour of semi-solid slurries with non-dendritic structure

The study of the rheology of metals in the semi-solid state was pioneered by Spencer *et al.* [38] in 1971. The authors reported that applied shear strain on solidifying Sn-15%Pb alloy, resulted in a significant reduction in shear stress compared with specimens that were not sheared during solidification. The microstructure of the sheared alloy was non-

dendritic, as opposed to the dendritic structure of the non-sheared alloy. Joly *et al.* [42] investigated the effect of different thermo-mechanical treatments on the microstructure and on the rheological properties of Sn-15wt.%Pb alloy using concentric cylinder viscometry. They observed that, in addition to the speed of rotation, non-dendritic formation during continuous cooling also improved by decreasing the cooling rate. Vogel *et al.* [43] and Kattamis *et al.* [44] studied the influence of shear conditions on the morphology and size in continuous cooling tests and observed that, at a given cooling rate, an increase in speed of rotation induced a smaller particle size.

2.2.3.1 Influence of solid fraction on apparent viscosity

The apparent viscosity has been found to be strongly influenced by the solid volume fraction. Spencer *et al.* [38] found that the apparent viscosity of semi-solid slurry increases with decreasing temperature due to the increasing volume fraction of primary phase. Joly *et al.* [42] reported that at high shear rates the apparent viscosity of continuously cooled slurries of Sn-15%Pb shows a linear dependence over ranges of volume fraction solid and can be described by an equation of the type:

$$\eta_a = A \exp. Bg_s \qquad (2\text{-}1)$$

where η_a is the apparent viscosity and g_s is the volume solid fraction. The coefficients A and B are found to be functions of shear rate and cooling rate.

Moon [45] has also studied the effect of the solid volume fraction on the apparent viscosity of semi-solid Al-6.5% Si slurries and composite slurries. The author found that the A and B coefficient are dependent on shear rate and cooling rate. Ito *et al.* [46] introduced the concept of liquid entrapped inside agglomerates. The authors suggested that

the effective solid volume fraction, i.e. volume fraction of solid plus volume fraction of entrapped liquid should be used if one tries to correlate the volume fraction solid to the apparent viscosity (Fig. 2.13).

2.2.3.2 Influence of shear rate on viscosity

The viscosity of semi-solid slurries at constant temperature decreases remarkably with increasing shear rate as shown in Figure 2.14. This behaviour is known as pseudo-plasticity or shear-thinning. This shear rate dependency of viscosity was attributed to the degree of agglomeration between solid particles, which, in turn, is the result of a dynamic equilibrium between agglomeration and deagglomeration processes [1]. At low shear rates, many bonds form between solid particles (agglomerates), and viscosity is high. At high shear rates, the agglomerate size of the solid decrease by rupture of the solid bridges. This decrease in size leads to the release of the entrapped liquid, thus reducing the resistance to flow (viscosity). The rate at which this dissociation and reagglomeration occurs is time dependent which characterizes the thixotropic behaviour. This was also confirmed later by the work of Ito *et al.* [46] performed on Al-Si alloy sheared at different rates using metallographic observations. In addition, they observed that high shear rates lead to a smaller volume fraction of entrapped liquid.

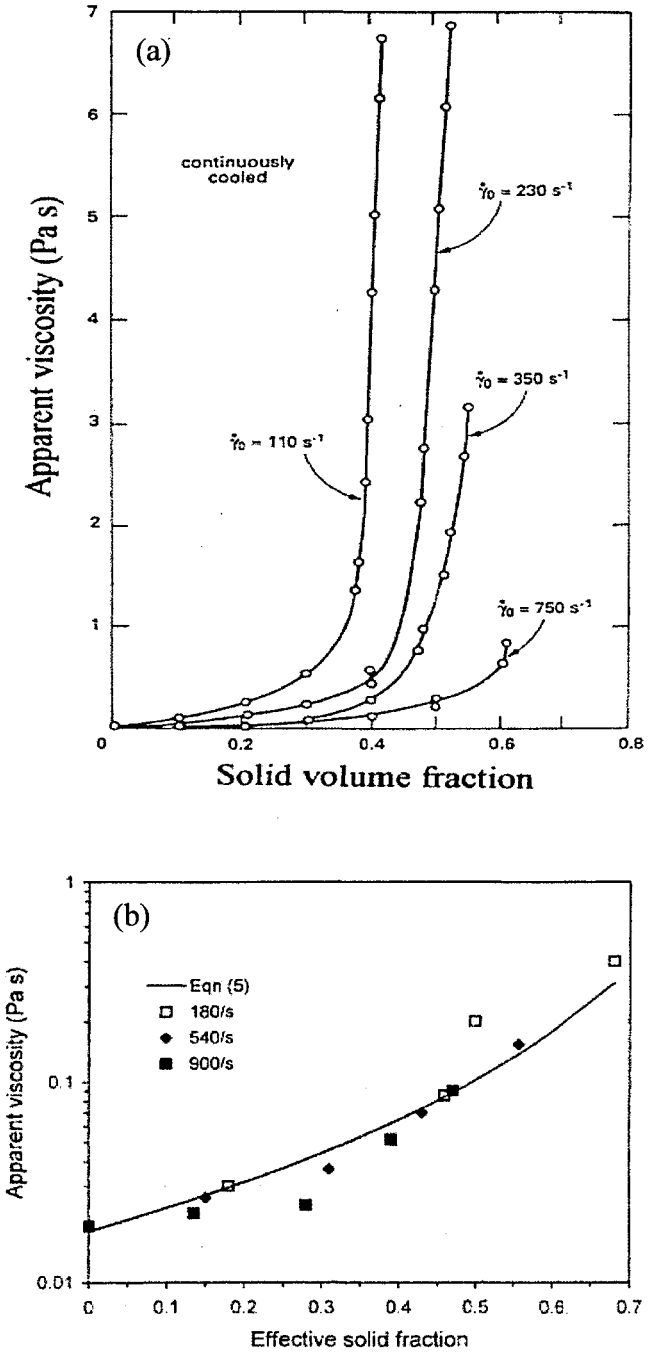

Fig. 2.13 (a) Apparent viscosity as function of fraction solid of Sn-15wt.%Pb sheared continuously and cooled at 0.33 K min^{-1} [42], (b) apparent viscosity versus effective solid fraction [47].

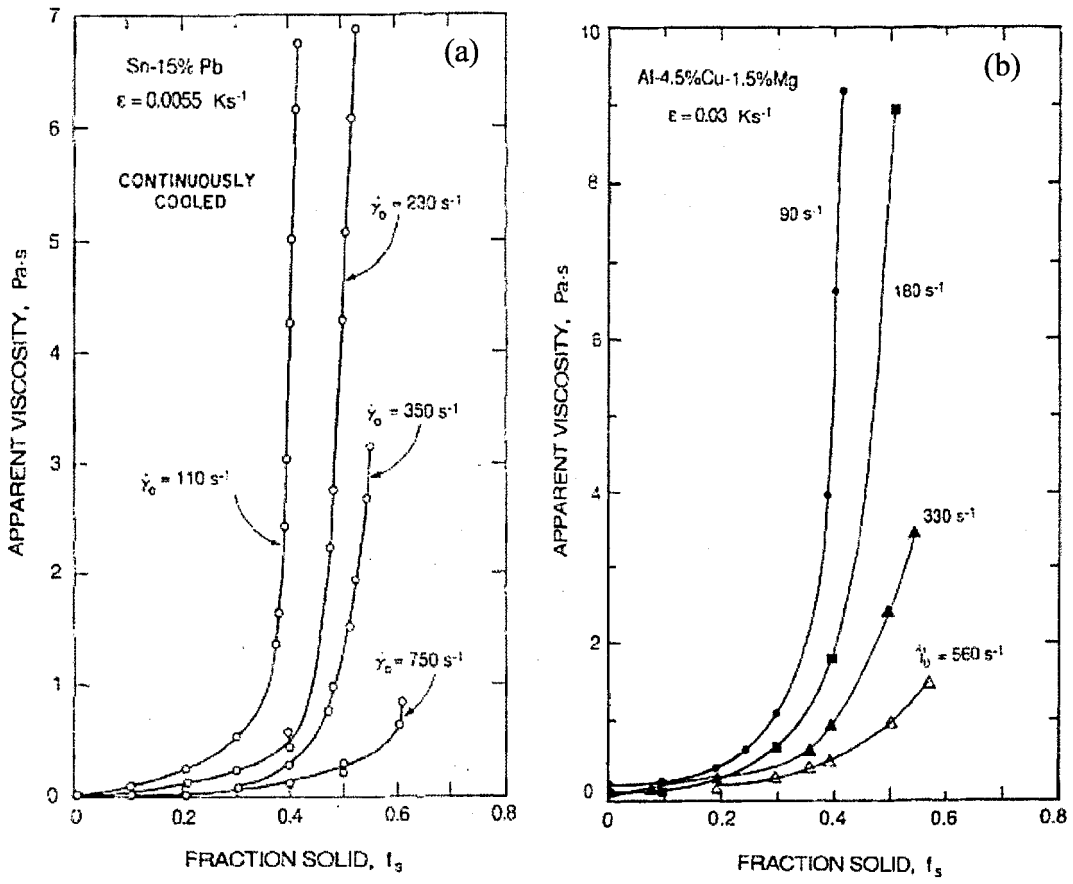

Fig.2-14 Influence of shear rate on apparent viscosity of semi-solid alloys (a) Sn-15wt.%Pb [42] and (b) Al-4.5wt.%Cu-1.5 wt.%Mg [10].

2.2.3.3 Influence of cooling rate on viscosity

The cooling rate in the semi-solid slurries is an important factor affecting viscosity as illustrated by the two examples in Figure 2.15. Generally speaking, the viscosity decreases as the cooling rate decreases. Joly *et al.* [42] showed that the viscosity was sensitive to the cooling rate and shearing rate. They reported that low cooling rates and high shear rates decrease the viscosity for a given solid fraction. Both increasing shear rate and decreasing

cooling rate result in more rounded globules, which move more easily past one another [10].

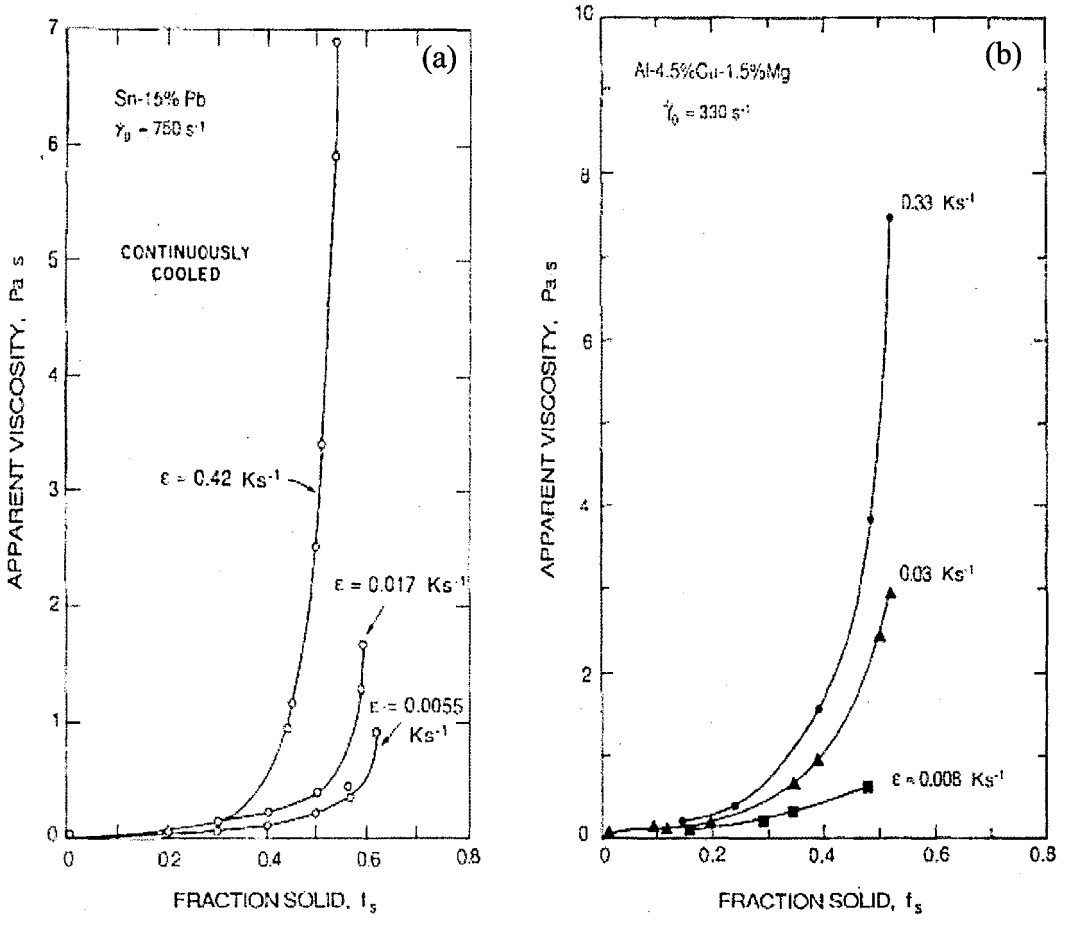

Fig. 2.15 Influence of cooling rate on apparent viscosity of semi-solid alloys: (a) Sn-15wt.%Pb [10], and (b) Al-4.5wt.%Cu-1.5 wt.%Mg [44].

2.2.3.4 Influence of size and shape of solid particles

It has been reported [38] that the viscosity of alloy slurries is highly dependent on the size and shape of the primary solid particles, these being a function of the shear rate and the cooling rate. The effect is explained by considering the microstructure of the semi-solid slurry. At higher cooling rates, primary dendrites do not have enough time to change into

globular particles. The deformed dendritic and rosette-shaped structures cause more resistance to the flow than the globular shape. Flemings *et al.* [13] have shown that the viscosity of semi-solid alloys depends strongly on the sphericity of the primary solid particles. Dendritic or rosette-shaped structures produce slurries of higher viscosity compared with globular structures. Moon [45] compared the apparent viscosity of semi-solid Al-6.5 wt. % Si and that of alloy slurries containing SiC particulates. The author observed that the viscosity of semi-solid slurry is lower than that of the composite system at a given solid fraction. He concluded that semi-solid slurries containing solid particles have a high specific surface area (high aspect ratio) and result in higher apparent viscosity than slurries with solid particles of lower specific surface area. Doherty et al. [43] observed that the morphology of the primary solid phase in the semi-solid Al-20~30wt%Cu alloys evolved from dendritic via rosette-type to a globular structure with increasing shear rate and stirring time. This tendency has been confirmed in other studies [42, 48].

2.2.3.5 Thixotropic behaviour

Thixotropy is defined as the time dependency of the viscosity. This behaviour was first demonstrated by Joly and Mehrabian [42] on Sn-15Pb alloy. The alloy was gradually brought to a specified temperature in the semi-solid region. The hysteresis loops during shear deformation were generated to study the thixotropy of the system by using the Green-Weltmann method. An example is presented in Figure 2.16, showing the upward curve (increasing shear rate) above the return curve resulting in a hysteresis loop. The area enclosed is a measure of the thixotropy of the material. However, this method is not sufficient to quantify the kinetics of the agglomeration and deagglomeration processes.

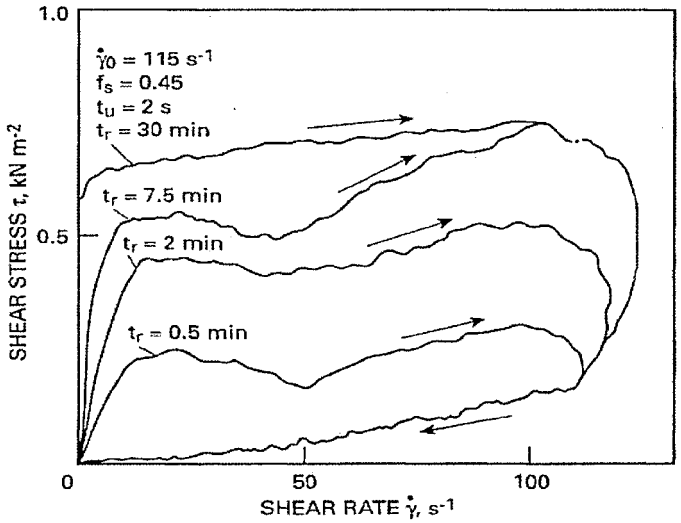

Fig. 2.16 Effect of rest time on hysteresis loops displayed by Sn-15wt.%Pb alloy[42].

2.2.4 Experimental techniques

Rheological tests consist of the measurement of the forces required to produce given controlled deformations. These techniques measure well defined properties, such as stress, strain or viscosity in characterizing the rheological properties of semi-solid slurries.

The concentric cylinder rheometer has been widely employed in the study of semi-solid alloys [42, 45]. The major advantage of this technique is the possibility of producing the globular microstructure suitable for the rheocasting directly in the apparatus. During the experiment, the alloy is sheared between two concentric cylinders. This technique can have two different experimental configurations; rotating crucible (Couette) or rotating cylinder (Searle). However, this method is limited to low shear rates and low solid fractions, because a high shear rate can cause flow instability and high solid fractions can lead to wall slippage. The apparent viscosity is calculated by the set of equations given below using the torque that is measured.

$$\tau = \frac{T}{2\pi r^2 L} \tag{2-2}$$

$$\overset{o}{\gamma} = \frac{2\Omega}{r^2}\left(\frac{r_i^2 r_o^2}{r_o^2 - r_i^2}\right) \tag{2-3}$$

$$\eta = \frac{T}{4\pi L\Omega}\left(\frac{1}{r_i^2} - \frac{1}{r_o^2}\right) \tag{2-4}$$

Where T is the torque, L is the liquid height inside the cylinder, $\overset{o}{\gamma}$ is the shear rate, Ω is the angular speed of the rotor, η is the apparent viscosity, r_i is the inner cylinder radius, and r_o is the outer cylinder radius.

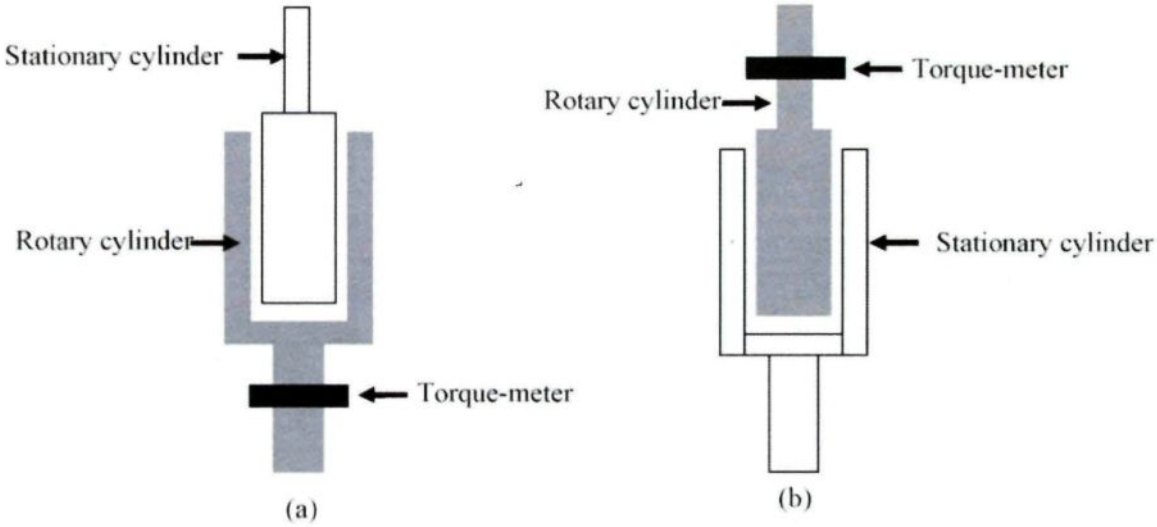

Fig. 2.17 The two types of viscometers (a) Couette and (b) Searle.

Compression between parallel plates has also been extensively used to investigate the deformation behaviour of semi-solid slurries owing to the simplicity of the test (Figure

2.18). In this method, a cylindrical sample with low aspect ratio is compressed between two parallel plates at constant deformation rate or under constant load [39]. This apparatus can be used to characterise semi-solid slurries with high solid fraction, and to detect the presence of yield stress. By contrast, it is difficult to define the steady state deformation rate due to solid/liquid segregation. In this method the deformation behaviour is first investigated by analyzing strain variation versus time. The resulting strain-time curve is further treated mathematically to characterize the rheological behaviour of the tested alloy. The interpretation of results obtained from such curves can be treated differently depending on whether the SSM slug behaves as Newtonian or non-Newtonian material. At low shear rates i.e. less than 0.01 s^{-1}, the resulting curves could be treated similar to that of Newtonian fluids [39]

Assuming that the shear rate value is low and does not vary appreciably within the sample during the compression test, the results can be expressed by the Stefan equation:

$$F = -\frac{3\eta V^2}{2\pi h^5}\left(\frac{dh}{dt}\right) \qquad (2\text{-}5)$$

The solution of Eq [2-5] was obtained by first integrating from $h = h_0$ at $t = 0$ and $h = h$ at $t = t$.

$$\frac{1}{h^4} - \frac{1}{h_0^4} = \frac{8\pi F t}{3\eta V^2} \qquad (2\text{-}6)$$

$$\frac{3Vh_0}{8\pi P_0}\left(\frac{1}{h^4} - \frac{1}{h_0^4}\right) = \frac{t}{\eta} \qquad (2\text{-}7)$$

The corresponding average value of the shear rate, at any instant during the compression test is given by:

$$\dot{\gamma}_{av} = -\sqrt{\frac{V}{\pi}}\left(\frac{dh/dt}{2h^{2.5}}\right) \qquad (2\text{-}8)$$

where η, V, h_0, h, F and t are the viscosity (Pa.s), volume of specimen (mm^3), initial height (mm), instantaneous height (mm), applied dead force (N), and deformation time (s), respectively.

If the semi-solid alloys are treated as non-Newtonian fluids, the solution to the deformation equations for cylindrical sample compressed between two parallel plates is as follows:

$$\frac{h_o}{h} = \left\{1 + \left(\frac{3n+5}{2n}\right) k h_o^{\frac{n+1}{n}} t\right\}^{\frac{2n}{3n+5}} \qquad (2\text{-}9)$$

Where

$$k = \left\{\left(\frac{2n}{2n+1}\right)^n \left(\frac{4(n+3)}{\pi m d_o^{n+3}}\right) F\right\}^{\frac{1}{n}} \qquad (2\text{-}10)$$

Equation 2-9 is only valid for deformation under steady state conditions where the engineering strain changes linearly with time. Equation 2-9 could be further treated mathematically including engineering strain (e) as given in equation 2-10.

$$\log(1-e) = -\left(\frac{2n}{3n+5}\right)\log t - \left(\frac{2n}{3n+5}\right)\log\left(\frac{3n+5}{2n} k h_o^{\frac{n+1}{n}}\right) \qquad (2\text{-}11)$$

The power l-law parameters m and n may be obtained from the slope and intercept of a plot of log (1 - e) *vs* log t at long times. The details of this analysis may be found in Appendix B.

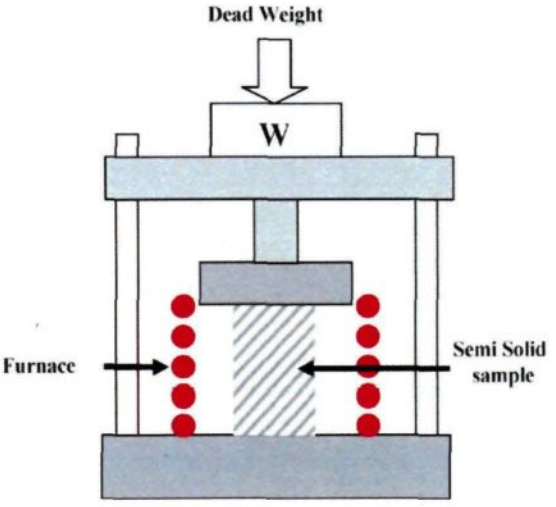

Fig. 2.18 A schematic of the parallel plate compression test.

Indentation tests are used to study mechanical properties of slugs [49]. In this method, the depth of penetration of a steel cylinder under a constant pressure in the slurry is taken as an indication of the viscosity of the alloy, as shown in Figure 2.19. Figure 2.20 shows the influence of testing parameter and solid fraction on the indenter-slurry interaction [49]. The following equation was used to calculate the viscosity of semi-solid alloy during an indentation test:

$$\eta = \frac{16\ \pi^{\frac{3}{2}} \left[\left(1 - \upsilon^{2}\right) F\right]}{6\sqrt{\pi r}\ \dot{\varepsilon}_{o}} \qquad (2\text{-}12)$$

Where υ is the Poisson ratio, F is the applied load; r is the radius of the cylindrical indenter, and $\dot{\varepsilon}$ is the strain rate.

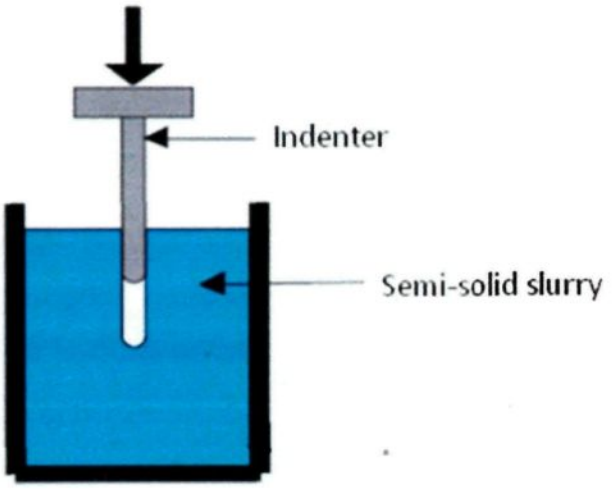

Fig. 2.19 A schematic of the indentation test [50].

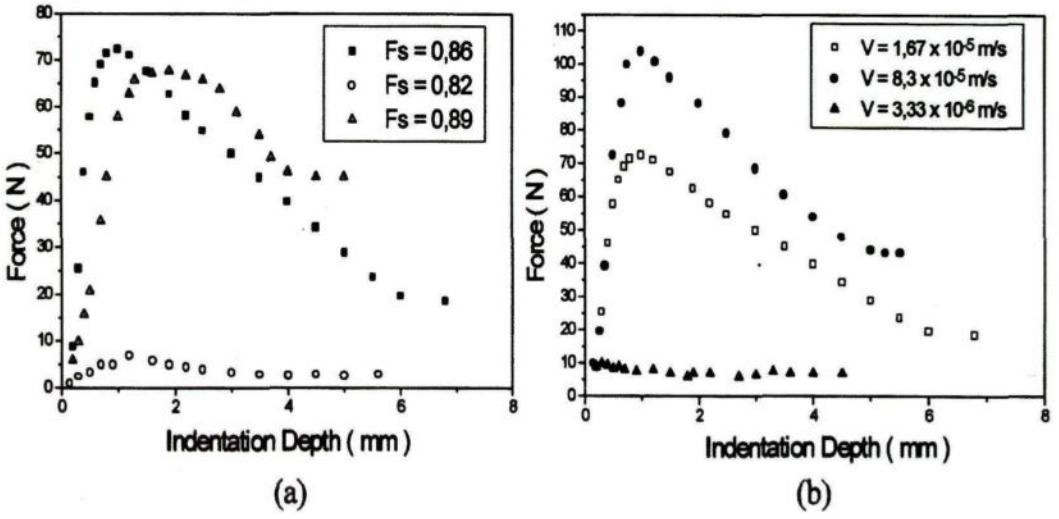

Fig. 2.20 Results of the indentation test for (a) constant penetration speeds and different f_s; (b) different penetration speeds at f_s =0.86 [49].

Extrusion tests may also be employed to investigate die fill-ability of slurries with information on the viscosity of the semi-solid alloy. Figure 2.21 shows a schematic of direct and indirect extrusion tests [50]. More experimental details and suitable theorical treatments for such methods are accessible in the literature [51, 52].

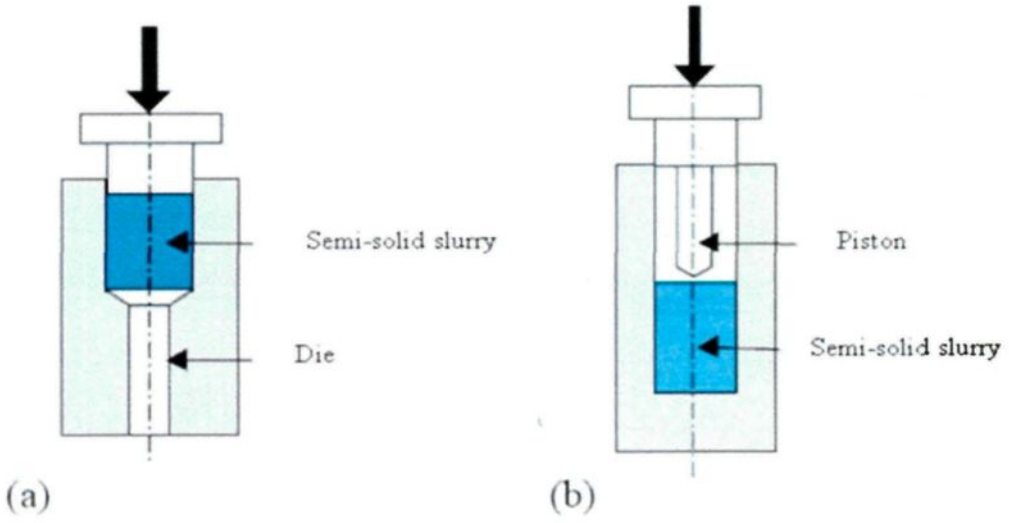

Fig. 2.21 A schematic of the extrusion viscometry (a) direct extrusion, (b) indirect extrusion [50].

2.3 Hypereutectic Al-Si-Mg-Cu alloys

2.3.1 Hypereutectic Al-Si-Mg-Cu alloys with low Mg content

Al-Si alloys with silicon as the major alloying addition are very important aluminum cast alloys because of their high fluidity, low shrinkage, high corrosion resistance, good weldability, easy brazing, and low coefficient of thermal expansion (CTE) [53-55]. Depending on the amount of silicon, the alloys may be divided into three groups:

hypoeutectic alloys with a Si content of 5-10%, eutectic alloys with 11-13% Si and hypereutectic alloys with a normal Si content of 14-20%.

Hypereutectic Al-Si alloys such as A390 alloy have generated significant interest in recent years, due to their attractive properties, such as low coefficient of thermal expansion, high wear resistance, high strength, and hardness. Typical composition of the most commonly used hypereutectic Al-Si alloys are shown in Table 2.2.

Table 2.2 Chemical composition of hypereutectic Al-Si alloys.

Si	Fe	Cu	Mg	Mn	Zn	Ti	P	Al
16-18	1.0 max	4.0-5.0	0.5-0.65	0.1 max	0.2 max	Traces	0.1 max	Bal.

The presence of primary silicon in the matrix provides the good wear resistance and high hardness. Some of the most common applications are: engine blocks, cylinder heads, clutch input housing, clutch assembly, brake cylinders, oil pump coolers, valve covers, cylinder sleeves, drives sleeves, clutch assemblies, brake cylinders, gears, pump housings, pulley wheels and brake drums.

The Al-Si system is a simple binary eutectic with the eutectic composition at about 12 wt.% Si and 577°C. The binary equilibrium diagram of aluminum and silicon is shown in Figure 2.19. With silicon contents higher than 12.6 wt.% the alloy solidifies with diamond-cubic silicon as the primary phase. In the Al-Si system, the solid solubility of aluminum in solid silicon at any temperature is almost nil, with a maximum value of ~ 0.17 wt.% [56]. The maximum solubility of silicon in aluminum is 1.49 at.% at the eutectic temperature and

is reduced to 0.05 at.% at 300°C and 0.01 at.% at 227°C [57]. Backerud *et al.* [58] studied the solidification of hypereutectic Al-Si alloys such as A390 alloy. The solidification reactions reported by them are listed in Table 2.3. It can be observed that the solidification begins with the precipitation of primary silicon. The second phase precipitated is a small volume fraction of dendritic aluminum, rather than the eutectic phases. During the eutectic reaction Al, Si and β-Al_5FeSi phases start to precipitate. θ-Al_2Cu and Mg_2Si phases precipitate in later reactions, below 510 °C.

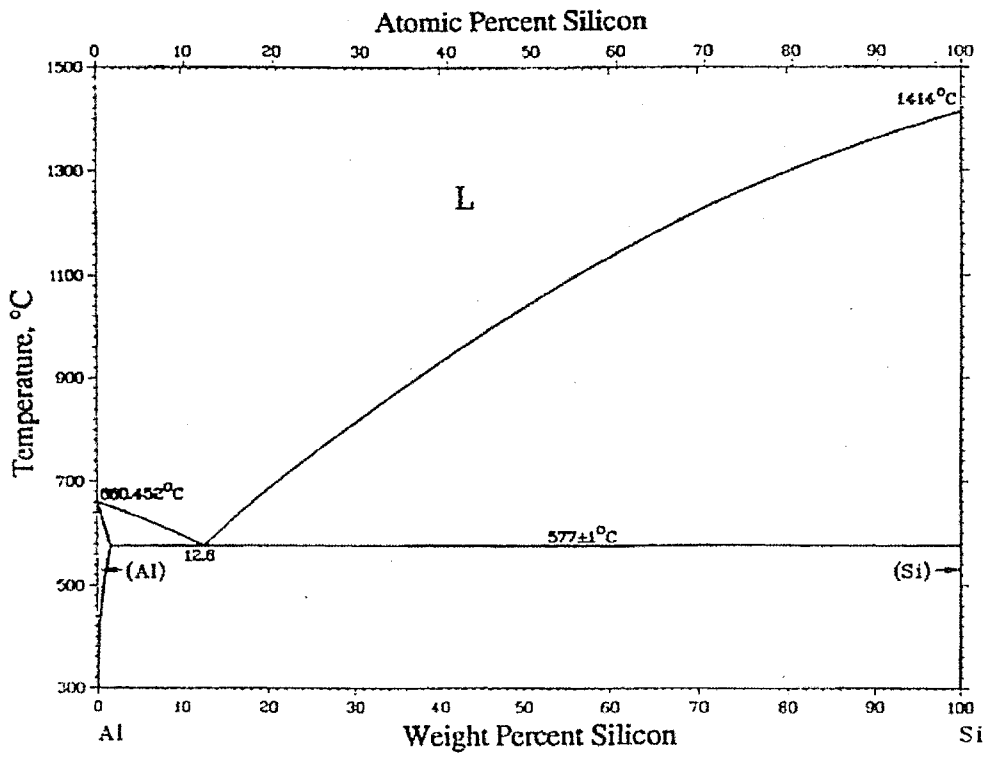

Fig. 2.22: Equilibrium phase diagram of Al-Si system [59].

Table 2.3 Solidification reactions for A390 alloy [58]

N°	Reactions	Suggested temperature °C (K)
1	Precipitation of primary Si crystal	654 (927)
2	Development of α-Al dendrites	628 (901)
3	Start of eutectic reaction Liq.→ α-Al+Si+Al_5FeSi	565 (838)
4	Precipitation of Mg_2Si Liq.→ α-Al+Si+ Mg_2Si	540 (813)
5	Precipitation of Al_2Cu L+ Mg_2Si → α-Al+Si+ Al_2Cu+$Al_5Mg_8Cu_2Si_6$	500 (773)
6	Precipitation of complexe eutectic Liq.→ α-Al+Si+ Al_2Cu+ $Al_5Mg_8Cu_2Si_6$	499 (772)
7	End of solidification	494 (768)

2.3.2 Mechanical properties of SSM cast hypereutectic Al-Si alloy

The mechanical properties of conventional and semi-solid A390 alloy are shown in Table 2.4. It is clearly apparent that stirred semi-solid and squeeze cast 390-T6 alloy yield comparable tensile properties and hardness, and both exhibit higher strength than either sand cast or GPM 390-T6 alloy.

Table 2.4 Mechanical properties of A390 alloy for various casting processes [60].

Process	Temper	Yield Strength (ksi)	Tensile Strength (ksi)	% Elongation	BHN
Sand casting	T6	40	40	-	140
GPM[a]	T6	45	45	-	145
CDC	F	35	40.5	-	120
CDC	T5	38	43	-	125
Squeeze	T6	-	51-56.9	<1.0	145-165
SSM (EM-stirred)	F	26.8	31.9	1.0	115
SSM (EM-stirred)	T5	39.2	39.2	<0.2	140
SSM (EM-stirred)	T5	32.6	32.6	<0.2	115
SSM (EM-stirred)	T6	-	49.5-55.9	<1.0	140-160
SSM (EM-stirred)	T6	50.8	50.8	<0.2	165

a = tensile properties and hardness determined from standard cast-to-size tensile bars

2.3.3 Hypereutectic Al-Si-Mg-Cu alloys with high Mg content

Hypereutectic Al-Si alloys with high Mg contents have been attracting much attention as an important lightweight material for potential application in the automotive and aerospace industries due to their relatively low density and good wear resistance as compared with other structural metals [61,62]. These alloys are considered as *in-situ* aluminum matrix composites containing a large amount of Mg_2Si particles and could be potential candidates to replace Al-Si alloys in engine applications. These Al-Mg_2Si composites show high potential as automobile brake disc material because the reinforcement Mg_2Si exhibits a high melting temperature of 1085 ^{o}C, low density of 1.99 x 10^3 kg m^{-3}, high hardness of 4.5

x 10^9 N m^{-2}, a low thermal expansion coefficient of 7.5 x 10^{-6} K^{-1} and a reasonably high elastic modulus of 120 GPa [63].

Mandal *et al.* [64] studied the microstructure and mechanical properties of cast hypereutectic Al-Si alloys with magnesium contents up to 5.02 wt pct. They found that the Mg addition changed the morphology and size of the primary silicon phase and also observed that the tensile strength of these alloys was found to be superior to that of A390 alloy, but with lower hardness. Zeng *et al.* [65] examined the effect of both Si and Mg contents in Al-Si-Mg alloys, where the concentration of Si and Mg varied from 8 to 17 wt pct and 2 to 4 wt pct, respectively. They found that the addition of 2 - 4 wt pct Mg to Al-Si alloys changes the brittle β-Al_5FeSi phase to the π-$Al_8Si_6Mg_3Fe$ phase, showing that the castability and mechanical properties of the alloys increase significantly at higher Mg contents. Recently, Hekmat-Ardakan *et al.* [66] reported that higher Mg contents change the morphology of the eutectic silicon from long platelet-like form to a fine Chinese script form while the primary silicon particles are suppressed and are replaced by primary Mg_2Si phase. They also examined the wear properties of hypereutectic Al-Si-Cu-Mg alloys containing 6 wt pct and 10 wt pct Mg in the as-cast condition and after T6 heat treatment compared to the wear resistance of A390 alloy [61]. It was found that the wear resistance increases considerably for alloys with high Mg content. From their investigations, the authors concluded that the improvement of wear resistance is due to transformation of the coarse primary Si particles to a finer Mg_2Si intermetallic phase.

Zhang *et al.* [67] have shown that Mg_2Si has a density of 1.99 x $10^3$$kgm^{-3}$, a low thermal expansion coefficient of 7.5 $10^{-6}K^{-1}$, a high melting temperature of 1085 ^oC, a high

hardness of 4.5 x $10^9 Nm^{-2}$ and a reasonably high elastic modulus of 120 GPa [Table 2.5]. These properties are important characteristics for the development of *in-situ* metal matrix composites containing Al and Mg_2Si designed to improve the traditional Al-Si hypereutectic alloys [68] currently used in the automotive and aerospace industry.

Table 2.5 Physical and mechanical properties of Mg_2Si and Si [69].

Phases point	Cristal structure	Lattice parameter (nm)	Density ($g\ cm^{-3}$)	C.T.E ($10^{-6}\ K^{-1}$)	Elastic modulus (GPa)	Melting (°C)
Mg_2Si	Cubic	0.635	1.99	7.5	120	1085
Si	Cubic	0.542	2.33	3.06	112	1411

Several studies [70, 71, 72] have reported on the methods of modifying the Mg_2Si primary phase of the in-situ composite containing Mg_2Si in the Al matrix. However, information on the solidification process of the in-situ composite produced by alloying of hypereutectic Al-Si with Mg is limited. Zhang *et al.* [73] reported that microstructural changes in the Al/Mg_2Si composite system were not explained clearly in previous investigations due to the very limited information on the Al-Mg-Si ternary phase diagram, especially for high Mg and Si contents.

More recently, Hekmat-Ardakan *et al.* [74] studied the solidification of hypereutectic Al-Si-Cu A390 alloys with less than 10 wt. pct. Mg using the FactSage software. The authors have reported that the addition of Mg up to 10 wt. pct. alters the formation temperature for the liquidus, and the start of the binary and ternary eutectic reactions. The Mg_2Si phase precipitates as an intermetallic compound for contents up to 4.2 wt pct and between 4.2 wt pct and 7.2 wt pct Mg. However, for compositions above 7.2 wt pct Mg, the Mg_2Si solidifies as the primary phase instead of Si (Figure 2.23).

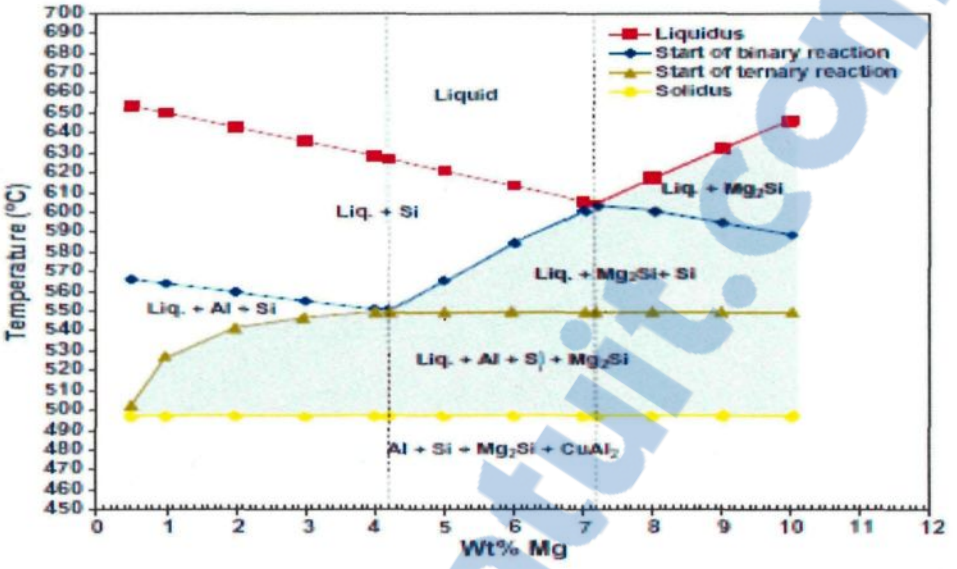

Fig. 2.23 Equilibrium phase diagram of Al-Si-Mg system [74].

2.3.4 Refinement and modification in hypereutectic alloys

2.3.4.1 Phosphorous refinement

The size and morphology of primary silicon in hypereutectic Al-Si alloys can be affected by the composition, cooling rate, and superheat temperature. In conventional solidification at moderate cooling rates primary silicon crystallises as hexagonal plates joined together at a center, which appear as star-shaped particles in cross-section. Without heterogeneous nuclei, primary Si nucleates only after a considerable undercooling. Jorstad [75] has reported that if primary Si nucleated with high undercooling, the crystal can grow very quickly to a large size.

On the other hand, hypereutectic Al-Si-Mg alloys with high Mg contents easily form undesirable, coarse dendritic primary Mg_2Si and brittle Chinese script Mg_2Si eutectic phase, which are harmful to the mechanical properties of the alloys.

Phosphorous refinement is one effective method to control the primary Si particle size in hypereutectic Al-Si. Phosphorus reacts with the liquid aluminum to form aluminum phosphide, AlP, which has a crystal structure very similar to that of silicon, and acts as an effective heterogeneous nucleant. Refinement of primary Mg_2Si in the hypereutectic Al-Si-Mg alloys with high Mg contents is also achieved by the addition of phosphorus to the melt.

2.3.4.2 Strontium Modification

Strontium modification is a melt treatment process usually applied in the foundry industry in order to change the morphology of the eutectic Si phase. This process is frequently applied to both hypoeutectic and hypereutectic Al-Si alloys, and generally consists of the addition of elements such as Na or Sr. Crossley and Mondolfo [76] proposed a physical model to explain the modifying mechanism of Sr addition. The authors assumed that the eutectic Si grows at a faster rate than aluminum, thus resulting in sharp acicular particles in the unmodified microstructure. However, the addition of Sr reduces the surface tension of aluminum and increases the contact angle between aluminum and silicon, thus allowing the aluminum to envelop and to obstruct the growth of the Si phase as well as to promote that of the aluminum dendrites.

Dahle *et al.* [77] compared the development of the cast structure on a macroscopic scale in both unmodified and Sr-modified alloys, see Figure 2.24. Cozonal twinning was present in the silicon fibres in all alloys with twins lying parallel to the apparent growth direction of the fibres. As shown in Figure 2.24(a), it was possible to identify silicon crystals which were not twinned in the unmodified alloys. In unmodified alloys, the vast majority of

eutectic aluminum had an orientation identical to that of the surrounding dendrites, while in Sr-modified alloys the eutectic aluminum displayed multiple orientations unrelated to the surrounding dendrites, as seen in Figure 2.24(b). There was a dramatic difference to be observed in the size of the eutectic grains as shown in Figure 2.24(c). The eutectic grains in the unmodified alloy were, at most, a few hundred microns in diameter and consist of relatively few coarse silicon plates. In the Sr-modified alloys, the eutectic grains were roughly circular in cross-section and were typically much larger than in the unmodified alloys. Each eutectic grain in the Sr-modified alloys contained a high density of silicon fibres; see Figure 2.24(d). The difference in the eutectic grain size between the unmodified and Sr-modified alloys was further made apparent in the macrographs of samples quenched early during eutectic solidification, as shown in Figure 2.24(e). The eutectic grain size in the unmodified sample was so small that no grains were resolvable in the macrograph. However, there was a layer of coalesced eutectic grains lining the wall of the sample in the Sr-modified alloy, and several large grains could be seen independently distributed throughout the centre of the casting.

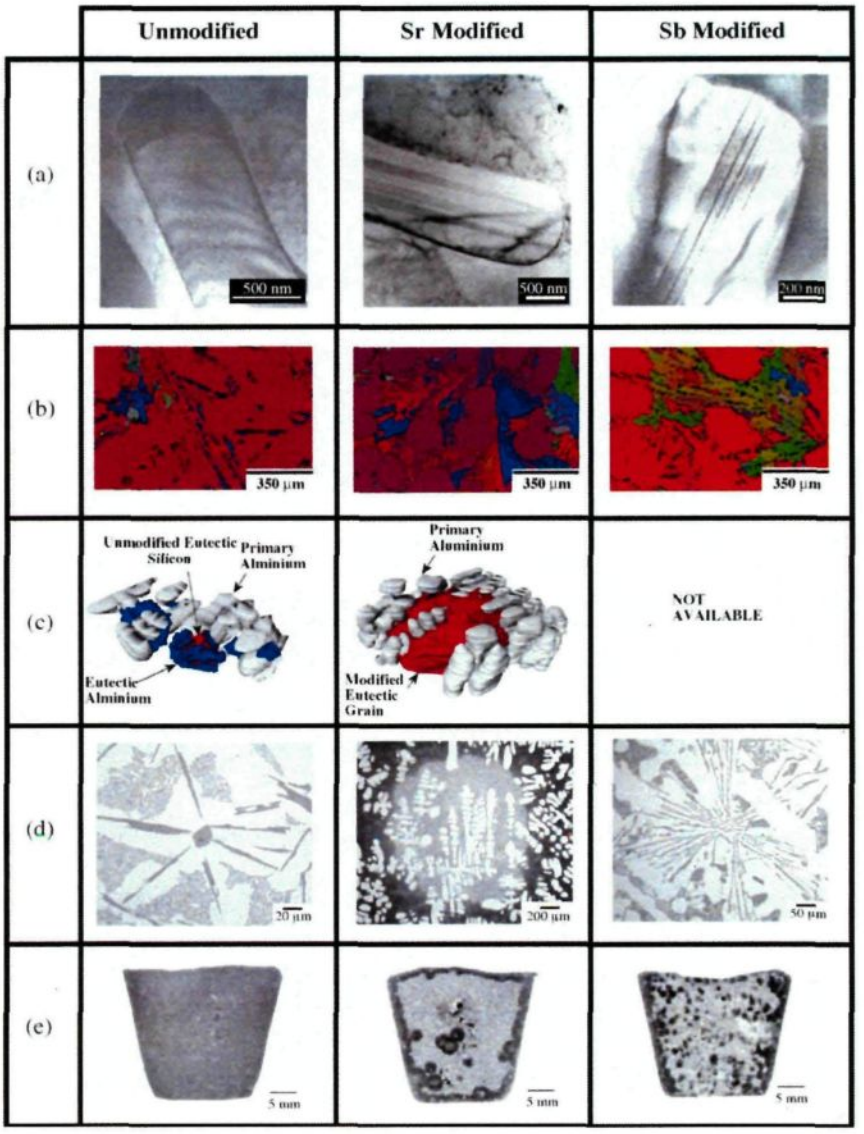

Fig. 2.24 Comparison of unmodified and Sr-modified structures: (a) TEM images of silicon crystals; (b) EBSD maps illustrating the orientation of the eutectic aluminum relative to the primary aluminum dendrites; (c) 3D reconstruction of eutectic grains derived from serial sectioning of quenched samples (the unmodified sample is 85 /in deep, the modified one is 117/in deep); (d) Optical micrographs of quenched samples; and (e) macrographs of quenched samples [77].

References

[1] D. B. Spencer. PhD thesis, MIT, Cambridge, MA, 1971.
[2] S. Ji. Journal of Materials Science, 2003, 38: 1559-1564.
[3] T. Li, X. Lin, W. Huang. Acta Materialia, 2006, 54: 4815-4824.
[4] S. Wu, L. Xie, J. Zhao, H. Nakae. Scripta Materialia, 2008, 58: 556–559.
[5] D. Ruvalcaba, R. H. Mathiesen, D. G. Eskin, L. Arnberg, L. Katgerman. Acta Materialia, 2007, 55: 4287–4292.
[6] M. C. Flemings, J. Yurko, R. Martinez. Semi-solid forming: Our understanding today and its implications for improved process. The 8th International Conference on Semi-Solid Processing of Alloys and Composites. Limassol, Cyprus, 2004.
[7] X. Jian, H. Xu, T. T. Meek, Q. Han. Materials Letters, 2005, 59: 190–193.
[8] M. C. Flemings. Solidification processing, Metallurgical transaction, 1974, 5: 2121-2134.
[9] A. Hellawel. The 4th international conference on semi solid processing of alloys and composites, Sheffield, Cyprus, 2004
[10] M.C. Flemings. Metallurgical and Materials Transactions A, 1991, 22A: 957-981.
[11] M. P. Kenney, J. A. Courtois, R. D. Evan, G. M. Farrior, C. P.Kyonka, A. A. Koch, and K. P. Young: in 'Metals handbook',9 edn, Vol. 15, 327-338; 1988, Metals Park, OR, ASM International.
[12] F. Niedermaier, J. Langgartner, G. Hirt., I. Niedick. "Horizontal Continuous Casting of SSM Billets", 5th International Conference on Semi-Solid Processing of Alloys and Composites, Golden, Colorado, USA, 1998: 407-414
[13] M. C. Flemings, R. Martines, A. M. de Figueredo, J. Yurko. 21th International Die Casting Congress, Cincinatti, Oh., 2001.
[14] S. Nafisi, O. Lashkari, R. Ghomashchi, J. Langlais, B. Kulunk. "The SEED Technology: A New Generation in Rheocasting", Light Metals, CIM publication 2005: 359-371
[15] S. Ji, Z. Fan, M.J. Bevis. Materials Science and Engineering A, 2001, A299: 210-217.
[16] J. Wannasin, S. Thanabumrungkul. Songklanakarin Journal Science and Technology, 2008, 30 (2): 215-220.
[17] D.H. Kikwood. International Materials Reviews, 1994, 39: 173-189.
[18] Kenneth Proung: 17th IDCCE Trans., 1993, 387.
[19] P. Mathur, D. Apelian, A. Lawley. Acta Materiallia, 1989, 37: 429-443.
[20] C. Cui, U. Fritsching, A. Schulz, R. Tinscher, K. Bauckhage, P. Mayr. Journal of Materials Processing Technology , 2005, 168: 496-504.
[21] X. Pan, H. Zhang, A. Wang, B. Ding, K. Qiu, Z. Hu. Journal of Materials Science and Technology, 2000, 16: 453-460.
[22] H. Wang, C.J. Davidson, D.H. StJohn, in: G.L. Chiarmetta, M. Rosso (Eds.), Proceeding of the 6th International Conference on the Processings of Semi-Solid Alloys and Composites, Turin, Italy, 2000: 149-154.
[23] V. Abramov, O. Abrarnov, V. Bulgakov, F. Sommer. Materials Letters, 1998, vol.37: 27-34.

[24] R. K. Kilbert, P. S. Frederick, N. L. Bradley, R. O. Newman, R. D. Carnahan, NADCA Transaction, 1991, T91-011: 1-4.
[25] D.H. Kirkwood. Semi solid Processing of Alloys. Springer-Verlag Berlin Heidelberg 2010.
[26] O. Lashkari, R. Ghomashchi. Journal of Material Processing Technology, 2007, 182: 229-240.
[27] P. A. Joly, R. Mehrabian. Journal of Materials Science ,1976, 11, 1393-1418.
[28] F. C. Yee: Ph.D. Thesis, Nanyang Technical University, Singapore, Republic of Singapore, 1999.
[29] M. Modigell, J. Koke, R. Kopp, D. Neudenberger, P. R. O. Klaassen, Proceding of the 6th International Conference on the Processing of Semi-Solid Alloys and Composites, G.L. Chiarmetta and M. Rosso, eds., Edimet, Brescia, Italy, 2000: 605-09.
[30] P. Vicente-Hernandez, A. M. Chase, and C. Levaillant: Proc. Sec. International Conference on the Processing of Semi-Solid Alloys and Composites, S.B. Brown and M.C. Flemings, eds., TMS, Warrendale, PA, 1992: 316-27.
[31] C. Rouff, R. Bigot, V. Favier, and M. Robelet. Proceding 6th International Conference on the Processing of Semi-Solid Alloys and Composites, G.L. Chiarmetta and M. Rosso, eds., Edimet, Brescia, Italy, 2000: 405-10.
[32] W.R. Loue, M. Suéry, and J.L. Querbes. Proc. Sec. International Conference on the 27 Processing of Semi-Solid Alloys and Composites, S.B. Brown and M.C.Flemings, eds, TMS, Warrendale, PA, 1992, vol. 49: 211-219.
[33] J. C. Gebelin, M. Surry, and D. Favier. Materials Science and Engineering A, 1999, vol. A272: 134-44.
[34] T. Basner, R. Pehlke, and A. Sachdev. Metallurgical and Materials Transactions A, 2000, vol. 31A: 57-62.
[35] F. Kolenda, P. Retana, G. Racineux, A. Poitou. Powder Technology, 2003, 130: 56-62.
[36] S. A. Metz, M. C. Flemings. AFS Transaction. 1969, 77: 329-334.
[37] S. A. Metz, M. C. Flemings. AFS Transansaction. 1970, 78: 453-460.
[38] D. B. Specer, R. Mehrabian, M. C. Flemings. Metallurgical and Materials Transactions B, 1972, 3: 1925-1932.
[39] V. Laxmanan, M. C. Flemings. Metallurgical and Materials Transactions A, 1980, 11A: 1927-1937.
[40] D.A. Pinsky, P.O. Charreyon, M.C. Flemings. Metallurgical and Materials Transactions B, 1984, 15B: 173-181.
[41] M. Suery, M.C. Flemings. Metallurgical and Materials Transactions A, 1982, 13A: 1809-1819.
[42] P.A. Joly, R. Mehrabian. Journal of Materials Science, 1976, 11: 1393-1418.
[43] A. Vogel, R. D. Doherty, B. Cantor, Solidification and Casting Metals, The Metals Society, London, 1979, 479.
[44] T. Z. Kattamis, T. T. Piccone. Materials Science and Engineering A, 1991, 131: 265-271.
[45] H.K. Moon. Rheological behaviour and microstructure of ceramic particulate /aluminum alloy composites, PhD thesis, MIT, Cambridge, MA: 1990.

[46] Y. Ito, M. C. Flemings, J. A. Corne. , edition J.A. Sekhar and J.A. Dantzig, Warrcndale, PA, TMS, 1992: 3-17
[47] Z. Fan, J. Y. Cen. Matererial Science and Technology, 2002, 18: 243-249.
48 J. M. M. Molenaar, L. Katgerman, W. H. Kool and R. J. Smeulders, Journal of Materials Science, 1986, 21: 389-394.
[49] M. Ferrante, E. de Freitas. Materials Science and Engineering A, 1999, A271: 172-180.
[50] C. Rouff. Contribution à la caractérisation et `à la modélisation du comportement d'un acier à l'état semi-solide-application au thixoformage, PH.D thesis, École Nationale Supérieure d'Arts et Métiers, Centre de Metz, Metz, France, 2003.
[51] O. Draper, S. Blackburn, G. Dolman, K. Smalley, A. Griffiths. Journal of Material Processing Technology, 1999, 92-93: 141-146.
[52] M. Ferrante, E. de Freitas, M. Bonilha, V. Sinka. 5th International Conference of Semi solid Processing of Alloys and Composites, 1998: 35-42.
[53] L. Lasa and J. M. Rodriguez-Ibabe. Materials science and Engineering A, 2003, A363: 193-202.
[54] G. Timmermans, L. Froyen. Wear, 1999, 230: 105-117.
[55] H. J. Kim. Materials Science and Technology, 2003, 19: 915-918.
[56] Metals Handbook, vol. 8th Edition, American Society for Metals, Materials Park, Ohio, 1973.
[57] S. C. Hansen, Antimony Modification of Aluminum-Silicon Alloys, PhD Thesis, University of Wisconsin-Madison, 2000.
[58] L. Arnberg, L. Bäckerud, G. Chai. American Foundry men's Society: solidification characteristics of Aluminum Alloys, Skanaluminium, Universitetsforlaget AS. Oslo, Norway, 1986, V.3: 137-144.
[59] J. E. Gruzleski, B. M. Closset, American Foundrymen's Society, Inc., Des Plaines, IL, USA, 1990, 16: 25-55.
[60] D. Apelian, J. L. Jorstad, R. DasGupta. Science and Technology of Semi-Solid Metal Processing. Edited by Anacleto de Figueredo, Worcester Polytechnic Istitute, Worcester, MA, 2001: 3-23
[61] Alireza Hekmat-Ardakan, Xichun Liu, Frank Ajersch, X.-Grant Chen, Wear, 2010,269: 684-692.
[62] Yavuz Sun, Hagrettin Ahlatci, Materials and Design, 2011, 32: 2983-2987.
[63] J. Zhang, Z. Fan, Y. Q. Wang, B. L. Zhou, Material Science and Engineering A, 2000, 281: 104-112.
[64] A. Mandal and M. M. Makhlouf." Microstructure and Mechanical properties of cast hypereutectic Al-Si alloys with high magnesium content ". TMS 2009: 57-62.
[65] Xiaochun Zeng, Makhlouf M. Makhlouf, Sumanth Shankar. Development of Novel Al-Si-Mg Alloys With 8 to 17 wt% Si and 2 to 4 wt% Mg, TMS 2007: 183-190.
[66] Alireza Hekmat-Ardakan, Frank Ajersch, X.-Grant Chen. Journal of Materials Science, 2011: 2370-2378.
[67] J. Zhang, Z. Fan, Y. Q. Wang, B. L. Zhou. Materials Science and Engineering A, 2000, A281: 104-112.

[68] R. Hadian, M. Emamy, N. Varahram, N. Nemati. Materials Science and Engineering A, 2008, 490: 250-257.
[69] J. Zhang, Z. Fan, Y. Q. Wang and B. L. Zhou. Materials science and Engineering A 2000, vol. A281: 104-112
[70] Q. D. Qin, Y. G. Zhao, W. Zhou, P. J. Cong. Materials science and Engineering A, 2007, 447: 186-191.
[71] Z. Zhang, Z. Fan, Y. Q. Wang, B. L. Zhou. Journal of Materials Science Letters, 2000, 19: 1825-1828.
[72] Y. G. Zhao, Q. D. Qin, Y. H. Liang, W. Zhou, Q. C. Jiang. Journal of Materials Science, 2005, 40: 1831-1833.
[73] J. Zhang, Z. Fan, Y. Q. Wang, B. L. Zhou. Scripta Materialia, 2000, 42: 1101-1106.
[74] Alireza Hekmat-Ardakan, Frank Ajersch, Acta Materialia, 2010, 58: 3422-3428.
[75] J. Jorstad, D. Apelian. International Journal of Metalcasting, summer, 2009: 13-36.
[76] F. A. Crossley, L. F. Mondolfo, Mechanism of grain refinement in aluminum alloys, Journal of Metals — Transactions of the American Institute of Mining and Metallurgical Engineers, décembre 1951, vol. 191: 1143-1148.
[77] A. Dahle, K. Nogita, S. McDonald, C. Dinnis, L. Lu. Materials Science and Engineering A, 2005, vol. 413-414: 243-248.

CHAPTER 3

EXPERIMENTAL PROCEDURES

CHAPTER 3

EXPERIMENTAL PROCEDURES

The current investigation is divided into three sections. In the first section, the effect of phosphorus, strontium and processing parameters on the processability and microstructure of semi-solid 390 alloy was studied. Due to the difficulties in semi-solid rheoforming of hypereutectic 390 alloys, a new variation of the SEED rheocasting process that consists of isothermal holding and addition of solid metal in the melt was adapted to produce semi-solid billets of 390 alloy. The effects of isothermal holding and the addition of solid metal on the semi-solid microstructure and the temperature gradient within the slurry were also investigated.

The second experimental section describes the methods used in two parts: 1) to investigate the solidification and microstructural evolution of Al-Si-Mg-Cu quaternary alloys containing different Mg concentrations, 2) to study effect of P and Sr on the modification of the microstructure of Al-15Si-14Mg-4Cu alloy. A study of the thermodynamic calculation of hypereutectic Al-Si-Mg-Cu alloys with different Mg contents was first carried out using the Thermo-Calc software. The results were then compared with DTA (Differential Thermal Analysis) and microstructural observations. One alloy Al-15Si-14Mg-4Cu was specifically selected from the Al-Si-Mg-Cu alloys studied, which showed a coarse dendritic primary Mg_2Si phase. The effect of phosphorus and

strontium additions on the primary Mg_2Si particles, eutectic (Mg_2Si+Si) and π-Fe intermetallic compound in this alloy was investigated.

The third section was designed to study the effect of shear rates, solid fraction, primary particle size and chemical composition on the rheological properties and microstructure of semi-solid hypereutectic Al-Si-Mg-Cu alloys. In this section four alloys were selected from the first and the second sections namely two 390 (unrefined and P-refined) and two Al-15Si-xMg-4Cu alloys with 10.5 and 13.5% Mg contents.

3.1 Section I: Effect of P, Sr and processing parameters on the processability and microstructure of semi-sold 390 alloy

In this section, a commercial A390 alloy was used to produce the semi-solid material. Its chemical composition is listed in Table 3.1.

Table 3.1 Chemical composition of alloys used in the present work (wt. %)

Alloy #	Elements (wt. %)							
	Si	Cu	Mg	Fe	Mn	Ti	Zn	Al
390	17.1	4.48	0.55	0.36	0.02	< 0.01	< 0.05	Bal.
356	7.12	0.01	0.4	0.1	0.01	0.12	< 0.01	Bal.

Due to difficulties in semi-solid rheoforming of the hypereutectic 390 alloys, a new variation of the SEED rheocasting process was used. It consists of isothermal holding and addition of solid metal to the melt to produce semi-solid slurries of 390 alloy. The experimental setup is shown in Figure 3.1. It consists of an insulated steel crucible, a device for adding solid pieces of alloy and the SEED apparatus. The process steps to produce the semi-solid slurry are illustrated in Figure 3.2.

First, 24 kg of alloy was heated to the liquid state at 750 °C in a 30kg capacity refractory crucible, using an electrical resistance furnace. In each test, approximately 1.5kg of the melt was carefully poured at 660 °C into a crucible of 85 mm in diameter and 250mm in depth. Two K-type thermocouples were placed in the crucible prior to pouring, one at the center and the second near the wall of the crucible, to monitor the temperature gradient in the slurry during solidification. The tips of the thermocouples were positioned at 70mm from the bottom of the crucible. The molten metal was then swirled at 150RPM or 2.5Hz, using the SEED process. After pouring the liquid metal into the crucible, two kinds of solid metal pieces with different quantities were added to the molten metal during swirling. The first addition is pieces of 390 that have the same composition as the melt in the crucible, followed by a second addition of a 356 solid piece with the chemical composition shown in Table 3.1. The weights of the 390 and 356 solids pieces are 50g and 40g, respectively. The duration of the swirling stage depends on the mold dimension and the charge mass and for these experiments and in general it was set to 280 seconds. In the next step, the swirling motion was stopped and the melt was held isothermally for 40 seconds. Finally, the semi-solid slurry was demoulded from the crucible and rapidly quenched in cold water. In other tests, phosphorus or phosphorus combined with strontium was added to the liquid metal to refine the primary Si and modify the eutectic Si of the alloys.

Metallographic specimens were cut from the quenched slurry and polished using standard metallographic procedures. The microstructure was examined using optical microscopy. A CLEMEX JS-2000 optical image analyser was used to quantify the volume fraction of α-Al and the particle size of the primary Si particles.

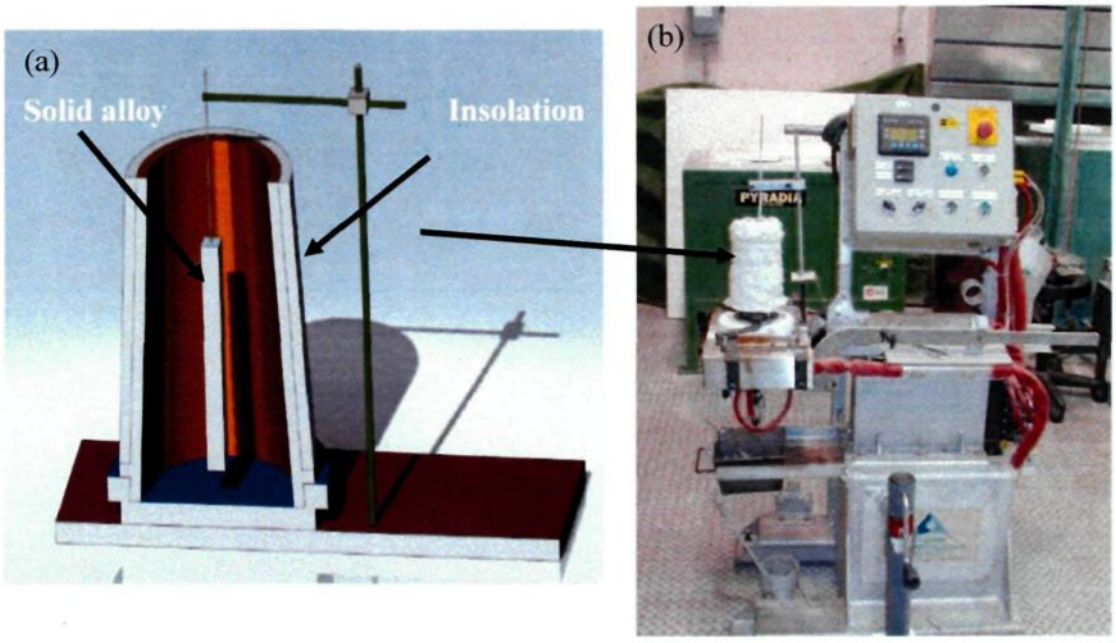

Fig. 3.1 (a) Schematic and (b) an actual overview of new variation of SEED rheocasting process.

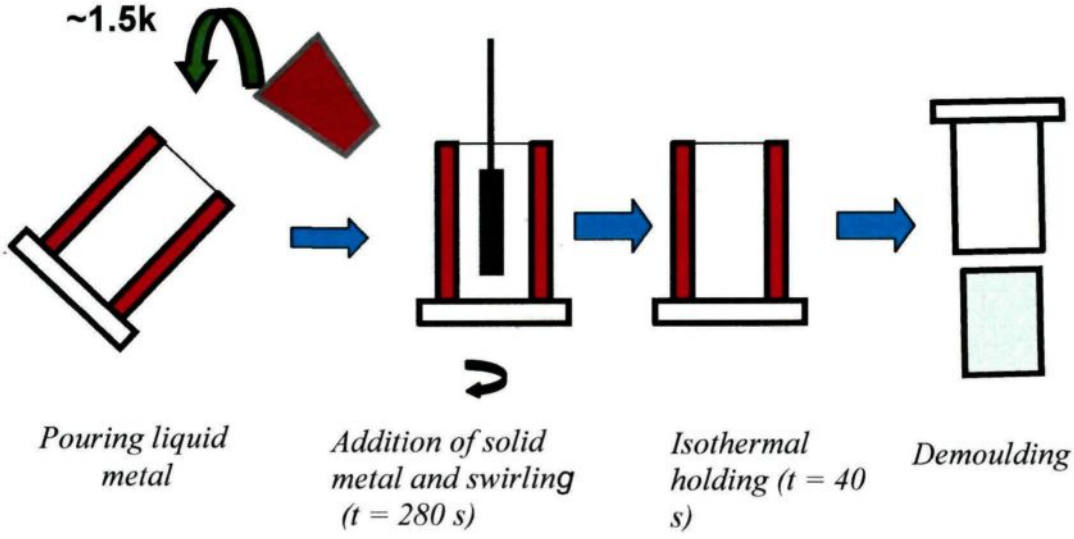

Fig. 3.2 Illustration of the steps involved in the new variation of the SEED rheocasting process.

3.2 Section II - Part 1: investigating the solidification and microstructural evolution of Al-Si-Mg-Cu quaternary alloys containing different Mg concentrations

Based on the phenomenological or Calphad approach [1] of calculating phase diagrams and thermodynamic equilibria in alloys of interest to materials scientists, ThermoCalc, a software package for calculation of phase equilibria, was also employed to understand solidification and phase formation in multicomponent alloys. In this part, ThermoCalc was used to investigate the effect of high Mg contents on the solidification sequence of the hypereutectic Al-Si-Mg-Cu system. Thermodynamic variables were computed using the AA12Br database. In addition, the thermodynamic calculations were compared with the thermal analysis results and microstructural observations obtained from the experimental data.

A commercial 390 alloy, and Al-50%Si and Al-50%Cu master alloys were used as starting materials to prepare the Al-15Si-xMg-4Cu alloys. About 2.5kg of the prepared alloy was melted in a clay-graphite crucible, and the temperature of the melt was maintained at 780 ^{o}C ± 10 ^{o}C. Small blocks of pure magnesium (99 wt. % purity) preheated at 250 ^{o}C and wrapped in aluminum foil were added to the melt with an extra 20% of the target composition in order to compensate for the oxidation of magnesium. The alloys were melted in an electrical resistance furnace under controlled argon atmosphere. Stirring was carried out after each Mg addition. Samplings for chemical analysis were taken from the corresponding melts. For the thermal analysis, the melt was then poured into a thin shell steel crucible which had been preheated by immersion in the liquid metal for about 1 minute. Table 3.2 lists the chemical analyses of the four alloys studied.

Table 3.2 Alloy Codes and Compositions (wt. %)

Alloy #	Elements (wt. %)				
	Si	Mg	Cu	Fe	Al
A	15.1	6.2	4.0	0.4	Bal.
B	15.5	8.4	4.0	0.4	Bal.
C	15.4	12.8	4.2	0.3	Bal.
D	15.5	14.9	4.0	0.3	Bal.

To confirm the thermodynamic calculation results, cooling curves were obtained for the various alloys studied by placing two K-type thermocouples at the center and at the wall of a preheated steel crucible into which the melt sample was poured, and the temperature-time data during solidification were recorded, using a data acquisition system (National Instruments NI SCXI-1531). The thermal analysis set-up provided a cooling rate of 0.6 ^{o}C/s, as obtained above the liquidus temperature. Fig. 3.3 shows the schematic illustration of the thermal analysis setup.

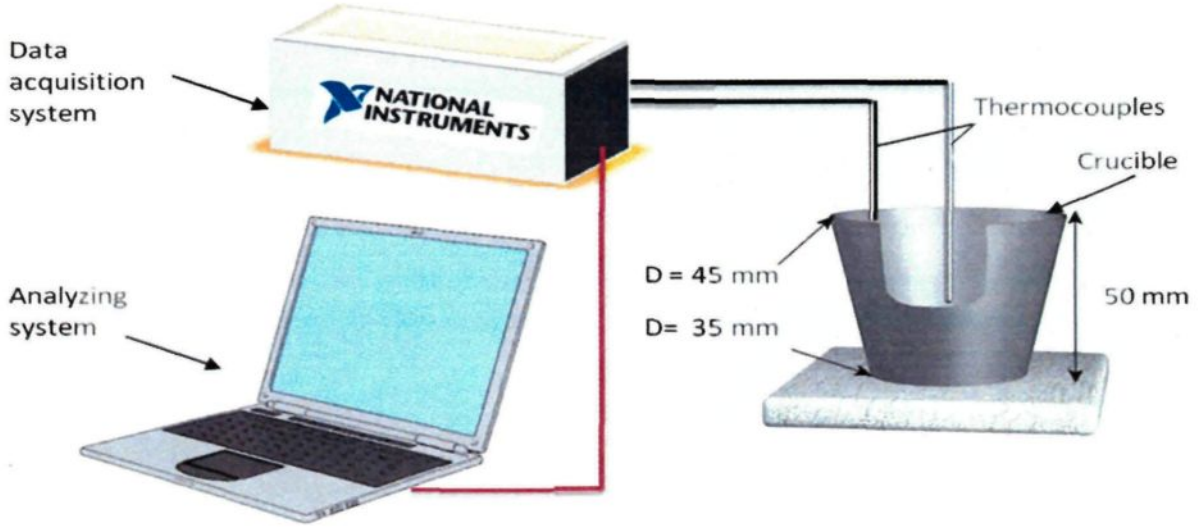

Fig. 3.3 Schematic illustration of the thermal analysis setup.

In order to study the effect of Mg on the microstructural evolution of the alloys studied, samples were sectioned from the corresponding thermal analysis castings (~150g) from the central part containing the thermocouple tip, then polished for microstructural examination using standard metallographic procedures. Some samples were also deep-etched for 10 minutes in 10% NaOH solution for better delineation of the 3D morphology of the Mg_2Si and Si particles. The microstructures were examined using optical microscopy and the various phases observed were identified using scanning electron microscopy (JEOL JSM-6480LV) and EDS analysis. The volume fractions of Mg_2Si and Si phases were quantified using an image analysis system (Clemex JS-2000) coupled with the optical microscope.

3.3 Section II - Part 2: Effect of P and Sr on the modification of the microstructure of Al-15Si-14Mg-4Cu alloy

In this part, one alloy Al-15Si-14Mg-4Cu was selected from the Al-Si-Mg-Cu alloys studied in section II-part I. In each test, approximately 2 kg material was melted in a graphite crucible using an electric resistance furnace. The Cu-8% P and Al-10% Sr master alloys preheated at 300 °C were added into the melt at 800 °C. After being held for 20 minutes, the hypereutectic Al-15Si-14Mg-4Cu melts were poured into steel dies to produce ingots. The chemical compositions of the alloys prepared are listed in Table 3.3.

Table 3.3 Alloy Codes and Compositions (wt. %)

Alloy #	Elements (wt. %)						
	Si	Mg	Cu	Fe	P	Sr	Al
1	15.5	13.6	4.3	0.3		-	Bal.
2	15.5	13.5	4.3	0.4	0.4	-	Bal.
3	15.1	13.9	4.6	0.4		0.08	Bal.
4	15	13.8	4.1	0.3	0.4	0.08	Bal.

Thermal analysis was performed to determine eutectic nucleation temperature (T_N), growth temperature (T_G), and minimum temperature (T_{Min}). The characteristic temperatures are identified as the point where the cooling curve starts to bend and is detected more easily with the help of the first derivative of the cooling curve. The difference between T_G and T_{Min} describes the recalescence ΔT of the eutectic arrest. The different temperatures, T_N, T_G and T_{Min} are shown in Fig. 3.4.

The eutectic Si and eutectic Mg_2Si particle characteristics were quantified using an image analyzer (CLEMEX JS- 2000, PE 4.0) attached to the optical microscope, following the usual procedures employed for volume fraction or other measurements of any specified phase. The various phases observed in these samples were identified using optical microscopy and scanning electron microscopy (SEM) coupled with energy dispersive X-ray spectroscopy (EDS).

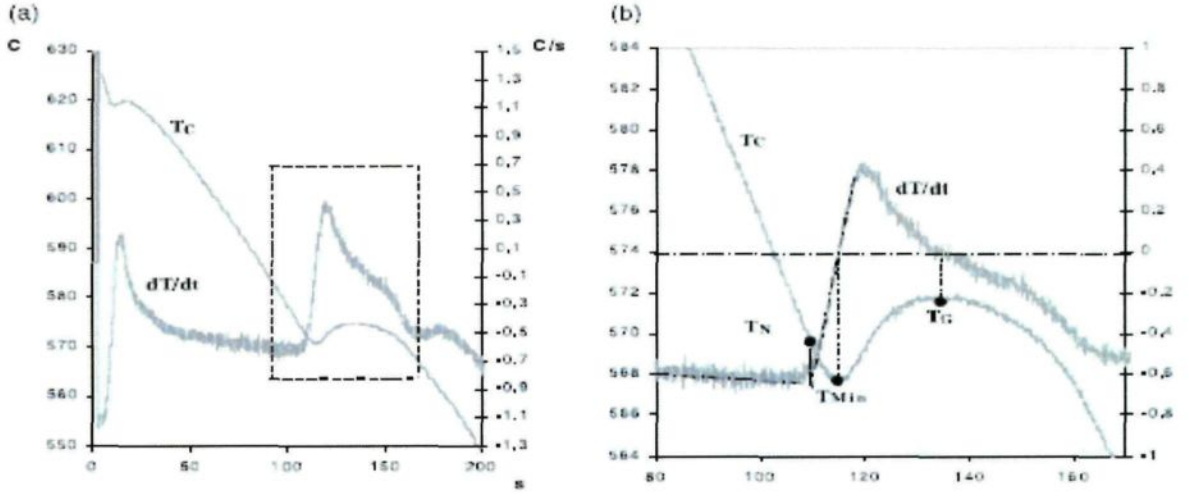

Fig. 3.4 Cooling curve, (a) first derivative and (b) representation of nucleation, growth and minimum temperatures.

3.4 Section III: Rheological properties and microstructure of semi-solid hypereutectic Al-Si-Mg-Cu alloys

The materials used for this section were hypereutectic Al-17Si-4Cu (A390), P-refined Al-17Si-4Cu (A390), and two P-refined Al-15Si-xMg-4Cu alloys with 10.5 and 13.5% Mg contents. To refine the primary Si and Mg_2Si phases, a certain amount of Cu-8% P master alloy was added into the alloy melts. Table 3.4 shows the chemical compositions of the experimental alloys used for rheological study in this project.

Table 3.4 Alloy Codes and Compositions (wt. %)

Alloy #	Elements (wt. %)					
	Si	Mg	Cu	Fe	P	Al
1	17.1	0.55	4.5	0,4	-	Bal.
2	17.1	0.55	4.5	0,4	0,01	Bal.
3	15	10.5	4	0,4	0,4	Bal.
4	15	13.5	4.1	0,4	0,4	Bal.

In this section, two methods were used to produce semi-solid slurries of the studied alloys, namely conventional SEED rheocasting process (Fig. 3.5) and a new variation of the

SEED rheocasting process (Fig. 3.2). The new variation of the SEED process was employed to produce semi-solid slurries of unrefined 390 and P-refined 390 alloys. Details of the novel experimental method were reported in section 3.1 of Chapter 3. For Al-15Si-10.5Mg-4Cu and Al-15Si-13.5Mg-4Cu alloys, the conventional SEED rheocasting process was used (Fig. 3.5). A 1.5 kg melt at 710 °C was poured into the cylindrical steel crucible, and swirled at 150 RPM and held down to a given temperature. The duration of the swirling and holding for both alloys was 180 seconds and 30 seconds, respectively. In each test, the semi-solid billet had a diameter of 75 mm and a height of about 160 mm. A K-type thermocouple was installed at the billet center to monitor the temperature change during solidification. The schematic diagram of the conventional SEED rheocasting process is shown in Fig. 3.5.

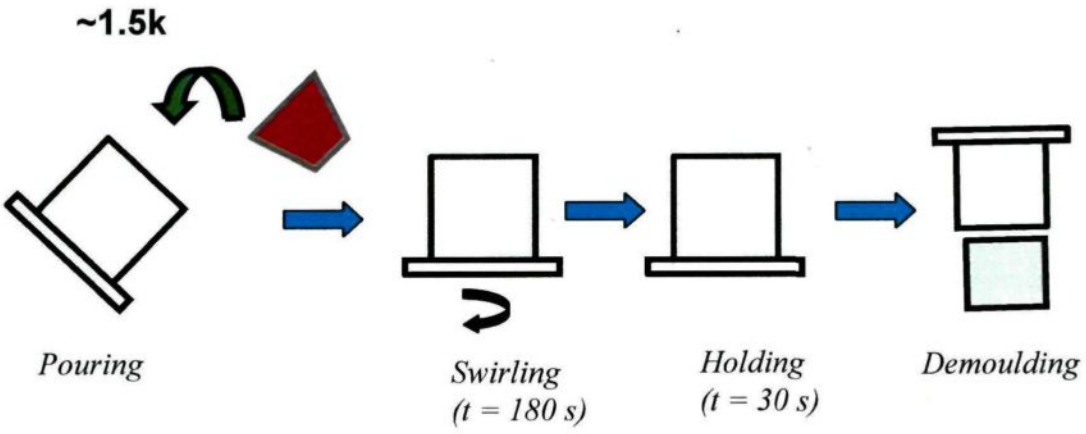

Fig. 3.5 Illustration of the steps involved in the conventional SEED process.

The working temperatures for compression tests were 560, 558, 552 °C for A390 alloy, 550, 548, 543 °C for Al-15Si-10.5Mg-4Cu alloy, and 548 °C, 544 °C, 538 °C for Al-15Si-13.5Mg-4Cu alloy, which corresponded to solid fractions of 0.4, 0.5 and 0.6 of these alloys,

respectively. The relation of solid fraction as a function of temperature for the 390 alloys was calculated from the thermal analysis, using the Newtonian method [2]. The relation of solid fraction vs. temperature for both Al-15Si-10.5Mg-4Cu and Al-15Si-13.5Mg-4Cu alloys was calculated from ThermoCalc simulation.

When the melt temperature at the billet center reached to one of the working temperatures, the billet was quickly taken out of the mould and transversely sectioned at 60 mm from the bottom. The rest of the billet (75 mm in diameter and about 100 mm in height) was transferred and compressed uniaxially in a parallel plate compression machine by applying different dead weights (Fig. 3.6) [3]. The applied dead weight varied between 3.7-10.5 kg and the change in the billet height was registered versus time using a National Instrument data acquisition unit, NI SCXI-1531. An electric resistance furnace was mounted on the press bed to keep the billet temperature constant during the course of the deformation. Two K-type thermocouples were positioned within the furnace to control the chamber and to monitor the billet temperature. After compression, the deformed billets were taken out of the furnace and quenched immediately in cold water. Some quenched billets were sectioned in the regions between the center and the wall of the billet as shown in Fig. 3.7. The microstructures were examined using an optical microscope.

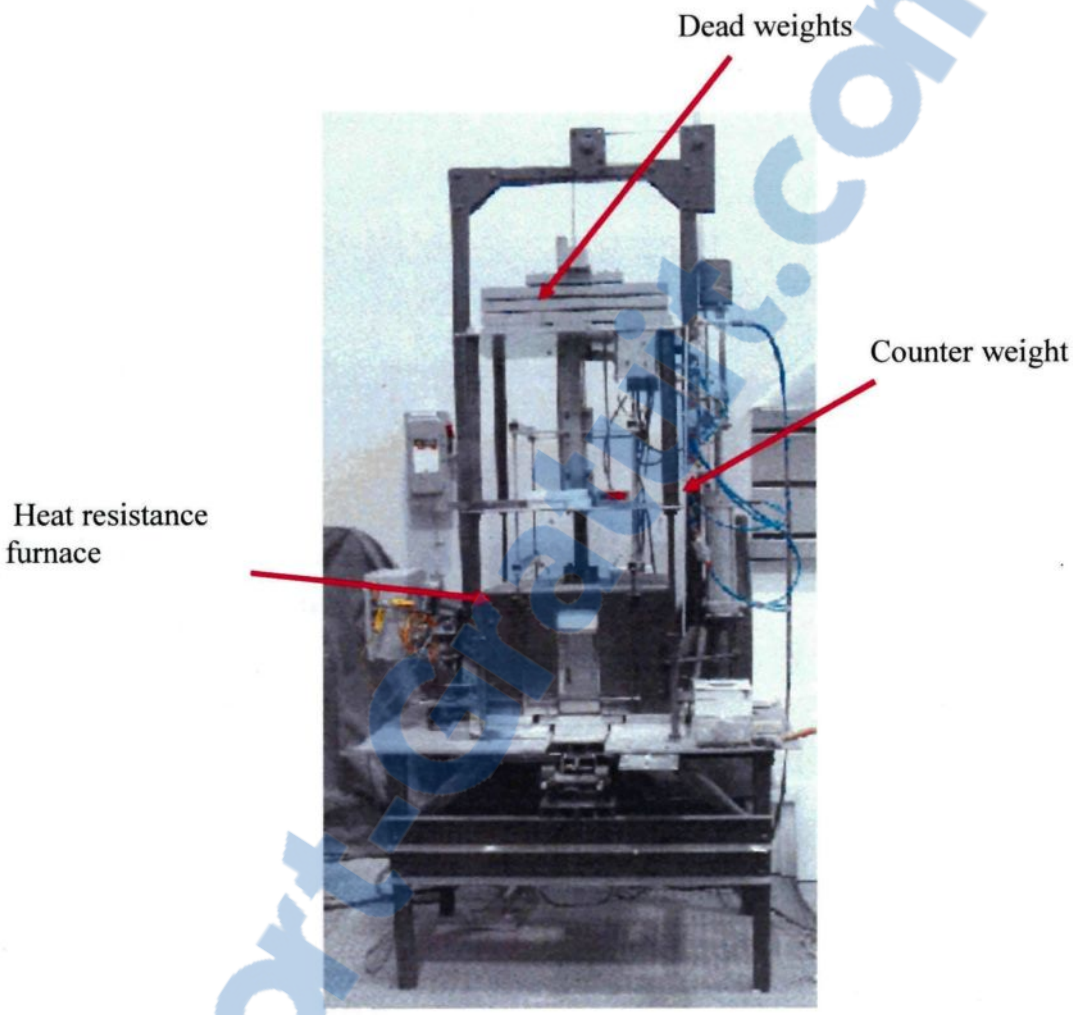

Fig. 3.6 An overview of the parallel plate compression test machine.

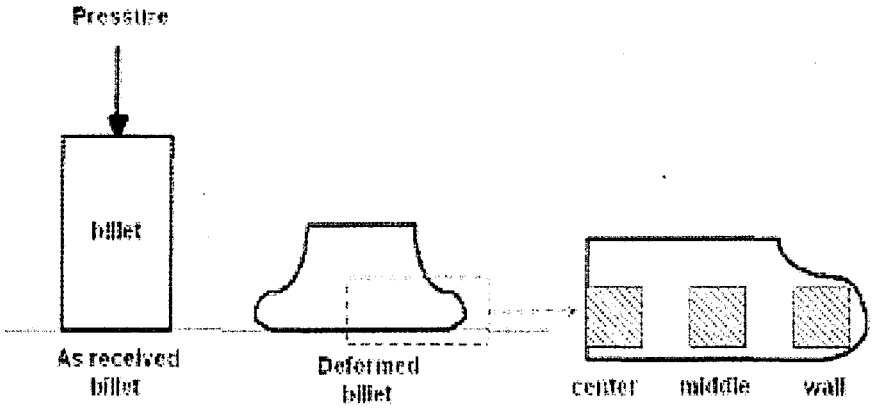

Fig. 3.7 Area of samples sectioned for optical microscope observations for a typical deformation.

3.5 Microstructure observations

3.5.1 Optical microscopy

For each of the experimental sections, an optical microscope (Nikon Eclipse ME600) was used to examine the microstructures of the alloys studied. The samples were mounted and polished down to 0.5 micron diamond suspension finish. Quantitative analyses were carried out using an optical microscope coupled to a Clemex image analyser.

3.5.2 Scanning electron microscopy (SEM)

A scanning electron microscope (SEM, JSM-6480LV) equipped with energy-dispersive X-ray spectroscopic (EDS) facilities was also used to examine the microstructure of the Al-Si-Mg-Cu alloys studied in section II . To reveal the three-dimensional morphology of phase constituents, the metallographic samples were deep-etched with 0.5 % HF for 10 minutes. An HKL Channel 5 EBSD system attached to the SEM (JSM–6480LV) was employed for phase identification purposes.

References

[1] Y. Austin Chang, Shuanglin Chen, Fan Zang, Xinyan Yan, Fanyou Xie, Rainer Schmid-Fetzer, W. Alan Oates. Progress in Materials Science, 2004, 49: 313-345.
[2] P. Marchwica, J. H. Sokolowski, W. T. Kierkas. Journal of Achievements in Materials and Manufacturing Egineering, 2011, 47-2: 115-136.
[3] Omid Lashkari, Reza Ghomashchi. Materials and Design, 2007, 28: 1321-1325.

CHAPTER 4

SEMI-SOLID HYPEREUTECTIC AL-SI-CU 390 ALLOYS USING RHEOFORMING PROCESS

CHAPTER 4

SEMI-SOLID HYPEREUTECTIC AL-SI-CU 390 ALLOYS USING RHEOFORMING PROCESS

4.1 Introduction

Hypereutectic 390 alloys (Al-17Si-4Cu) have generated significant interest in recent years, due to their attractive properties, such as low coefficient of thermal expansion, high wear resistance, high strength and hardness [1-3] and are widely used in the automotive and aerospace industry. Typical applications are: pistons, cylinder blocks and AC compressors [3]. However, the semi-solid processing of 390 alloys presents considerable difficulties due to the segregation of large primary silicon particles, the wide range of solidification and a large proportion of eutectic, resulting in poor processability of the semi-solid slurry [4].

Semi-solid metal (SSM) processing is a relatively new technology for near-net-shape manufacturing, which was discovered in early 1971 by Spencer [5]. The most common process routes are thixoforming, where the prefabricated billet is reheated to the semi-solid state prior to casting, and rheoforming which generally starts with molten metal that is processed directly into semi-solid slurry by controlled cooling resulting in an appropriate non-dendritic structure (slurry on demand) [5].

It has been reported that thixoforming was successfully used to produce hypereutectic 390 semi-solid cast parts [6-8]. In this process, the partial remelting and isothermal holding promoted the separation of α-Al and Si eutectic phases and increased the amount of non-

dendritic α-Al, resulting in a suitable microstructure for forming semi-solid slurry [9]. However, thixoforming is not the most economical route for semi-solid processing.

Recently, a new concept of rheoforming has been explored because of its many obvious advantages. It consists of a simple process step from liquid metal to slurry with a large capability to use all possible material sources (primary, secondary, selected process and recycled scrap) [10-12]. However, semi-solid processing of hypereutectic A390 alloy by rheoforming presents certain difficulties, such as a small processing temperature window, a high heat of fusion of silicon, a long solidification time and a segregation of primary silicon particles. These factors led to of the development of innovative methods to achieve an acceptable semi-solid microstructure for rheoformed hypereutectic alloys. Saga *et al.* [4] have introduced two novel methods using diffusion solidification as a means to extract heat from the slurry. The two concepts are a) mixing hypoeutectic alloy with hypereutectic alloy at different temperatures and b) cooling of the liquid hypereutectic alloy with the addition of solid particles. To date, there are still only few publications on the rheoforming of hypereutectic Al-Si-Cu alloys.

The SEED process (Swirl Enthalpy Equilibration Device) is a slurry-on-demand process that involves the application of mechanical mixing (swirling), which allows the extraction of a controlled amount of heat from the molten alloy to generate a semi-solid mixture [12]. This method is well adapted to the processing of 356/357, 6061 and 206 semi-solid alloys.

In this chapter, a modification of the SEED process, including isothermal holding in an insulated mould together with the addition of solid alloy during swirling is described, which was employed to improve the processability of the semi-solid slurry. The effects of

isothermal holding and the addition of solid alloy on the semi-solid microstructure and on the temperature gradient within the slurry were investigated. The impact of phosphorus and strontium on the primary and eutectic silicon structure was also explored.

4.2 Materials and Methods

In this section, a combination of the SEED process, isothermal holding using insulation and addition of solid alloy during swirling was introduced as a novel method to improve the processability of semi-solid slurry. Details of the experimental method can be found in Chapter 3.

First, approximately 1.5kg of alloy was heated to the liquid state at 750 °C in a 30 kg capacity refractory crucible, using an electrical resistance furnace. The molten metal was then swirled using the SEED process with the addition of solid alloy pieces. After swirling, the melt was held isothermally for ten seconds. The molten metal was then carefully poured at 660 °C into a crucible of 85 mm in diameter and 250 mm in depth. Two K-type thermocouples were placed in the crucible prior to pouring, one at the center and the second near the wall of the crucible, to monitor the temperature gradient in the slurry during solidification. The tips of the thermocouples were positioned at 70 mm from the bottom of the crucible. Finally, the semi-solid slurry was demoulded from the crucible.

A commercial A390 alloy was used to produce the semi-solid material. Its chemical composition is listed in Table 4.1. During swirling, two different quantities of solid alloys were added to the molten metal. The first addition of A390 has the same composition as the melt in the crucible, followed by a second addition of A356 solid alloy with the chemical composition shown in Table 4.1. In other tests, phosphorus or phosphorus combined with

strontium was added to the liquid metal to refine the primary Si and modify the eutectic Si of the alloys.

After demoulding, the semi-solid slurry was rapidly quenched in water. Metallographic specimens were cut from the quenched slurry and polished using standard metallographic procedures. The microstructure was examined using optical microscopy. A CLEMEX JS-2000 optical image analyser was used to quantify the volume fraction of α-Al and the particle size of the primary Si particles.

Table 4.1 Chemical compositions of alloys added to molten metal to prepare semi-solid A390 alloy

Alloy #	Elements (wt. %)							
	Si	Cu	Mg	Fe	Mn	Ti	Zn	Al
390	17.1	4.48	0.55	0.36	0.02	< 0.01	< 0.05	Bal.
356	7.12	0.01	0.4	0.1	0.01	0.12	< 0.01	Bal.

4.3 Results and Discussion

4.3.1 Effect of processing parameters

Figure 4.1 compares the temperature profiles at the wall and at the center of the slurry using the conventional SEED process and the modified method. The crucible and pouring temperatures were fixed at 50°C and 670°C respectively in the tests. Figure 4.1a shows the thermal history of the slurry using the SEED process. It can be seen that the initial measured temperatures were 619 °C and 592 °C at the centre of the melt and at the mid height of the crucible wall. The radial temperature gradient during the initial stage of cooling is very large because of the temperature difference between the mould and the liquid alloy. This temperature gradient decreases rapidly while swirling for the first 50s as

the temperature of the crucible mould increases. After 100s, the temperature at the centre remained almost constant, whereas the temperature at the wall continued to slowly decrease resulting in a temperature gradient of 6°C at the final stage.

The temperature profile using the modified method is shown in Figure 4.1b. After pouring, the initial temperature difference between the wall and the centre is small due to the insulation of the crucible. It can be seen that after the solid alloy addition (at 50-60s), the temperature gradient almost disappears. The results of Figure 4.1b clearly illustrate the effectiveness of the insulation of the crucible and the addition of the solid alloy with swirling which allows high heat extraction from the centre of the slurry. Consequently the temperature of the slurry becomes much more uniform for an extended period of time from 100 to 320s in the semi-solid range at 560°C. At the final stage, the temperature difference in the slurry is only 0.5°C, compared to 6°C for the conventional SEED process.

Processing of hypereutectic Al-Si-Cu alloys, such as A390 using the SEED process resulted in a hard solid layer at the solidification surface with a high liquid content zone at the center of the ingot. These ingots were difficult to demould and were not self-supporting, which made them unsuitable for further die casting. The long period of constant temperature and the addition of solid metal in the modified process resulted in the successful rheoprocessing of A390 alloy by the separation of the α-Al and the Si eutectic phases and an increase of the volume fraction of the non-dendritic α-Al phase. The resulting slurry could easily be demoulded, was self-supporting and could be easily sliced as shown in Figure 4.2a and 4.2b, indicative of the good processability of the alloy using the modified method.

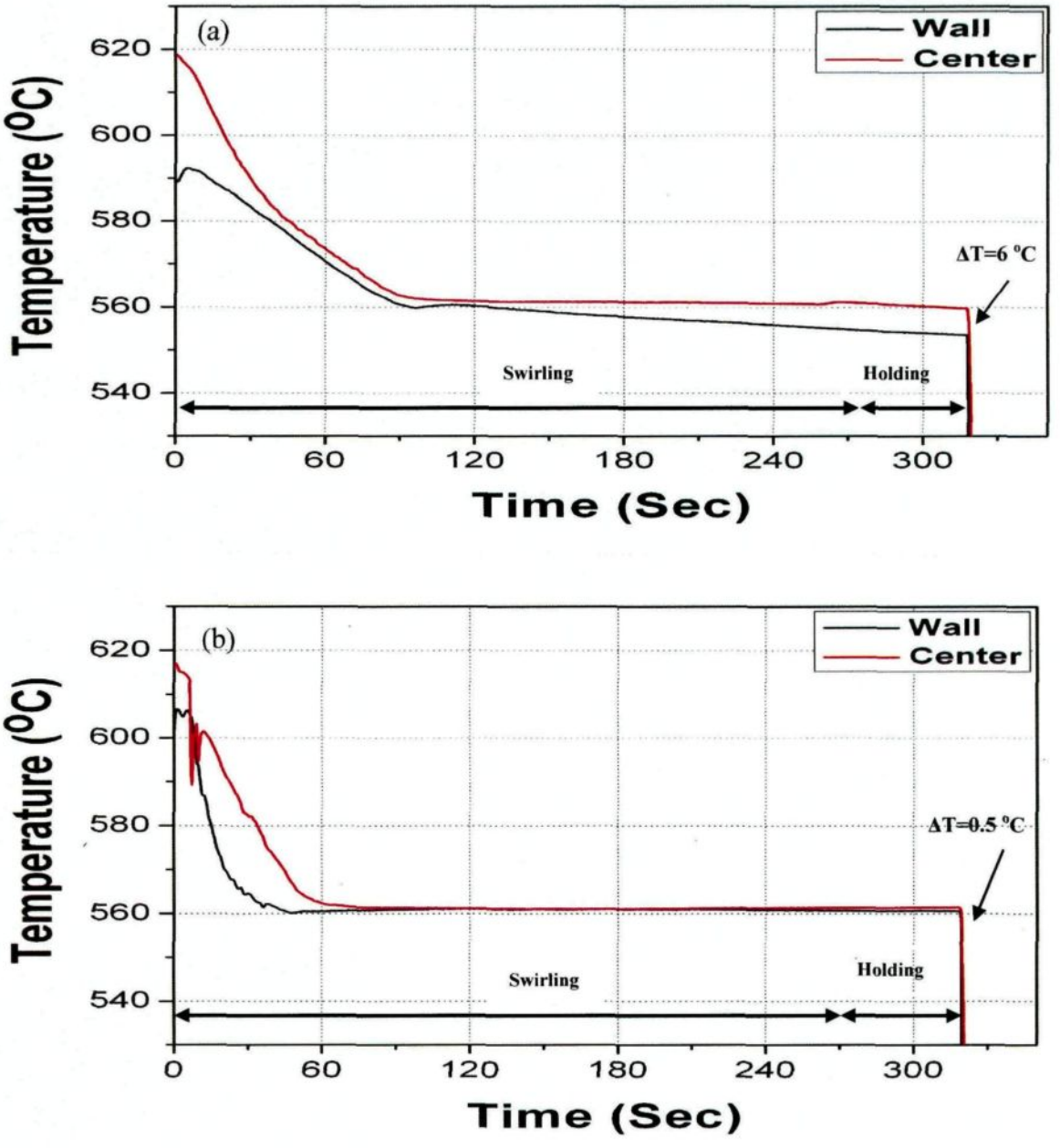

Fig. 4.1 Temperatures measured at the wall and at the center of the crucible mold during the production of semi-solid slurries: (a) Conventional SEED process; (b) Modified method.

(a) (b)

Fig. 4.2 The novel method of preparing the semi-solid slurries provides ingots that are self-supporting and easy to cut.

4.3.2 Microstructures of the rheoprocessed alloys

Figure 4.3 shows the microstructures in the center part of semi-solid slurries produced a) by the conventional SEED process and b) by the modified method. All slurries were quenched at 560°C. Slurries obtained by the conventional SEED process show large primary Si particles mostly in the form of clusters, a few dendrite-rosette α-Al particles and a large amount of eutectic liquid (Fig. 4.3a). Using the novel method, slurries show a significant increase in volume fraction of globular α-Al, resulting in an acceptable microstructure with rheological properties suitable for subsequent rheocasting (Fig. 4.3b). With the novel method, the SEED process provides good mechanical mixing and the insulation reduces the heat loss at the wall. Also, the addition of solid alloy at the centre reduces the heat flux from the molten alloy to the crucible wall and extracts the high heat of fusion released by the precipitation of the primary silicon particles. The addition of solid

metal also contributes to the massive nucleation of α-Al. This combined effect promotes the separation of α-Al and Si eutectic phases and increases the amount of globular α-Al.

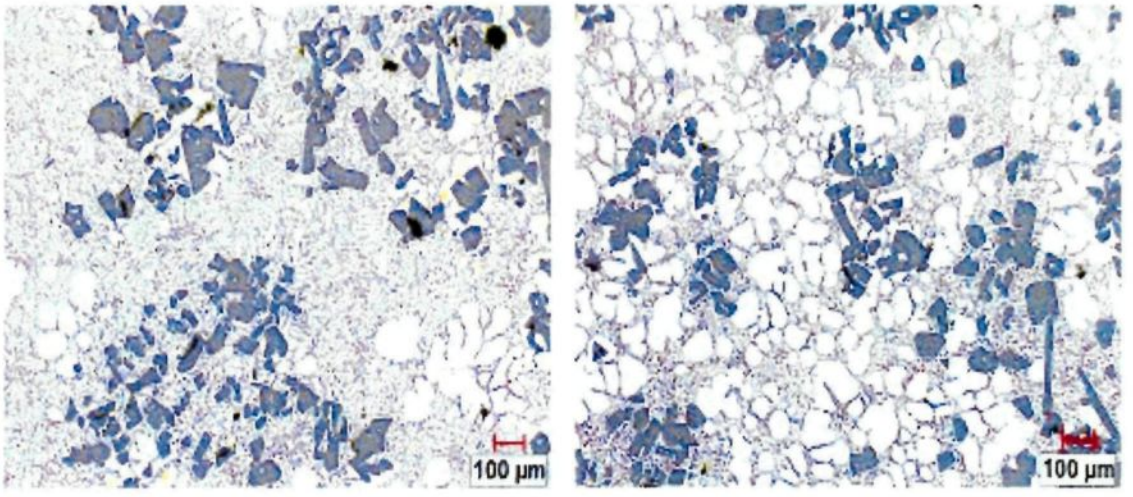

(a) (b)

Fig. 4.3 Microstructure of semi-solid A390 obtained using a) conventional SEED process and b) modified SEED process.

Figure 4.4 shows the effect of different solid alloy additions on the microstructure of semi-solid slurries prepared using the novel method. It can be seen from Fig. 4.4a and Fig. 4.4b that the amount of solid alloy addition has a significant effect on the microstructure. As the amount of A390 alloy increases from 50g to 85g, the solid fraction of α-Al increases. The results show that the addition of small amount of solid alloy removes the heat from the liquid at a rapid rate that promotes the nucleation of α-Al. The isothermal holding at the temperature near the eutectic point enhances the separation of α-Al and Si eutectic phases, and therefore, the Al in the solution can easily precipitate on the existing α-Al. Figure 4.4c presents the microstructure obtained with a combined addition of A390 and A356 alloys during swirling. The addition of two different compositions of solid alloys

significantly increases the volume fraction of the α-Al particles, when compared to the results obtained with the addition of A390 only (Fig. 4.4a and 4.4b). The increase in the volume fraction of α-Al is due to the nucleation and growth of α-Al by the dissolution of aluminum phase from the A356 solid alloy and by subsequent diffusion solidification [4].

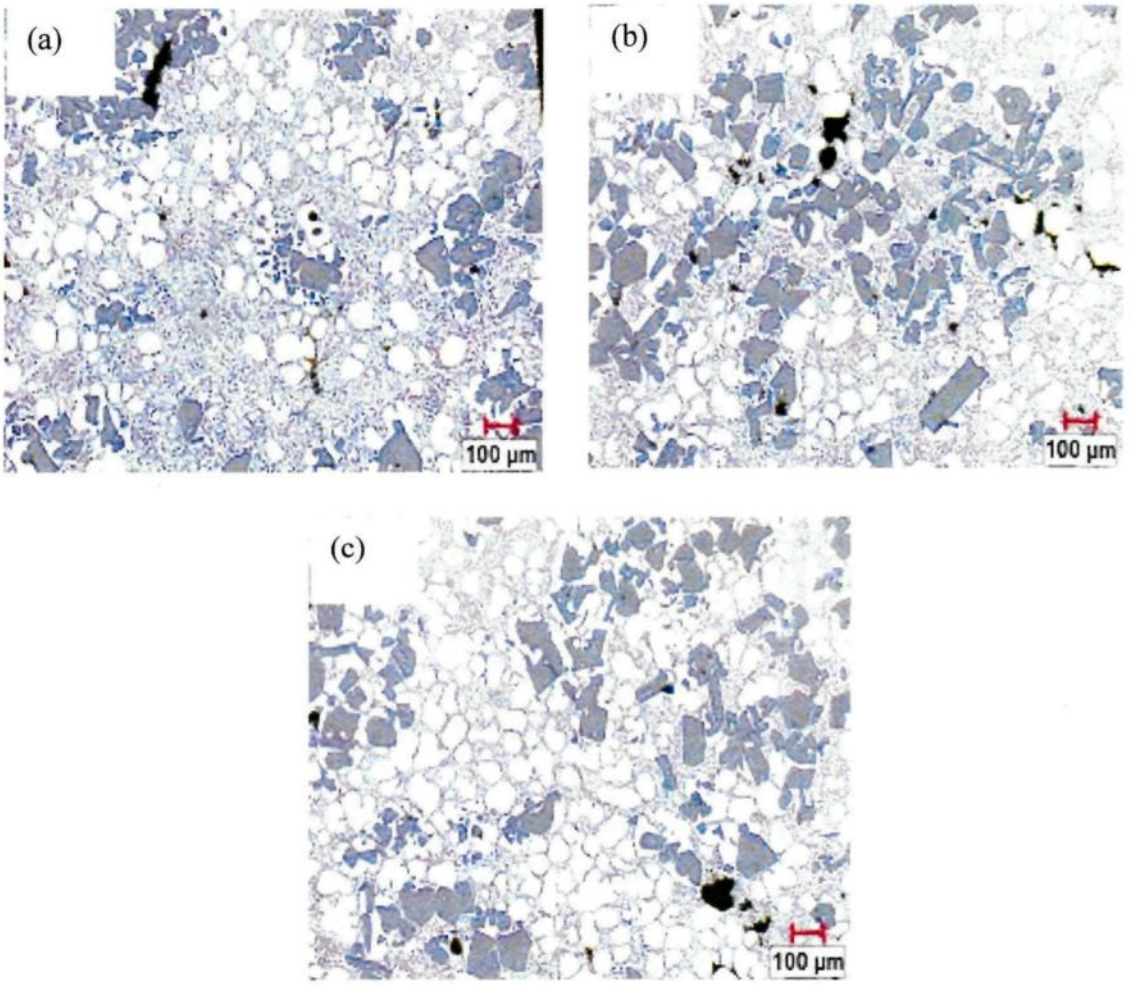

Fig. 4.4 Effect of the amount of addition of solid alloy on the microstructure of A390 slurry, a) 50g (A390), b) 85g (A390), c) 50g (A390) + 42g (A356).

The effects of the addition of phosphorus and strontium on the microstructure of semi-solid A390 slurries are shown in Figure 4.5. Primary silicon in untreated A390 alloy

generally takes the form of coarse platelets with an irregular morphology as shown in Figures 4.3 and 4.4. After the addition of 88 ppm P in the form of a Cu-8%P master alloy, the size and the morphology of primary silicon particles was changed to a fine blocky shape with a considerable decrease in size (Fig. 4.5a). It should be noted that during the preparation of the slurry, the fine primary silicon particles also have a tendency to agglomerate. It was previously reported that phosphorus can react with the liquid aluminum to form aluminum phosphide, AlP, which has a crystal structure very similar to that of silicon [14]. It is evident that primary Si nucleates heterogeneously on the AlP particles, which promotes the refinement of the primary silicon. However, the phosphorus refinement has no effect on the eutectic silicon, which remains in a lamellar plate like form (Fig. 4.5 b).

Figure 4.5c shows the effect of the addition of both phosphorus and strontium to the molten metal. Examination of the resulting microstructure showed that the size and morphology of primary silicon particles were slightly affected. Most of the primary silicon remained coarse and had an irregular morphology, while the morphology of eutectic silicon changed considerably to a fine fibrous form (Fig. 4.5d). This phenomenon is probably due to the interaction of the added elements. It was also previously reported that refinement of primary silicon and modification of silicon eutectic cannot be achieved simultaneously because the AlP particles are consumed by strontium to form Al_2Si_2Sr [14, 15].

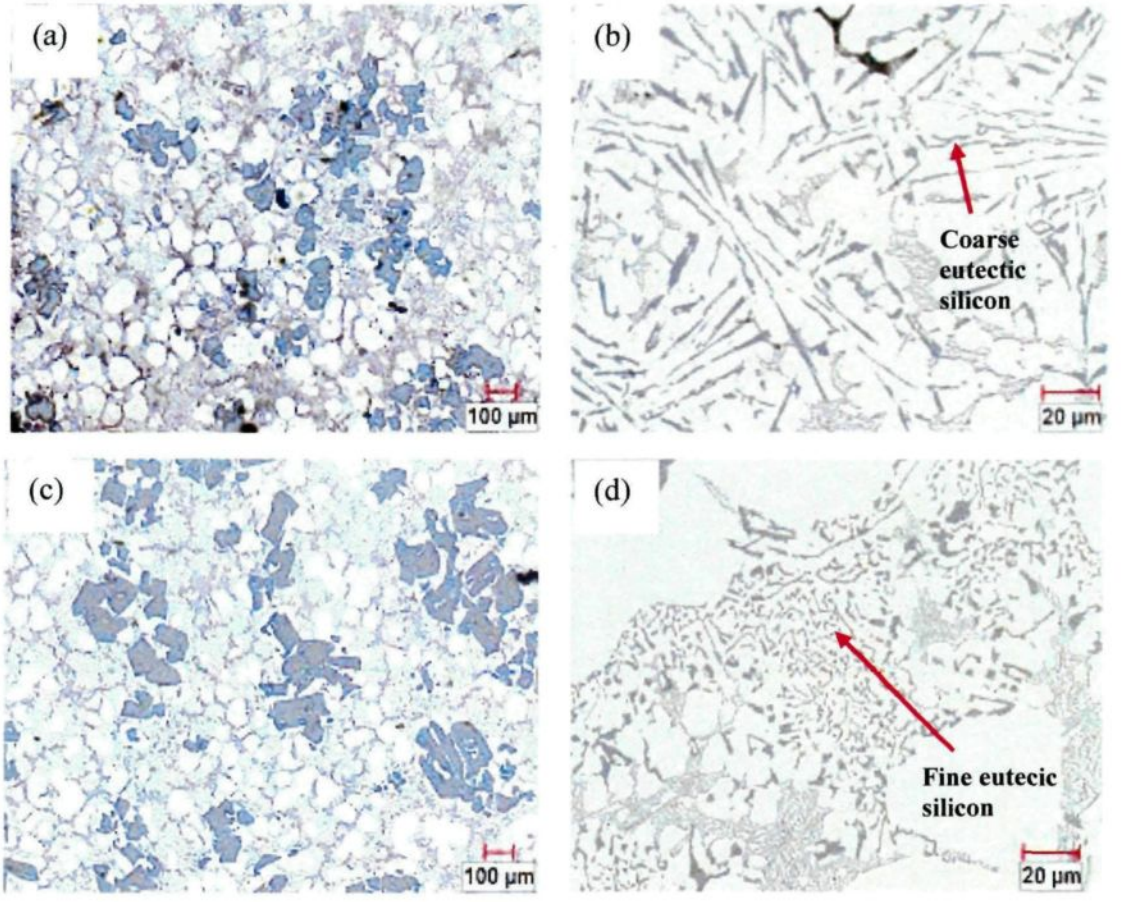

Fig. 4.5 Microstructure of semi-solid A390 with addition of (a)50 g of A390 alloy + 42 g of A356 alloy of solid metal, (b) with 88ppm P + 0ppm Sr and (c) and (d) with 88ppm P + 200ppm Sr.

The evolution of the effective volume fraction of α-Al resulting from the addition of solid alloys is illustrated in Figure 4.6. It clearly shows that the effective volume fraction of α-Al particles in final semi-solid slurries increases with an increase of the amount of solid alloy added as well as with the alloy composition. Figure 4.7 shows the effect of phosphorus and strontium addition on the particle surface area of primary silicon and of α-Al. It can be seen that the size of primary silicon particle decreases with addition of 88ppm P. The combination of phosphorus and strontium addition produces primary silicon

particles that are only partially refined and remain in a size that is larger than that obtained by phosphorus refinement. It can be seen that, in all three cases, the size of α-Al particles remains almost unchanged.

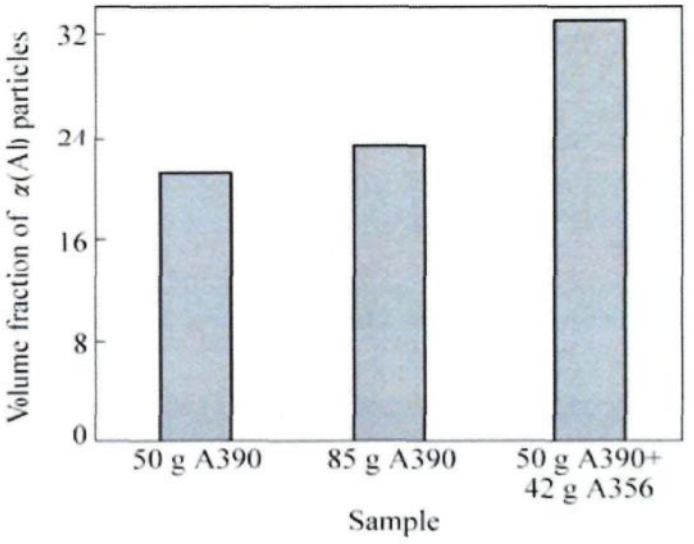

Fig. 4.6 Effect of mass and composition of solid alloy on volume fraction of α(Al) particles.

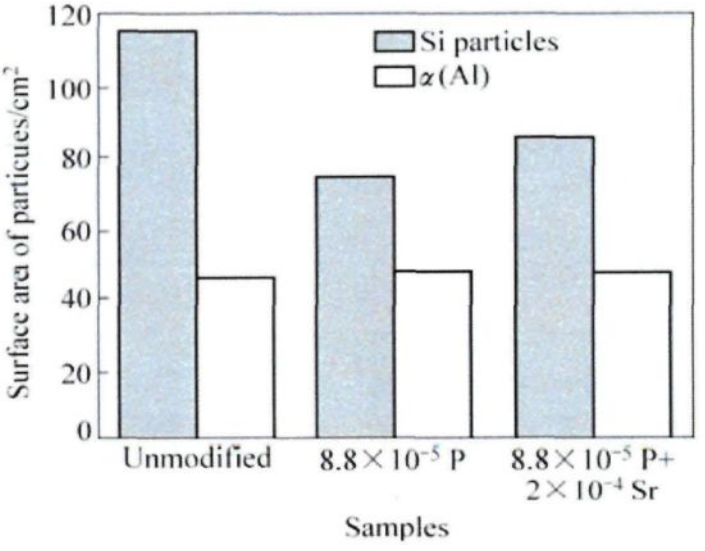

Fig. 4.7 Effect of solid alloy (50 g A390+42 g A356) with P and Sr addition on particle surface area of primary silicon and α(Al).

4.4 Summary

1. A combination of the SEED process, isothermal holding using insulation and addition of solid alloy during swirling can be used to rheoprocess semi-solid A390 alloy.

2. Isothermal holding using insulation reduces heat loss at the mould wall while the addition of solid alloy during swirling allows high extraction of latent heat at the center of the slurry, resulting in a decrease of the temperature gradient within the slurry and an increase of α-Al volume fraction.

3. The addition of two different compositions of solid alloy (A390 and A356) significantly increases the volume fraction of non-dendritic α-Al particles, which greatly improves the processability and rheological properties of semi-solid A390 slurries.

4. Primary silicon in the semi-solid microstructure can be refined by phosphorus additions. However, refinement of primary silicon and modification of eutectic silicon cannot be achieved simultaneously by phosphorus and strontium additions.

References

[1] L. Lasa, J. M. Rodriguez-Ibabe. Materials science and Engineering, 2003, A363: 193-202.
[2] G. Timmermans, L. Froyen. Wear, 1999, 230: 105-117.
[3] H. J. Kim. Materials Science and Technology, 2003, 19: 915-918.
[4] D. Saha, D. Apelian, R. DadGupta. AFS Transaction, 2004, 112: 04-57.
[5] Z. Fan. International Materials Reviews, 2002, 47: 49-84.
[6] C. M. Chen, C. C. Yang, C. G. Chao. Journal of Materials Processing Technology, 2005, 167: 103-109.
[7] P. Kapranos, D. H. Kirkwood, H. V. Atkinson, J. T. Rheinlander, J. J. Bentzen, P. T. Toft, C. P. Debel, G. Laslaz, L. Maenner, S. Blais, J. M. Rodriguez-Ibabe, L. Lasa, P. Giordano, G. Chiarmetta, A. Giese. Journal of Materials Processing Technology, 2003, 135: 271-277.
[8] Birol Yucel. Journal of Materials Processing Technology, 2008, 207: 200-203.
[9] H. Wang, Z. L. Ning, C. J. Davidson, D. H. Stjohn, S. S. Xie. Thixotropic structure formation in A390 hypereutectic Al-Si alloy. 8th International conference of semi solid processing, Limassol, Cyprus, 2004, 553-561.
[10] Haga Toshio, P. Kapranos. Journal of Materials Processing Technology, 2002, 130-131: 594-598.
[11] Birol Yucel. Journal of alloys and compounds, 2009, 480: 365-368.
[12] J. Jorstad, D. Apelian. International Journal of Metalcasting, summer, 2009: 13-36.
[13] D. Doutre, G. Hay, P. Wales, J-P. Gabathuler. SEED: Anew process for semi-solid forming. The conference of metallurgists COM, Vancouver, British Columbia, Canada, 2004, 43: 265-272.
[14] C. R. Ho and B. Cantor. Acta Metallurgica et Materialia, 1995, 43: 3231-3246.
[15] Y. H. Cho, H. C. Lee, K. H. Oh, and A. K. Dahle. Metallurgical and Materials Transactions A, 2009, 39: 2435-2448.

CHAPTER 5

SOLIDIFICATION AND MICROSTRUCTURE EVOLUTION OF HYPEREUTECTIC AL-15SI-XMG-4CU ALLOYS WITH HIGH MG CONTENTS

CHAPTER 5

SOLIDIFICATION AND MICROSTRUCTURE EVOLUTION OF HYPEREUTECTIC AL-15SI-XMG-4CU ALLOYS WITH HIGH MG CONTENTS

5.1 Introduction

Hypereutectic Al-Si alloys are widely used in automotive and aerospace applications due to their low coefficient of thermal expansion, good wear resistance and high hardness [1, 2, 3]. Alloys such as A390, containing 17% Si, 4.5% Cu and 0.5%Mg, are widely used in the manufacture of pistons, cylinder blocks and AC compressors [3]. All alloy composition are given in weight percent (wt %) unless otherwise stated. The presence of primary silicon in the matrix provides good wear resistance and high hardness. In this respect, hypereutectic Al-Si alloys have often been considered as *in situ* metals matrix composites (MMCs), with the primary Si acting as the reinforcement [4]. However, the size and the morphology of the Si phase can affect the mechanical properties of the alloy. The addition of a refiner and optimization of the cooling rate have been proposed to reduce the size of silicon particles and thus improve the mechanical properties of these alloys [5].

Backerud *et al.* [6] studied the solidification of A390 alloy. The solidification reactions reported by them are listed in Table 1. Solidification begins with the precipitation of primary silicon. The second phase precipitated is a small volume fraction of dendritic aluminum phase, followed by the eutectic reaction wherein Al, Si and β-Al_5FeSi phases are

formed. Precipitation of Mg_2Si and θ-Al_2Cu phases takes place in later reactions, as shown in Table 5.1.

Table 5.1 Solidification reactions for A390 alloy [6]

N°	Reactions	Suggested temperature °C (K)
1	Precipitation of primary Si crystal	654 (927)
2	Development of α-Al dendrites	628 (901)
3	Start of eutectic reaction Liq.→ α-Al+Si+Al_5FeSi	565 (838)
4	Precipitation of Mg_2Si Liq.→ α-Al+Si+ Mg_2Si	540 (813)
5	Precipitation of Al_2Cu L+ Mg_2Si → α-Al+Si+ Al_2Cu+$Al_5Mg_8Cu_2Si_6$	500 (773)
6	Precipitation of complexe eutectic Liq.→ α-Al+Si+ Al_2Cu+ $Al_5Mg_8Cu_2Si_6$	499 (772)
7	End of solidification	494 (768)

Hekmat-Ardakan *et al.* [7, 8] and Mandal *et al.* [9] observed that Mg addition changed the morphology and size of the primary silicon and eutectic phase in hypereutectic A390 alloy, and led to the formation of both eutectic and primary Mg_2Si phase particles. Although the tensile strength of these alloys was superior to that of A390 alloy, they exhibited a lower hardness. Zeng *et al.* [10] examined the effects of both Si and Mg content in Al-Si-Mg alloys, for Si and Mg levels ranging from 8 to 17% and from 2 to 4%, respectively. The addition of 2-4% Mg changed the brittle β-Al_5FeSi phase to the π-$Al_8Si_6Mg_3Fe$ phase, and improved the castability and mechanical properties at high Mg content.

More recently, Hekmat-Ardakan *et al.* [8] reported that higher Mg contents change the morphology of the eutectic silicon from their long platelet-like form to a fine Chinese script form while the primary silicon particles are suppressed and are replaced by primary Mg_2Si

phase. They also examined the wear properties of hypereutectic Al-Si-Mg-Cu alloys containing 6 and 10% Mg in the as-cast condition and after T6 heat treatment compared to those of A390 alloy [4]. It was found that the wear resistance increases considerably for alloys with high Mg content. From their investigations, the authors concluded that the improvement in wear resistance may be attributed to the transformation of the coarse primary Si particles to finer Mg_2Si phase particles.

Zhang *et al.* [11] have reported that Mg_2Si has a density of 1.99 x $10^3 kgm^{-3}$, a low thermal expansion coefficient of 7.5 x $10^{-6}K^{-1}$, a high melting temperature of 1085°C, a high hardness of 4.5 x $10^9 Nm^{-2}$ and a reasonably high elastic modulus of 120 GPa. These properties are important characteristics for the development of new lightweight and wear-resistant alloys containing Al and Mg_2Si designed to replace the traditional Al-Si hypereutectic alloys currently used in industry [12]. Table 5.2 shows the close similarity in properties between Mg_2Si and Si particles.

Table 5.2 Physical and mechanical properties of Mg_2Si and Si [11].

Phases	Crystal structure	Lattice parameter (nm)	Density ($g\ cm^{-3}$)	C.T.E ($10^{-6}\ K^{-1}$)	Elastic modulus (GPa)	Melting point (°C)
Mg_2Si	Cubic	0.635	1.99	7.5	120	1085
Si	Cubic	0.542	2.33	3.06	112	1411

According to Hekmat-Ardakan *et al.* [7], the phase diagram calculations for Al-17%Si alloy with a minimum Mg content of 11% show that the microstructure contains only primary Mg_2Si particles dispersed in the eutectic matrix, whereas below this level, a mixture of Mg_2Si and Si particles are observed. The lower density of Mg_2Si (*cf.* 1.99 with 2.33 g/cm^3 for Si) provides an excellent opportunity for further weight reduction without

loss in wear resistance. In view of these advantages, hypereutectic Al-Si alloys with high Mg contents can also be considered as *in-situ* aluminum matrix composites containing a large amount of Mg_2Si particles, and have garnered much interest in recent years to be potential candidates for critical applications such as engine blocks and brake discs.

While several studies [13, 14, 15] have reported on the methods of modifying the Mg_2Si primary phase in the Al/Mg_2Si *in-situ* composite, however, information on the solidification process of such composites produced by alloying hypereutectic Al-Si with Mg is limited. Zhang *et al.* [16] stated that microstructural changes in the Al/Mg_2Si composite system were not explained clearly in previous investigations due to the very limited information on the Al-Mg-Si ternary phase diagram, especially for high Mg and Si contents.

Hekmat-Ardakan *et al.* [17] carried out a thermodynamic investigation of hypereutectic Al-Si A390 alloys with up to 10% Mg using the FactSage software developed by the CRCT group at their institution. The authors reported that the addition of Mg up to 10% alters the formation temperature for the liquidus, and the start of the binary and ternary eutectic reactions. The Mg_2Si phase precipitates as an intermetallic compound for contents up to 4.2%, and between 4.2 and 7.2% Mg. However, for compositions above 7.2% Mg, the Mg_2Si solidifies as the primary phase instead of Si.

In the interests of pursuing the development of new wear-resistant alloys further, and given the limited information available to date, the present study was undertaken to investigate the solidification behaviour of Al-Si-Mg-Cu quaternary alloys with Mg concentrations extending up to 15%, beyond that investigated previously. The

microstructures of these alloys were characterized using optical microscopy and scanning electron microscopy (SEM), and image analysis for quantification purposes. ThermoCalc calculations were also carried out to determine the sequence of reactions and the phases occurring during the solidification process.

5.2 Materials and Methods

In this chapter, ThermoCalc was used to investigate the effect of high Mg contents on the solidification sequence and microstructure of the hypereutectic Al-Si-Mg-Cu system.

A commercial 390 alloy, and Al-50%Si and Al-50%Cu master alloys were used as starting materials to prepare the Al-15Si-xMg-4Cu alloys. The chemical composition of the alloys used in this part is presented in Table 5.3. DTA measurements were also carried out for alloys with 6.2, 8.4, 12.8 and 14.9 % Mg at cooling rate of 0.6 $^{o}C.s^{-1}$.

Sample for metallographic analysis were obtained from thermal analysis cups. Microstructural examination of polished and deep etched samples was conducted by optical microscopy and the various phases observed were identified using scanning electron microscopy. Image analysis was also used to quantify the volume fractions of Mg_2Si and Si phases. The details of the experimental method can be found in the section II- part 1 of Chapter 3.

Table 5.3 Alloy Codes and Compositions (wt. %)

Alloy #	Elements (wt. %)				
	Si	Mg	Cu	Fe	Al
A	15.1	6.2	4.0	0.4	Bal.
B	15.5	8.4	4.0	0.4	Bal.
C	15.4	12.8	4.2	0.3	Bal.
D	15.5	14.9	4.0	0.3	Bal.

5.3 Results and Discussion

5.3.1 Thermodynamic predictions

The effect of Mg content on phase transformation and microstructure evolution during solidification of the hypereutectic Al-Si-Mg-Cu quaternary alloy system was investigated by changing the Mg level from 6.15% to 20%, and keeping the Si and Cu constant at 15% and 4%, respectively. The phase diagram was calculated using ThermoCalc software and the supporting AA12Br data bank. Figure 5.1 summarizes the various phase transformation reactions that occur in the hypereutectic Al-Si-Mg-Cu alloys during solidification over the range of Mg concentrations studied. It should be mentioned here that although the ThermoCalc data bank also has values for the addition of iron to the system, the resulting phase diagram obtained becomes quite complicated with the inclusion of Fe. Thus, in the interests of simplicity, only the quaternary Al-Si-Mg-Cu system was considered in the thermodynamic calculations. However, while the amount of Fe in the alloy is only about 0.3-0.40%, it is sufficient to account for the formation of the π-$Al_8Mg_5FeSi_6$ phase which was observed in this study.

For the range of Mg concentrations studied, the phase diagram showed two distinct regions, I and II, separated by a critical composition at 12.52% Mg, region I representing Mg levels of 5.16 to 12.52%, and region II those from 12.52 to 20% Mg, corresponding to the vertical dotted lines in Figure 5.1. It was also found that within this range of Mg concentration, the solidification sequence changed significantly. Based upon Fig. 5.1, the sequence of reactions and phases formed upon solidification under equilibrium conditions is presented in Table 5.4.

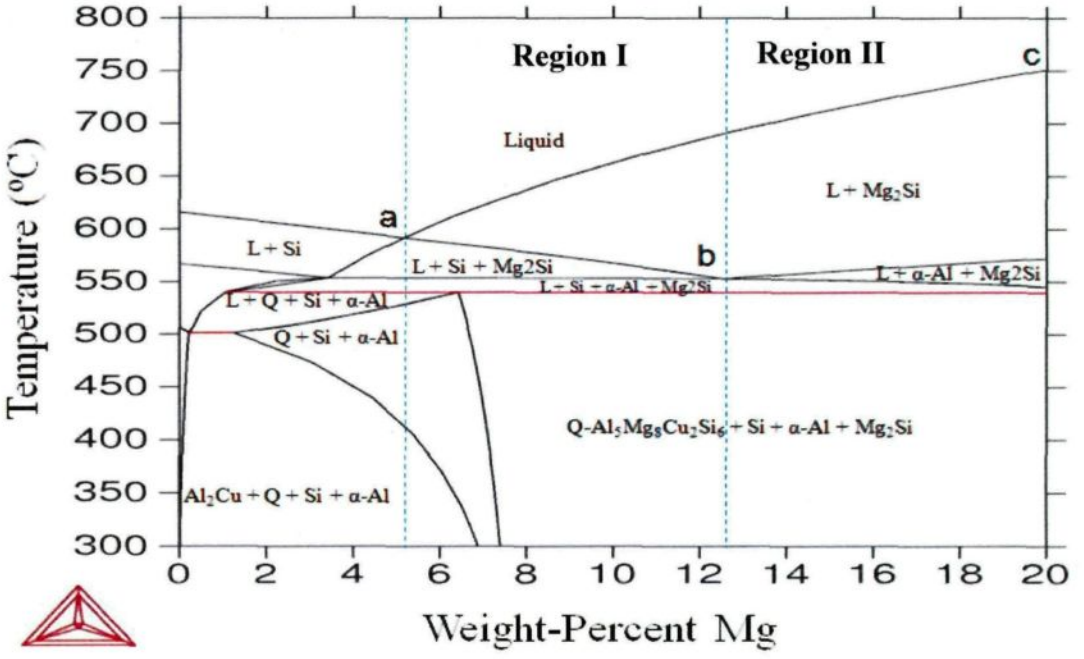

Fig. 5.1 Calculated phase diagram of Al-Si-Cu-Mg system. The dashed lines represent respectively the critical compositions of Al-15Si-4Cu-xMg at 5.16% Mg and 12.5% Mg.

According to Fig. 5.1, the liquidus, binary reaction, and ternary eutectic temperatures are found to vary significantly with Mg addition. The liquidus temperature increases progressively from 591.4°C at 5.2% Mg, to 690°C at 12.52% Mg, to 751 °C at 20% Mg; whereas the binary reaction temperature initially decreases from 591.4°C at 5.2% Mg to 553°C at 12.52% Mg, and then increases to 572.5°C at 20% Mg. The quaternary reaction, however, is not affected by the variation in Mg content. The phase diagram shows clearly that Mg_2Si precipitates as the primary phase, and then either Si and Mg_2Si, or α-Al and Mg_2Si, co-precipitate from the melt, depending on the Mg level in the alloy.

Table 5.4 Reaction scheme for Al-Si-Mg-Cu system according to the present work.

	Region I (a-b)	The eutectic composition (b)	Region II (b-c)	Solidification stage	Reaction No.
Solidification path	Type I	Type II	Type III		
	$L \rightarrow L + Mg_2Si$	$L \rightarrow L + Mg_2Si$	$L \rightarrow L + Mg_2Si$	Primary Mg_2Si	1
	$L \rightarrow L + Si + Mg_2Si$		$L \rightarrow L + \alpha\text{-}Al + Mg_2Si$	Pre-eutectic	2 - 3
	$L \rightarrow L + Si + \alpha\text{-}Al + Mg_2Si$			Main eutectic	4
	$L \rightarrow Q\text{-}Al_5Mg_8Cu_2Si_6 + Si + \alpha\text{-}Al + Mg_2Si$			Post- eutectic	5
	$\theta\text{-}Al_2Cu + Q\text{-}Al_5Mg_8Cu_2Si_6 + Si + \alpha\text{-}Al + Mg_2Si$ *				6

* The reaction 6 was predicted in the phase diagram only for Mg compositions up to 7 wt%.

The liquid and solid phase fractions of each constituent obtained under equilibrium conditions for the four alloys studied (i.e. four Mg levels) are shown in Figures 5.2(a) through (d). The solidification paths of these alloys can be classified into three representative types:

(i) Type I starts with the precipitation of primary Mg_2Si particles, followed by a secondary reaction where Mg_2Si co-precipitates with the Si phase, then the main eutectic reaction $L \rightarrow L+Si+\alpha\text{-}Al+Mg_2Si$ occurs, which produces a high amount of α-Al. This is followed by the post-eutectic reaction $L \rightarrow Q+Si+\alpha\text{-}Al+Mg_2Si$, as shown in Figures 5.2(a) and 5.2(b). These two diagrams show clearly how the phase fractions of the primary Mg_2Si and Si particles vary with Mg content. Upon increasing the Mg concentration, the Mg_2Si phase fraction increases linearly while the Si phase fraction decreases considerably.

(ii) Type II also begins with the precipitation of the Mg_2Si primary phase, followed by the main eutectic reaction $L \rightarrow L+Si+\alpha\text{-}Al+ Mg_2Si$, and finally by the post-eutectic $L \rightarrow Q+Si+\alpha\text{-}Al+Mg_2Si$ reaction, as shown in Figure 5.2(c). A significant increase in the Mg_2Si phase fraction can be observed compared to alloys A and B. On the other hand, the second or pre-eutectic reaction ($L \rightarrow Mg_2Si + Si$ or $L \rightarrow L + \alpha\text{-}Al + Mg_2Si$) which occurred in alloys A and B is found to be completely absent in the case of alloy C, as shown in Figure 5.2(c).

(iii) Type III is quite similar to the Type I solidification path corresponding to alloys A and B. The only difference lies in the second reaction where the pre-eutectic reaction forming Mg_2Si and Si is replaced by one forming Mg_2Si and α-Al in alloy D, as shown in Figure 5.2(d).

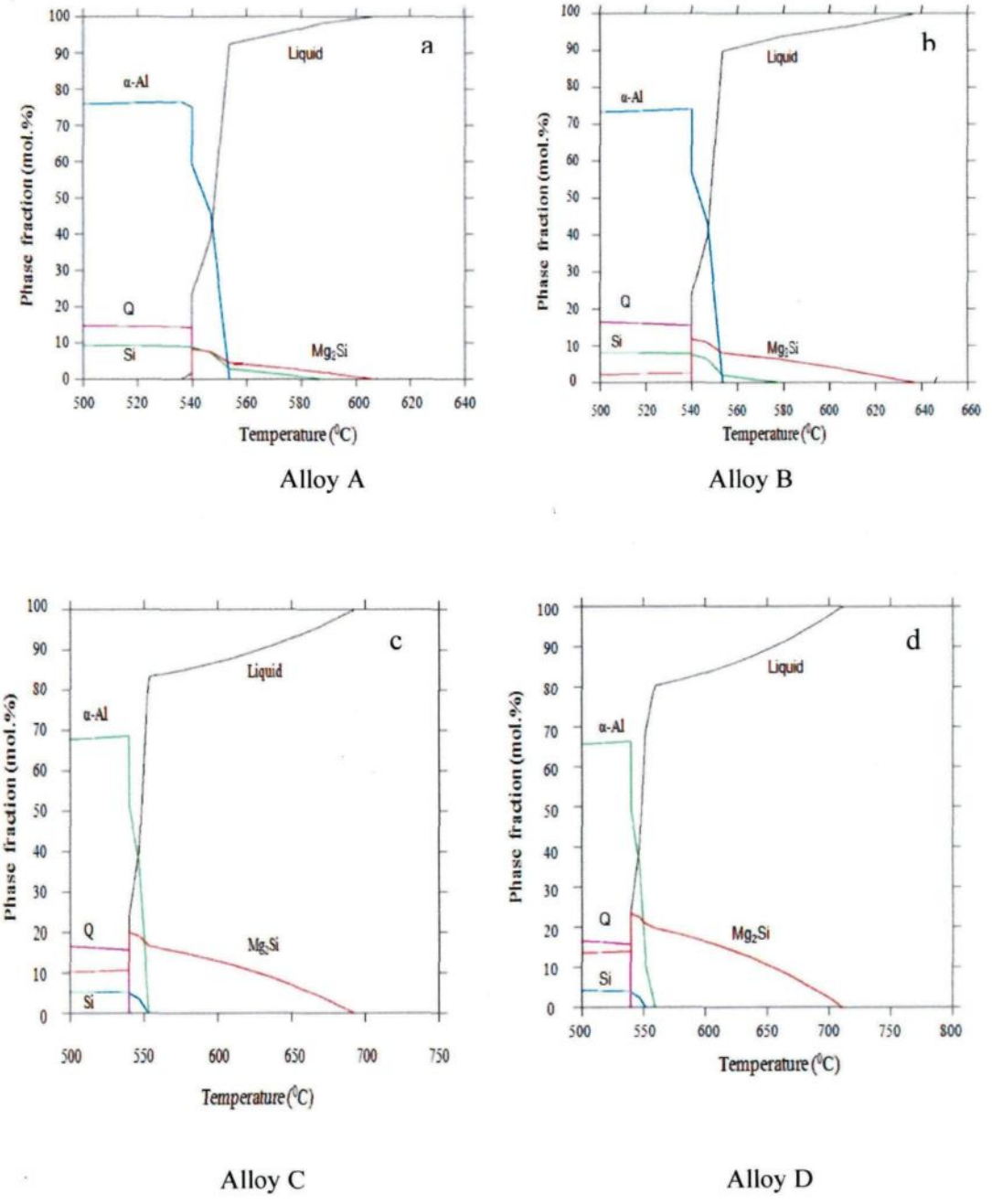

Fig. 5.2 Calculated phase fractions for the four alloys studied, showing the amounts of the phases present under equilibrium conditions, as a function of temperature.

Table 5.5 lists the calculated liquid fractions, type/percentage of constituents formed at the transition temperatures, as well as the solid fractions corresponding to each reaction during the solidification of the four alloys. The results indicate that the solid fraction at the eutectic reaction increases continually as the Mg content rises from 7.7% to 31.2% on going from alloy A to alloy D, as does the Q phase fraction, which increases from 14.8% to 15.76%; whereas those of primary Si and α-Al phases decrease respectively from 37.01% in alloy A to 7.61% in alloy B with Mg addition.

Table 5 The liquid and solid fractions corresponding to the reactions occurring in the four alloys studied.

Alloy code	Reaction #*	Reaction	Temp. (°C)	Liquid fraction (%)	Constituent percentage (at %)				Solid fraction (%)
					Mg_2Si	Si	α-Al	Q	
A	1	Primary Mg_2Si	609	100	-	-	-	-	0
	2	Pre-eutectic	587	97.8	100	-	-	-	2.2
	4	Eutectic	554	92.3	62.98	37.01	-	-	7.7
	5	Post-eutectic	539	2.3	-	8.94	76.2	14.86	97.65
B	1	Primary Mg_2Si	643	100	-	-	-	-	0
	2	Pre-eutectic	576	92.7	100	-	-	-	7.21
	4	Eutectic	554	89.2	83.01	16.98	-	-	10.73
	5	Post-eutectic	539	23.7	3.3	7.61	73.61	15.47	76.3
C	1	Primary Mg_2Si	693	100	-	-	-	-	0
	4	Eutectic	553	83.4	100	-	-	-	17.6
	5	Post-eutectic	539	23.9	10.06	4.15	69.03	15.75	76.1
D	1	Primary Mg_2Si	711	100	-	-	-	-	0
	3	Pre-eutectic	559	80.3	100	-	-	-	19.7
	4	Eutectic	552	68.8	66.24	-	33.75	-	31.2
	5	Post-eutectic	539	24	13.99	3.95	66.3	15.76	76

* Reactions: (1) $L \rightarrow L + Mg_2Si$; (2) $L \rightarrow L + Si + Mg_2Si$; (3) $L \rightarrow L + \alpha\text{-}Al + Mg_2Si$; (4) $L \rightarrow L + Si + \alpha\text{-}Al + Mg_2Si$; (5) $L \rightarrow Q\text{-}Al_5Mg_8Cu_2Si_6 + Si + \alpha\text{-}Al + Mg_2Si$

5.3.2 Microstructure observations

5.3.2.1 Precipitation of primary phases

Figures 5.3(a) through (d) display optical micrographs of samples corresponding to alloys A through D with 6.15, 8.42, 12.82, and 14.86% Mg, respectively. The microstructural analysis was supported by quantitative image analysis measurements of area fractions and the average size of the black Mg_2Si and grey Si primary phase particles

observed in these samples. All four alloys exhibit primary Mg_2Si and Si particles, a ternary eutectic region of Si/α-Al/ Mg_2Si and intermetallic compounds.

The microstructure of alloy A in Fig. 5.3(a) shows fine and uniformly distributed primary Mg_2Si particles co-existing with small polyhedral Si particles. Increasing the Mg content increases the size of the primary Mg_2Si and Si particles, Fig. 5.3(b). With further increase in Mg addition up to 12.82%, the primary Si particles disappear and are replaced by α-Al dendrites, as shown in Fig. 5.3(c). Nami *et al.* [19] reported that the formation of the α-Al phase on Mg_2Si particles is due to the non-equilibrium solidification of the alloy, caused by the limited diffusion rate of Mg and Si in the liquid surrounding the Mg_2Si particles.

Of particular interest to note is that (i) the morphology of the primary Mg_2Si particles changes from polyhedral form to a coarse dendrite crystal shape, and (ii) their size increases dramatically when compared with the particles observed in alloys A and B, as shown in Fig. 5.3(c). At the highest Mg content of 14.86% (Alloy D), no further change in the morphology of the Mg_2Si phase is observed, however the Mg_2Si dendrites coarsen considerably, while the primary Si particles disappear, being replaced by the α-Al phase, as shown in Fig. 5.3(d).

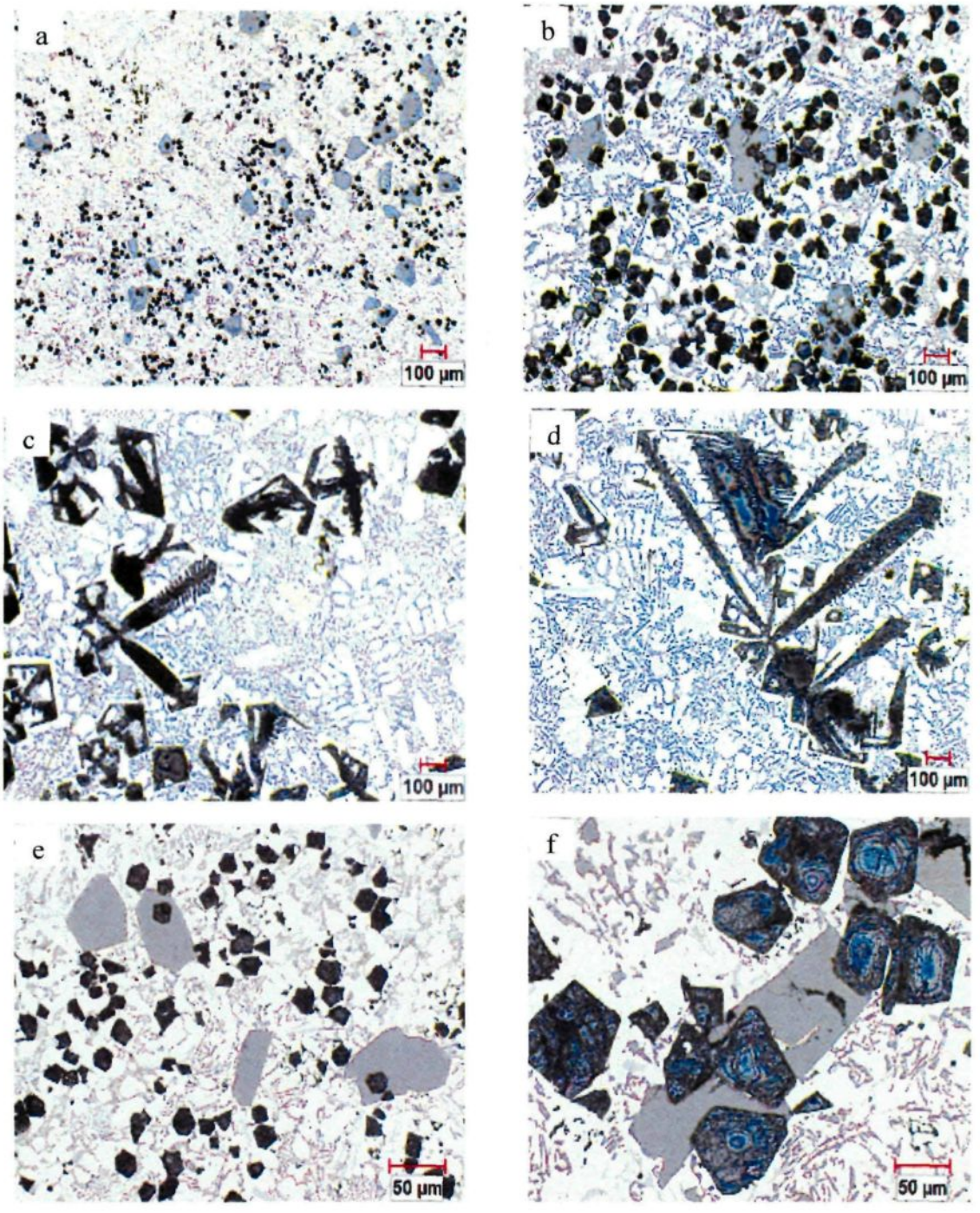

Fig. 5.3 Optical micrographs showing the typical structures obtained in the four alloys studied, containing (a) 6.15%, (b) 8.42%, (c) 12.82%, and (d) 14.86% Mg; (e, f) High magnification micrographs of (e) Alloy A, and (f) Alloy B. Note the change in size, morphology, and area fraction of the primary Mg_2Si (black) and Si (grey) particles.

Figures 5.3(e) and (f) are micrographs of Alloys A and B, respectively, taken at a higher magnification so as to render the primary particles as well as the eutectic regions much more clearly than the structures displayed in Figures 5.3(a) and (b) for the same alloys. The eutectic phases will be discussed in detail in section 5.3.2.3.

In order to better delineate the 3D morphology of the primary Mg_2Si and Si particles, the samples were deep-etched using a solution of 10% NaOH. Examples for Alloy A and Alloy C are shown in the SEM micrographs of Figures 5.4(a) and 5.4(b), which clearly reveal how the relatively small, faceted polyhedral primary Mg_2Si particles in Alloy A acquire a massive dendrite form in Alloy C when the Mg level is increased from 5.16 to 12.82%. This indicates that high Mg levels significantly influence both the nucleation and growth process of Mg_2Si.

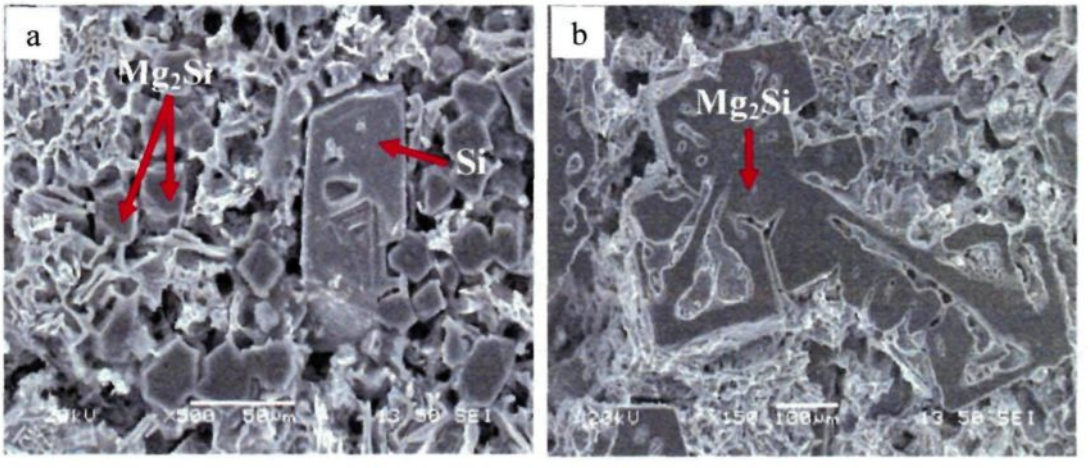

Fig.5.4 SEM micrographs of deeply etched primary Mg_2Si and Si particles in (a) Alloy A, and (b) Alloy C.

5.3.2.2 Growth of primary Mg_2Si phase

The high magnification SEM images of Figure 5.5 show three-dimensional views of particles of primary Mg_2Si phase and its morphological evolution on proceeding from

Alloy A to Alloy D, i.e., with increasing Mg content. At 12.82% Mg, the polyhedral morphology is converted to a dendrite-like form, as exhibited by Alloy C. Further Mg addition only serves to expand these dendrites in all directions. It ought to be noted here that these images were not all taken at the same magnification, the objective being to demonstrate the morphological details as clearly as possible, without cutting off any part of the particle (or particles) shown in the image. This point should thus be kept in mind when comparing the size of the primary Mg_2Si particles, particularly when comparing Figures 5.5(a) and (b), or Figures 5.5(c) and (d).

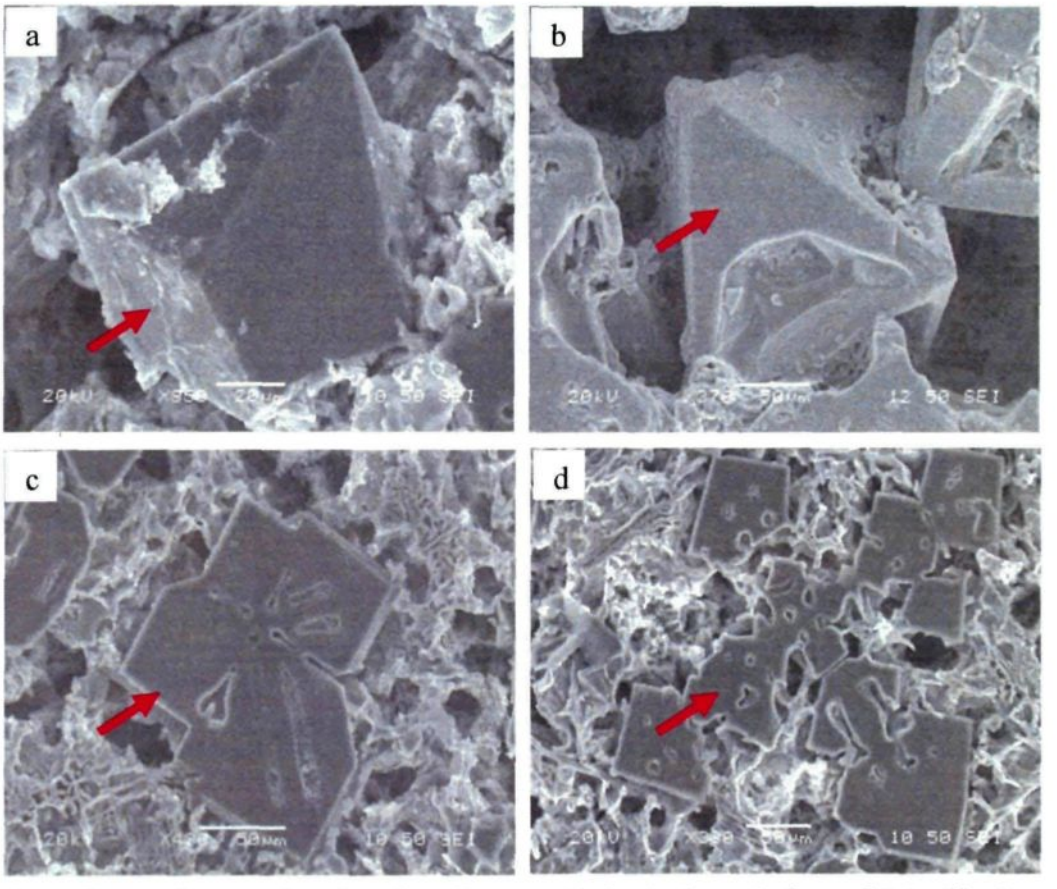

Fig. 5.5 SEM micrographs showing the morphological evolution of Mg_2Si phase with increase in Mg addition: (a) Alloy A, (b) Alloy B, (c) Alloy C, and (d) Alloy D.

Li *et al.* [20] carried out a detailed study of the morphology and growth mechanism of primary Mg_2Si phase in Al-Mg_2Si composite alloys. They reported that primary Mg_2Si particles may display different morphologies, among them, octahedral, "hopper-like", cubic, truncated octahedron and massive dendrite forms. Also, as the Mg content is increased, the particle size increases and the morphology changes. The images displayed in Figure 5 show (a) an octahedral Mg_2Si particle, (b) two Mg_2Si particles connected to each other and displaying partially incomplete octahedral surfaces or the so-called "hopper-like" structure, (c) the dendrite form of Mg_2Si, with arms growing out in four directions, and (d) several other Mg_2Si units, growing along the directions of the dendrite arms. In the context of the latter, Fig. 5.4(b) clearly demonstrates the growth of several secondary arms from the central primary Mg_2Si dendrite.

Wang *et al.* [21] have reported that Mg_2Si crystals have an fcc structure, display a faceted growth, with preferred growth directions along <100>; the crystals exhibit a tendency to appear in the form of faceted octahedrons, corresponding to minimum surface free energy conditions [20]. However, depending on the growth conditions and surrounding environment during the actual solidification process, other morphologies may well result. The presence of certain elements, for example, may alter the growth rate along the preferred growth directions, so that certain planes get eliminated with the progress of growth, others take precedence, ultimately altering the morphology of the Mg_2Si crystals. The alloy composition and any melt treatments such as modification or refining which are generally applied to Al-Si based alloys are thus the controlling parameters which will determine the final morphology of the primary phase.

5.3.2.3 Eutectic phases

The micrographs of Figure 5.6 show the eutectic network structures observed in the four alloys studied. The black Chinese script type particles observed most clearly in (a) are the eutectic Mg_2Si phase, the dark grey acicular particles correspond to the eutectic Si phase, and the lighter dendrite shaped areas represent the α-Al phase, respectively. The presence of copper and iron in these alloys also leads to the precipitation of the θ-Al_2Cu and π-$Al_8Mg_5FeSi_6$ (π-Fe) phases, respectively.

Several morphologically distinct intermetallic constituents were identified with the aid of scanning electron microscopy coupled with energy dispersive spectroscopy. These intermetallic species, labelled 2, 3 and 4 in Figure 5.6, were respectively identified as the π-$Al_8Mg_5FeSi_6$, θ-Al_2Cu, and Q-$Al_5Mg_8Cu_2Si_6$ phases. The β-Al_5FeSi phase, which appears in the form of platelets in Al-Si alloys at low Mg contents, is completely suppressed and is replaced by the π-$Al_8Mg_5FeSi_6$ phase. The presence of all these constituents is clearly noted in all four alloys.

A comparison of the eutectic structure in these alloys reveals a significant refinement in the size of the eutectic silicon particles with increasing Mg content. As a comparison of Figures 5.6(a) and 5.6(d) reveals, the morphology of the eutectic Si particles is also changed from its regular plate-like form to very fine script-like or fishbone type structures (see particle #5). The present findings also show that the addition of Mg leads to an abundant formation of the π-Fe intermetallic phase and a consequent increase in the size of these particles with increasing Mg content from 6.15 to 14.86%.

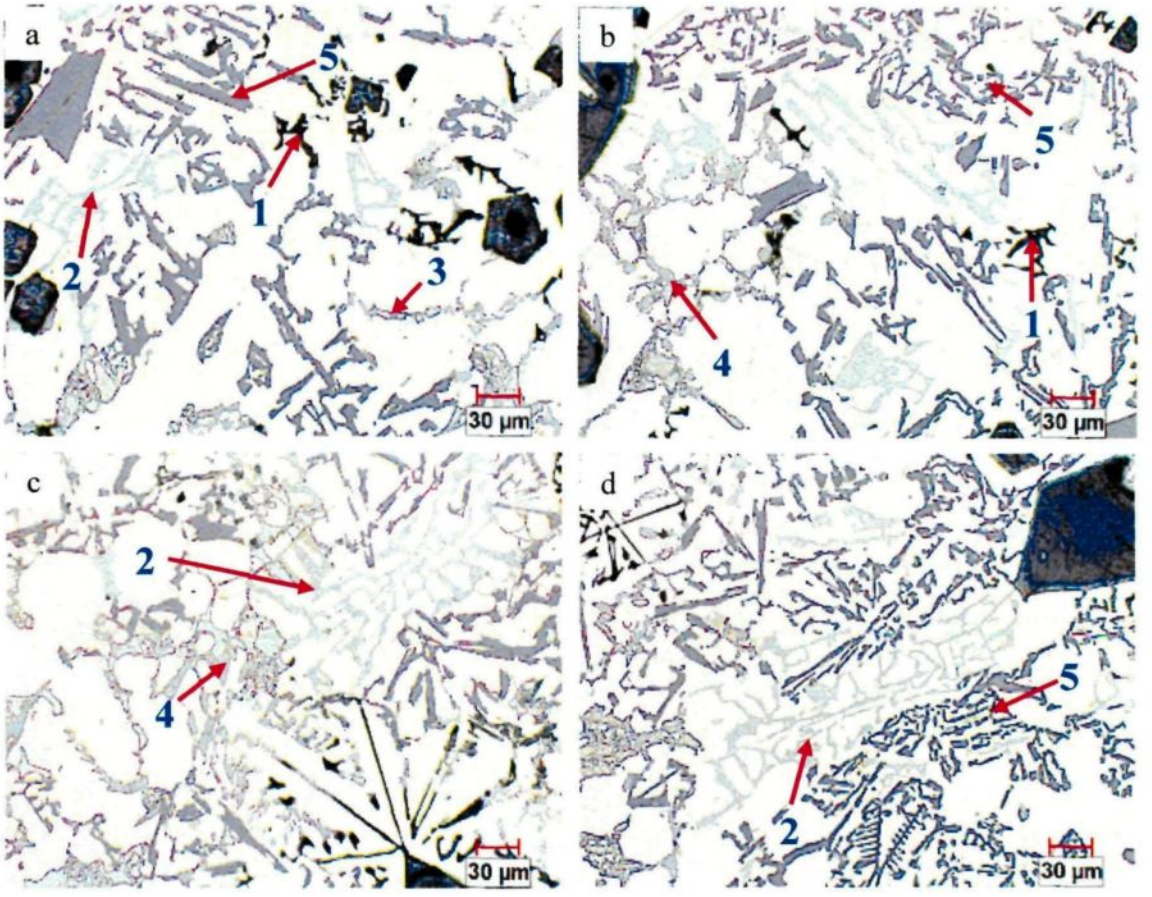

Fig. 5.6 Optical micrographs obtained from the eutectic regions of the four alloys in the as-cast condition: (a) Alloy A, (b) Alloy B, (c) Alloy C, and (d) Alloy D, showing the presence of (1) eutectic Mg_2Si, (2) π-$Al_8Mg_5FeSi_6$, (3) θ-Al_2Cu, (4) Q-$Al_5Mg_8Cu_2Si_6$, and (5) eutectic Si.

5.3.3 Image analysis

A quantitative analysis of the microstructural evolution of these alloys as a function of Mg addition was also attempted using image analysis. Fig. 5.7(a) shows the mean particle size of the primary Mg_2Si and Si phases. It was found that the average Mg_2Si particle size increased from 17.64 µm in Alloy A at 6.15% Mg to 727.66 µm at 14.86% Mg in Alloy D. Also, the average Si particle size increased from 67.87 µm in Alloy A to 429.68 µm in Alloy B. In Alloys C and D no pre-eutectic Si particles were observed, which is in good

agreement with the thermodynamic predictions reported in section 5.3.1. Fig. 5.7(b) compares the predicted (ThermoCalc) and measured fractions of Mg_2Si and Si phases. As may be observed, the Mg_2Si phase fraction increases progressively with increasing Mg content, while the Si phase fraction decreases for the same Mg contents in the case of Alloys A and B. Also, while the calculated and measured phase fractions for Si show good agreement, the measured phase fractions of the primary Mg_2Si phase are larger than the corresponding calculated values. The discrepancy may be explained by the fact that, unlike the Si particles which have a comparatively well defined shape, the Mg_2Si particles are more irregularly shaped, particularly at higher Mg levels, when they change their morphology from polyhedral to dendrite-like (see Fig. 5.3).

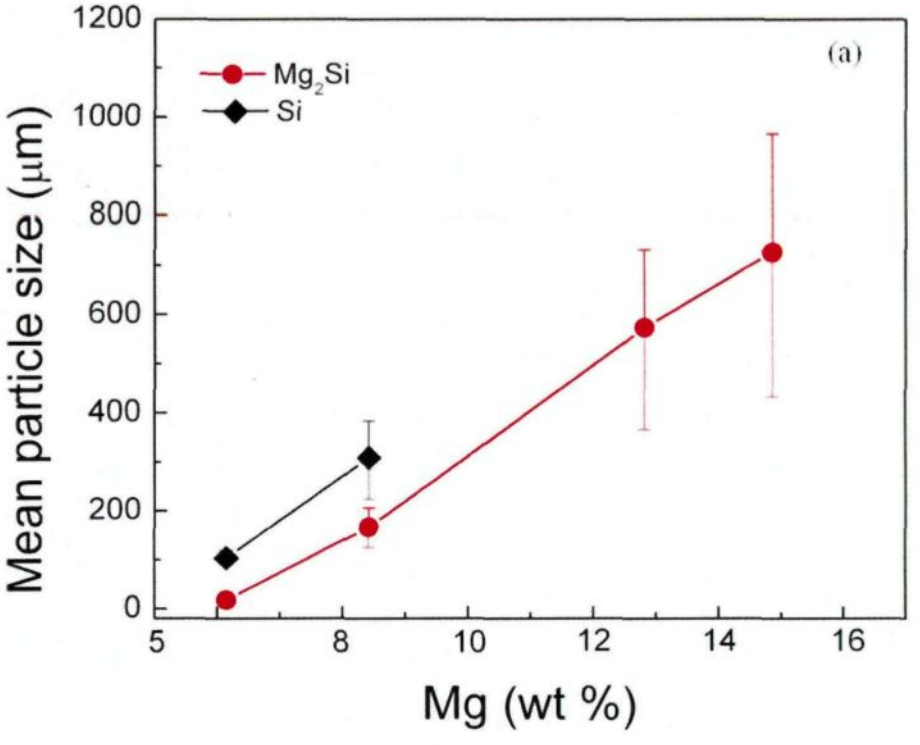

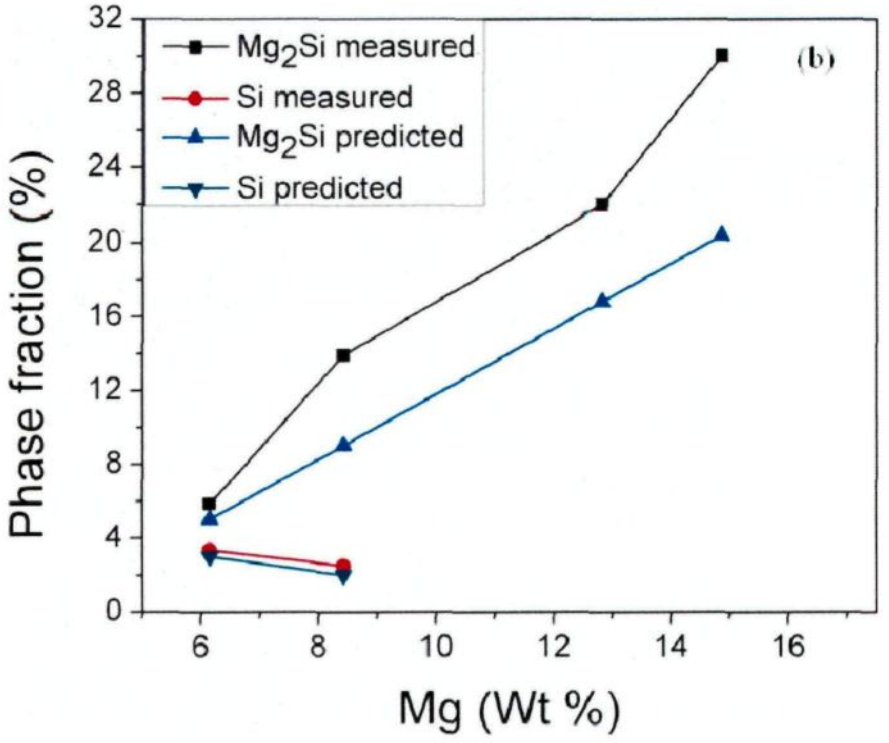

Fig. 5.7 Effect of Mg contents on the (a) mean particle size, (b) phase fraction of hypereutectic Al-Si-Cu-Mg alloys.

In the context of image analysis measurements, where the particles being measured are filled in with a specific color (corresponding to a selected bit plane), it is difficult to accurately outline the contour of such irregularly shaped dendrite particles. Consequently, the area or phase fraction measured would represent more than what is actually present. In addition, the fact that both the primary and eutectic Mg_2Si phases are black, would also contribute to an increase in the measured values since, during measurement, if some eutectic Mg_2Si particles, albeit much smaller in size, were present in the fields examined,

they would also be counted. Overall, the measured and calculated Mg_2Si phase fractions show the same trend. Interestingly enough, the two values are very close in the case of Alloy A with the lowest Mg content, while the values for Alloy D display the largest difference.

5.3.4 Thermal analysis

Thermal analysis was carried out for the four alloys, where the set-up provided a cooling rate of 0.6°C/s. Figure 5.8 shows the cooling curves and the first derivatives obtained in each case. The derivatives clearly reveal 6 peaks in the case of Alloys A and B, but only 4 peaks for Alloy C and 5 peaks for Alloy D, due to the variation in the solidification sequence with the alloy composition. Based on the phase diagram obtained using ThermoCalc and the microstructural observations, the possible reactions corresponding to each individual peak were identified and are listed in Table 5.6 at the end of this section.

For Alloys A and B, Peak 1 corresponds to the formation of primary Mg_2Si particles from the liquid phase. Peak 2 and Peak 3 correspond to the (Mg_2Si and Si) pre-eutectic and the (α-Al, Si and Mg_2Si) ternary eutectic reactions, respectively. Peak 6 represents the precipitation of the Cu-rich intermetallic phase (θ-Al_2Cu). The only contentious identifications are those associated with peaks 4 and 5. In order to investigate the temperatures of formation of the two phases that give rise to peaks 4 and 5 in the cooling curves and derivatives, an interrupted water quenching technique was employed.

Figure 5.9 shows the microstructures of the samples obtained from an Alloy A melt, and quenched (i) from a melt temperature that ranged between 528° and 520°C, and (ii) from 510 °C, respectively. The microstructure of the sample that was water quenched at 510 °C

showed the existence of both Q-$Al_5Mg_8Cu_2Si_6$ and π-$Al_8Mg_5FeSi_6$ phases, as seen in Fig. 5.9(a). However, on examining the microstructure of the samples quenched between 528 °C and 520 °C - one example is shown in Fig. 5.9(b), only the formation of π-$Al_8Mg_5FeSi_6$ was observed. This indicates that the π-iron phase precipitates prior to the Q-$Al_5Mg_8Cu_2Si_6$ phase. Thus, it is reasonable to say that peaks 4 and 5 in Figure 5.8 correspond to the formation of the π-$Al_8Mg_5FeSi_6$ and Q-$Al_5Mg_8Cu_2Si_6$ phases.

Figure 5.10 presents a backscattered electron image obtained from Alloy A, showing a script-like particle within the rectangular area, and the corresponding X-ray mappings of the elemental distributions of Si, Mg, Fe in the area. The morphology, X-ray images, and EDS analysis of the Chinese script particle in the inset in (a) confirmed this to be the π-$Al_8Mg_5FeSi_6$ phase.

The first derivative of the cooling curve shown in Fig. 5.8(c) for Alloy C (12.82% Mg) shows four peaks – Peaks 1, 3, 5 and 6, corresponding to the formation of primary Mg_2Si, the ternary eutectic containing α-Al, Si and Mg_2Si, and the precipitation of the Q-$Al_5Mg_8Cu_2Si_6$ and θ-Al_2Cu phases, respectively. In the case of Alloy D, Fig. 5.8(d), the first two high temperature peaks correspond to the formation of primary Mg_2Si, and the (Mg_2Si + α-Al) pre-eutectic reaction, as predicted by the phase diagram. Peaks 3 and 5 reflect the formation of the (Mg_2Si + Si + α-Al) main eutectic and the Q-phase, while the last peak indicates the precipitation of the θ-Al_2Cu phase. In the case of Alloys C and D, although the reaction for the π-Fe phase is not that evident, nevertheless, the change in the slope of the first derivative curve between Peaks 3 and 5 indicates that the reaction does occur at that point. The fact that the π-Fe phase is observed in the microstructures of all

four alloys, lends credence to the existence of this peak in Figures 5.8(c) and (d). In all probability, the amount of the π-Fe phase produced and the corresponding exothermic energy released is insufficient to produce a more pronounced peak as in the case of Alloys A and B which, incidentally, contain a slightly higher Fe levels (0.4 vs. 0.3% in Alloys C and D). It is interesting to note, at the same time, the increase in peak 5 with increasing Mg content, as more Mg is available to form the Q-phase.

It can be summarized from the above that the major reactions in all the cases can be identified by the phase diagram, and from the microstructure and thermal analysis results. The data obtained from thermal analysis are in good agreement with the calculated phase diagram and the observed microstructures. The only exception is that although the precipitation of θ-Al_2Cu phase at 495°C was not predicted in the phase diagram for alloys C and D, it was observed in both the microstructures and in the cooling curves (Peak 6).

In view of the difficulty in direct visualisation of the θ-Al_2Cu phase in the equilibrium phase diagram for compositions higher than 7 wt% Mg, an alternative calculation was performed using Scheil solidification simulation. This method calculates the solidification path of an alloy under non-equilibrium conditions, which are close to the real solidification conditions, i.e., where there is no diffusion in the solid and thermodynamic equilibrium exists only locally, at the liquid/solid interface [22]. Figure 5.11 shows the calculated Scheil solidification path for Alloys B and D, where the solidification temperature was plotted against a function of the solidified weight fraction. It can be seen that the θ-Al_2Cu phase precipitates in the last reaction, at ~500 °C in both alloys A and D.

Table 5.6 presents a summary of the solidification data. It should be noted that the temperatures obtained from the cooling curves and listed in Table 5.6, are correct to within ±2°C. For comparison purposes, the predicted temperatures (as obtained from ThermoCalc) are also listed in the table in the fourth column.

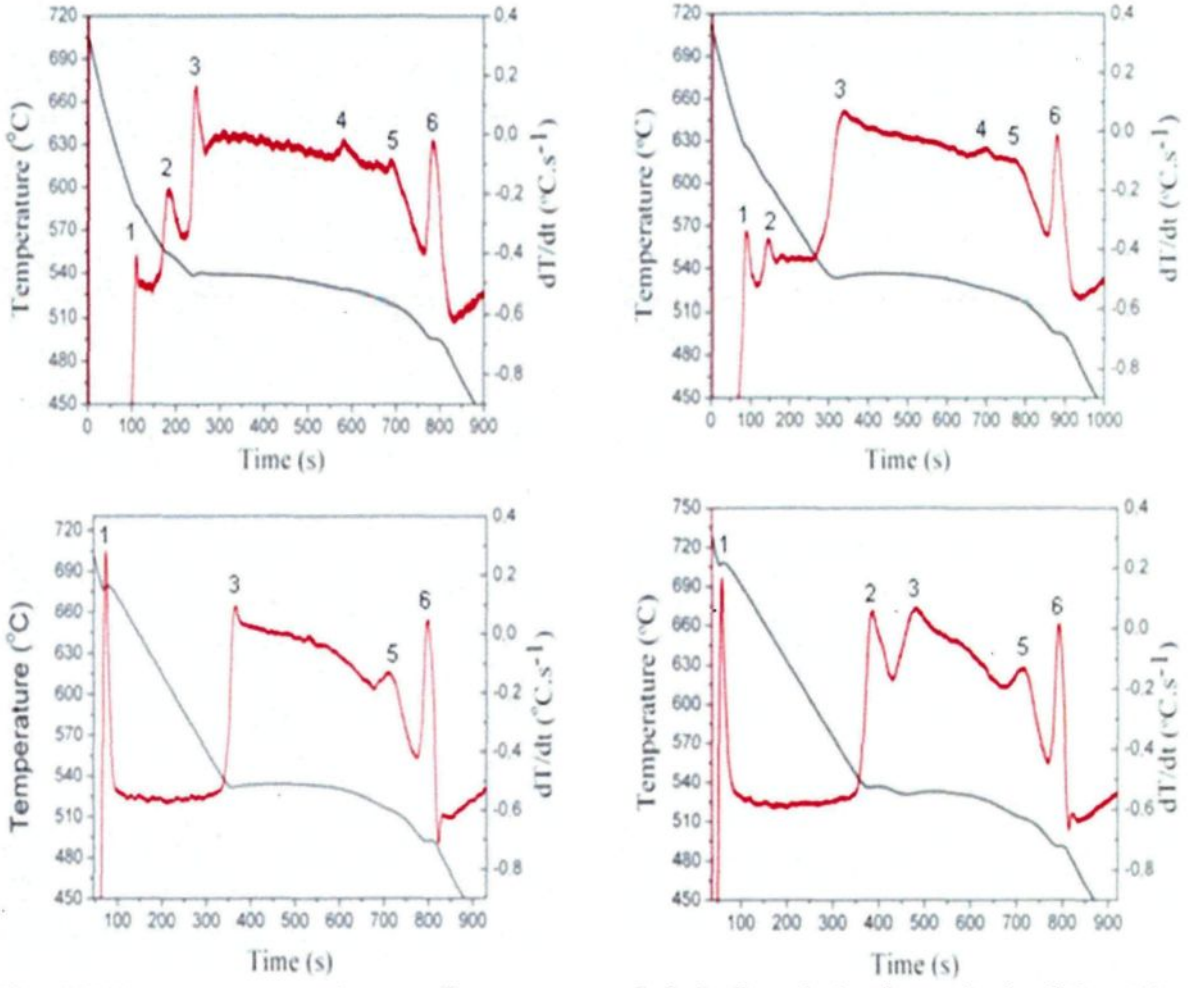

Fig. 5.8 Temperature *vs* time cooling curves and their first derivatives obtained for: (a) Alloy A, (b) Alloy B, (c) Alloy C, and (d) Alloy D.

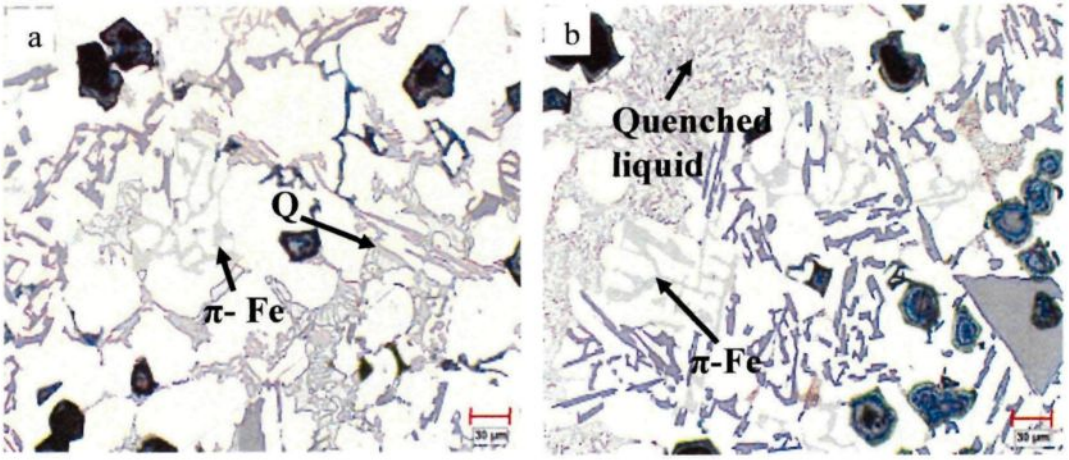

Fig. 5.9 Microstructure of Al-15Si-4Cu-6.15Mg alloy (Alloy A) water quenched at different temperatures (a) at 510 °C, (b) between 528 °C and 520 °C.

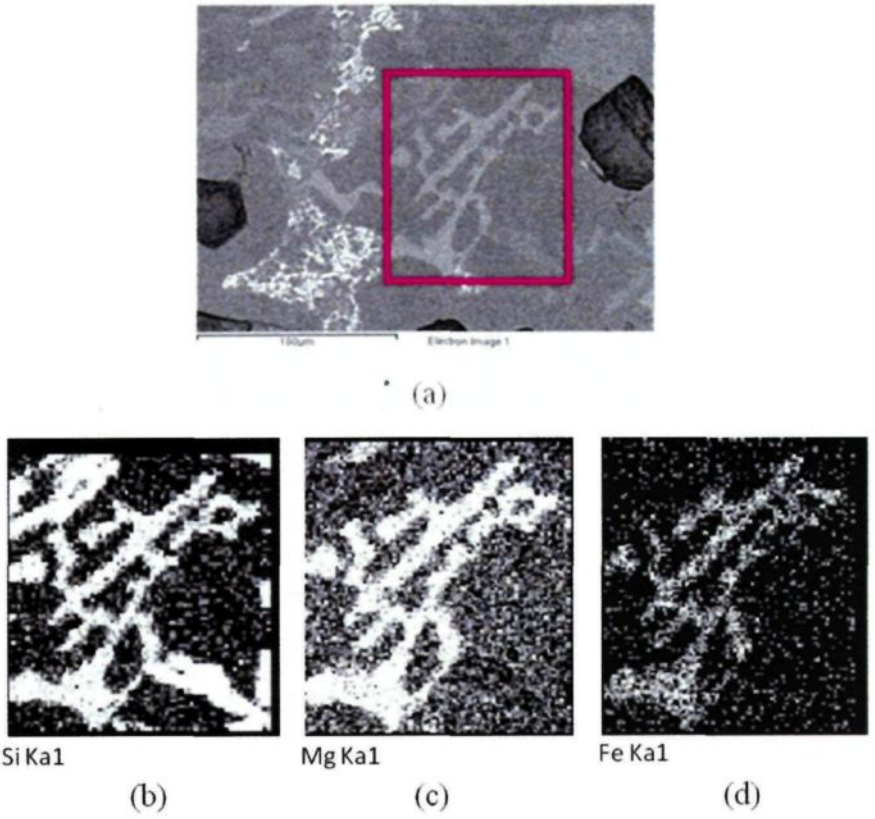

Fig. 5.10 (a) Backscattered electron image of alloy A and corresponding X-ray images showing distribution of (b) Si, (c) Mg, and (d) Fe in the π-$Al_8Mg_3FeSi_6$ phase shown in the inset in (a).

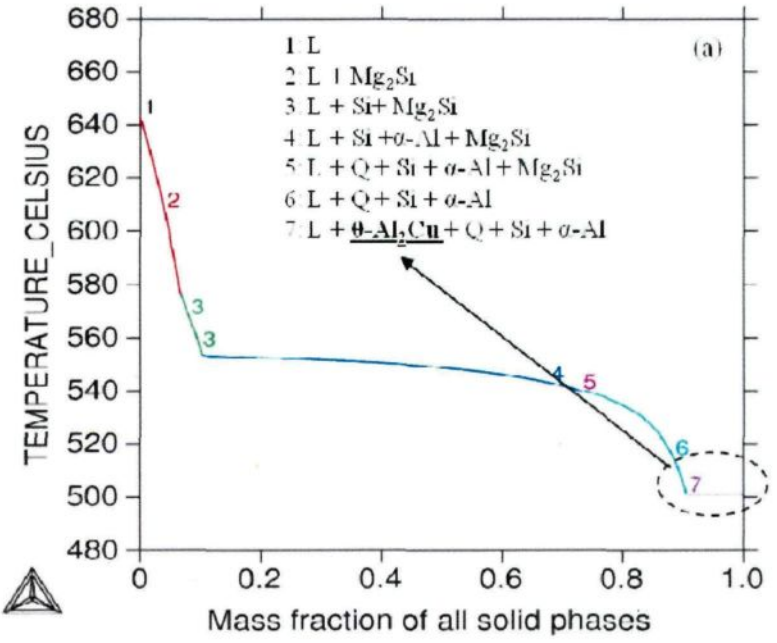

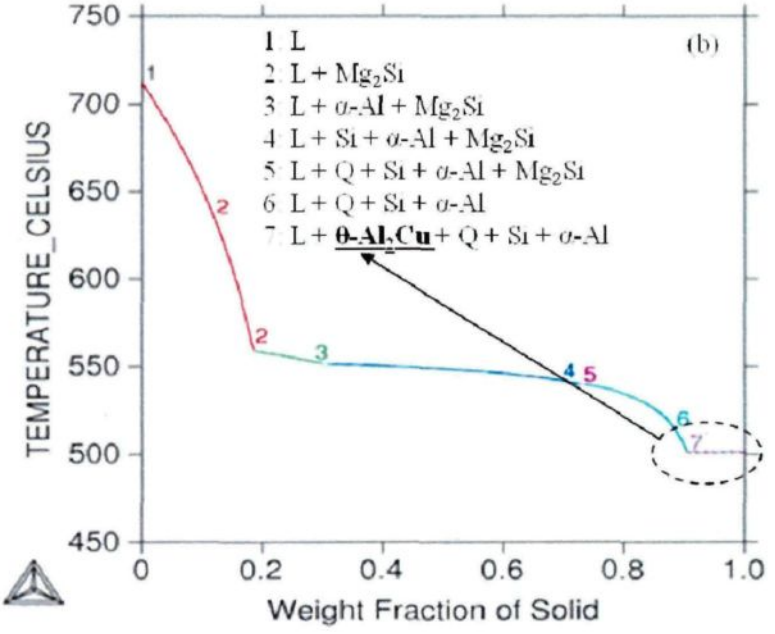

Fig. 5.11 Calculated Scheil solidification paths for (a) Alloy B with 8.4% Mg, and (b) Alloy D with 14.86%Mg.

Table 5.6 Main Reactions Observed from the Thermal Analysis of alloys A, B, C and D used in the present study.

Alloy Code	Reaction Number	Temperature Measured (°C)	Temperature predicted (°C)	Type of Reaction	Solidification Stage
A	1	588	609	L+Mg_2Si	Primary phase
	2	555	587	L+Si+ Mg_2Si	Pre-eutectic
	3	538	554	L+Si+α-Al+ Mg_2Si	Main eutectic
	4	528	-	L+ π-Fe + Si+α-Al	Post-eutectic
	5	520	539	L+Q + Si+α-Al+ π-Fe + Mg_2Si	
	6	495	365	Al_2Cu+ Q + Si+α-Al+π-Fe +Mg_2Si	
B	1	626	643	L+Mg_2Si	Primary phase
	2*	602	576	L+Si+ Mg_2Si	Pre-eutectic
	3	533	554	L+Si+α-Al+ Mg_2Si	Main eutectic
	4	525	-	L+ π-Fe + Si+α-Al +Mg_2Si	Post-eutectic
	5	520	539	L+Q + Si+α-Al+ π-Fe +Mg_2Si	
	6	495		Al_2Cu+Q + Si+α-Al+ π-Fe +Mg_2Si	
C	1	678	693	L+Mg_2Si	Primary phase
	2	532	553	L+Si+α-Al+ Mg_2Si	Main eutectic
	4**	-	-	L+ π-Fe + Si+α-Al +Mg_2Si	Post-eutectic
	5	519	539	L+ Q + Si+α-Al+ π-Fe + Mg_2Si	
	6	494	-	Al_2Cu+Q + Si+α-Al+ π-Fe +Mg_2Si	
D	1	707	711	L+Mg_2Si	Primary phase
	2	536	559	L+ α-Al+ Mg_2Si	Pre-eutectic
	3	531	552	L+Si+α-Al+ Mg_2Si	Main eutectic
	4**	-	-	L+ π-Fe + Si+α-Al +Mg_2Si	Post-eutectic
	5	514	539	L+ Q + Si+α-Al+ π-Fe + Mg_2Si	
	6	492	-	Al_2Cu+Q+ Si+α-Al+ π-Fe + Mg_2Si	

* The predicted temperature of Reaction 2 in Alloy B is lower than the measured temperature.

** The precipitation of π-$Al_8Mg_3FeSi_6$ phase - Peak 4 in the first derivative curves of Alloys A and B could not be clearly observed in Alloys C and D. However, the microstructures of the four alloys showed the formation of this phase.

5.4 Summary

The effect of the addition of Mg (6 to 15%) on the solidification behaviour and microstructural evolution of hypereutectic Al-15Si-4Cu-Mg alloys was investigated using thermodynamic calculations and thermal analysis, accompanied by extensive microstructural examination. It was found that the presence of Mg strongly influences the microstructure and solidification characteristics. From the analysis of the results obtained, the following conclusions were drawn.

1. Thermodynamic calculations using ThermoCalc software revealed the occurrence of six reactions during the solidification of the Al-Si-Cu-Mg alloys investigated, comprising (i) formation of *primary* Mg_2Si, two *pre-eutectic* binary reactions which produced (ii) Mg_2Si + Si or (iii) Mg_2Si + α-Al, (iv) the *main ternary eutectic* reaction with the formation of Mg_2Si + Si + α-Al, and two *post-eutectic* quaternary reactions showing the formation of (v) the Q-$Al_5Mg_8Cu_2Si_6$ phase and (vi) the θ-Al_2Cu phase.
2. Although the ThermoCalc equilibrium phase diagram predicts the formation of the θ-Al_2Cu phase only up to 7 wt% Mg levels, the use of Scheil (non-equilibrium) conditions in calculating the solidification path show the presence of the θ-Al_2Cu phase at higher Mg levels.
3. Depending on the Mg level, the solidification follows three paths, with Types I and III resembling each other except in their pre-eutectic reactions. Type III shows the absence of any pre-eutectic reaction - at the critical Mg content of 12.52% which separates the phase diagram into two distinct regions: 5.2-12.52% Mg and 12.52-20% Mg. The liquidus, binary and ternary eutectic temperatures also vary based on the Mg content.

4. Microstructures obtained from all alloys (containing 0.3-0.4% Fe) showed the presence of the π-$Al_8Mg_3FeSi_6$ phase in addition to all the other phases. The presence of the π-phase was also detected in the cooling curves obtained from thermal analysis.
5. The growth of the Mg_2Si primary phase is strongly affected by Mg addition. As the Mg content is progressively increased, the morphology of the primary phase evolves from an octahedral to a faceted dendrite form. This change in morphology occurs at 12.52 wt% Mg. Further increase in Mg content only coarsens the dendrite Mg_2Si primary particles.
6. The results predicted from ThermoCalc and Scheil calculations show good agreement with the experimental data obtained from the microstructural and thermal analyses.

References

[1] L. Lasa and Rodriguez-Ibabe. J.M. Materials Science and Engineering A, 2003, vol. A363: 193-202.
[2] G. Timmermans and L. Froyen. Wear, 1999, vol. 230: 105-117.
[3] H.J. Kim. Journal of Materials Science Technology, 2003, vol. 19: 915-918.
[4] Alireza Hekmat-Ardakan, Frank Ajersch and X.-Grant Chen. Wear, 2010, vol. 269: 684-692.
[5] J. Jorstad and D. Apelian: International Journal of Metalcasting., 2009, vol.3: 13-43.
[6] [4] L. Arnberg, L. Bäckerud, G. Chai. American Foundrymen's Society: solidification characteristics of Aluminum Alloys, Skanaluminium, Universitetsforlaget AS. Oslo, Norway, 1986, V.3: 137-144.
[7] Alireza Hekmat-Ardakan, Frank Ajersch, X.-Grant Chen. Journal Materials Science, 2011, 46: 2370-2378.
[8] Alireza Hekmat-Ardakan, Frank Ajersch. Journal of Materials Processing Technology, 2010, 210: 767-775.
[9] A. Mandal and M. M. Makhlouf. Light Metals, TMS, San Francisco, CA, 2009: 57-62.
[10] Xiaochun Zeng, Makhlouf M. Makhlouf and Sumanth Shankar, Light Metal, TMS, Orlando, FL, 2007: 183-190.
[11] J. Zhang, Z. Fan, Y. Q. Wang and B. L. Zhou. Materials Science and Engineering A, 2000, vol. A281: 104-112.
[12] R. Hadian, M. Emamy, N. Varahram and N. Nemati. Materials Science and Engineering A, 2008, vol.490: 250-257.
[13] Q.D. Qin, Y.G. Zhao, W. Zhou and P.G. Cong. Materials Science and Engineering A, 2007, vol. 447: 186-191.
[14] Z. Zhang, Z. Fan, Y. Q. Wang and B. L. Zhou. Journal of Materials Science Letters, 2000, vol. 19: 1825-1828.
[15] Y.G. Zhao, Q.D. Qin, Y.H. Liang, W. Zhou and Q.C. Jiang. Journal of Materials Science, 2005, vol. 40: 1831-1833.
[16] J. Zhang, Z. Fan, Y.Q. Wang and B.L. Zhou. Scripta Materialia, 2000, vol. 42: 1101-1106.
[17] Alireza Hekmat-Ardakan and Frank Ajersch. Acta Materialia, 2010, vol. 58: 3422-3428.
[18] Y. Austin Chang, Shuanglin Chen, Fan Zang, Xinyan Yan, Fanyou Xie, Rainer Schmid-Fetzer, W. Alan Oates. Progress in Materials Science, 2004, 49: 313-345.
[19] H. Nami, A. Halvaee, H. Adgi and A. Hadian: J. Mater. Process. Technol., 2010, vol. 210, pp. 1282-1289.
[20] C. Li, Y. Y. Wu, H. Li, X. F. Liu. Acta Materialia, 2011, 59: 1058-1067.
[21] Y. Wang, X. N. Wang, Z. X. Mei, X. L. Du, J. Zou, J. F. Jia , Q. K. Xue, X. N. Zhang and Z. Zhang. Journal of Applied Physic, 2007, vol. 102(126),102.
[22] M. C. Flemings: Solidification Processing, McGraw-Hill, New York, 1974. :34.

CHAPTER 6

EFFECT OF P AND SR ON THE MICROSTRUCTURE OF HYPEREUTECTIC AL-15SI-14MG-4CU ALLOY

CHAPTER 6

EFFECT OF P AND SR ON THE MICROSTRUCTURE OF HYPEREUTECTIC AL-15SI-14MG-4CU ALLOY

6.1 Introduction

Hypereutectic Al-Si-Mg-Cu alloys with high Mg contents have been attracting much attention as an important lightweight material for potential application in the automotive and aerospace industries due to their relatively low density and good wear resistance as compared with other structural metals [1, 2]. These alloys can be also considered as *in-situ* aluminum matrix composites containing a large amount of Mg_2Si particles and could be potential candidates to replace traditional hypereutectic Al-Si-Cu alloys in engine applications. These Al-Mg_2Si composites show high potential as automobile brake disc material because the reinforcement Mg_2Si exhibits a high melting temperature of 1085 ^{0}C, low density of 1.99 x 10^3 kg m^{-3}, high hardness of 4.5 x 10^9 N m^{-2}, a low thermal expansion coefficient of 7.5 x 10^{-6} K^{-1} and a reasonably high elastic modulus of 120 GPa [3].

The microstructures of hypereutectic Al-Si-Mg alloys with high Mg content are essentially made up of two components, the proportions of which are governed by the alloy composition and solidification conditions. The two components are primary Mg_2Si particles and the Al-Si- Mg_2Si ternary eutectic. The addition of up to 4.5 % Cu to these alloys leads to the precipitation of θ-Al_2Cu and Q-$Al_5Mg_8Cu_2Si_6$ intermetallic compounds [4]. When Mg is present together with iron, there is an increased tendency to also form the π-Fe ($Al_8Mg_3FeSi_6$) phase [5].

However, under normal casting conditions, the hypereutectic Al-Si-Mg-Cu alloys with high Mg contents generally form undesirable, coarse dendritic primary Mg_2Si and brittle Chinese script Mg_2Si eutectic phase particles, which result in decreased mechanical properties of the alloys. Therefore, the refinement and modification of primary and eutectic Mg_2Si phases is considered to be one of the important means of improving the mechanical properties of such alloys.

The refinement of hypereutectic Al-Si-Mg-Cu alloys with high Mg contents is usually achieved by addition of rare earths [6], potassium fluotitanate [7], lithium [8], sodium salt [9], phosphorus [10] or strontium [11]. Among those chemical refiners, phosphorus is commonly used, resulting in AlP particles which act as effective nuclei for the primary Mg_2Si phase.

The modification of hypereutectic Al-Si-Mg-Cu alloys with high Mg contents relates to the transformation of the eutectic Mg_2Si phase from its Chinese script form into a fibrous form. The modification is generally carried out by adding modifiers like, Y [12], Sb [13] and Sr [14]. Jiang *et al.* [12] studied the effect of Y on the size and morphology of the Mg_2Si phase. The authors reported that addition of 0.8% Y to Mg-5%Si alloy effectively refined the primary Mg_2Si particles and the Chinese script Mg_2Si phase. Recent studies have also shown that Sr addition can significantly modify and refine the Chinese script-like Mg_2Si phase in Mg-Al-Si-based alloys [14]. It has also been shown that the modification effect of KBF_4 additions on the primary and eutectic Mg_2Si is more effective than that of K_2TiF_6 [15]. Recently, Li was added to the Al-Mg_2Si composite resulting in a significant change in size and morphology of primary Mg_2Si particles and a transition from flake to

coral-like morphology in the eutectic Mg_2Si structure [16]. However, while most of the studies reported in the literature have focused on the refinement of primary Mg_2Si, few studies have been carried out on the effect of modifiers on the size and morphologies of both primary Mg_2Si dendrite and Chinese-like eutectic Mg_2Si.

This part of the study was therefore undertaken to investigate the effects of phosphorus and strontium additions on the refinement and modification on the Mg_2Si phase (both primary and eutectic Mg_2Si) and π-Fe ($Al_8Mg_3FeSi_6$) phase in hypereutectic Al-Si-Mg-Cu alloys with high Mg contents. The mechanisms of refinement and modification of P and Sr with respect to primary and eutectic Mg_2Si phases and the π- $Al_8Mg_3FeSi_6$ phase are also discussed.

6.2 Materials and Methods

Commercial Al-50%Si, Al-50%Cu master alloys, pure magnesium (ingot, >99.9% purity) and pure Al (ingot, >99.9% purity) were used as the starting materials. The Al-Si and Al-Cu master alloys and pure Al were melted in a graphite crucible furnace. When the temperature reached 750 °C, pure Mg wrapped in aluminum foil was added in small increments into the Al-Si-Cu melt. The Cu-8% P and Al-10% Sr master alloys preheated at 300 °C were added into the melt at 800 °C. After being held for 15 min, the Al-15Si-14Mg-4Cu alloy melts were poured into steel dies to produce ingots. The chemical compositions of the alloys prepared are listed in Table 6.1.

Thermal analysis was performed to determine the eutectic nucleation temperature (T_N), growth temperature (T_G), and minimum temperature (T_{Min}). The characteristic temperatures are identified as the point where the cooling curve starts to bend and is detected more easily

with the help of the first derivative of the cooling curve. The difference ΔT between T_G and T_{Min} describes the recalescence of the eutectic arrest.

Table 6.1 Chemical composition of Al-15Si-14Mg-4Cu alloys used.

Alloy #	Elements (wt. %)						
	Si	Mg	Cu	Fe	P	Sr	Al
1	15.5	13.6	4.3	0.3		-	Bal.
2	15.5	13.5	4.3	0.4	0.4	-	Bal.
3	15.1	13.9	4.6	0.4		0.08	Bal.
4	15	13.8	4.1	0.3	0.4	0.08	Bal.

The eutectic (Si+ Mg_2Si) particles characteristics were quantified using an image analyzer (CLEMEX JS- 2000, PE 4.0) attached to the optical microscope, following the usual procedures employed for volume fraction or other measurements of any specified phase. The various phases observed in these samples were identified using optical microscopy and scanning electronic microscopy (SEM) coupled with energy dispersive X-ray spectroscopy (EDS) facility.

6.3 Results and Discussion

6.3.1 Effect of P and Sr on primary Mg_2Si particles

Fig. 6.2 shows optical micrographs of the cast alloys corresponding to the (a) base alloy (b) Sr addition (c) P addition (d) Sr + P addition. According to vertical section of the Al-Si-Mg-Cu equilibrium quaternary diagram (Fig. 6.1), the primary Mg_2Si phase will become rather coarse in the materials because of the broad temperature interval between the liquidus and solidus, and the microstructure of the composite should consist of primary Mg_2Si, α-Al, eutectic (Si, Mg_2Si) phases and Q phases. The microstructure of the unmodified alloy shown in Fig. 6.2a consists of dendritic primary Mg_2Si crystals,

surrounded by of coarse Al particles. The dark particles are the primary Mg_2Si and the bright phase is α-Al. The addition of 0.08% Sr did not alter the morphology and the size of the primary Mg_2Si significantly, as shown in Fig. 6.2b, which indicates that the effect of a strontium modifier on primary Mg_2Si is not significant. On the other hand, it is interesting to note that when P or P + Sr were added to the melt, the size of the primary Mg_2Si particles decreased from 350 to less than 60 μm, and their morphology changed from a dendritic to polyhedral shape, as shown in Fig. 6-2c-d, indicating that adding 0.4% P or a combination of 0.4% P and 0.08% Sr can effectively modify and refine the Mg_2Si primary phase.

In order to further characterize the size and the morphology changes of the primary Mg_2Si due to the P refinement, deep-etched samples were examined by SEM. Fig. 6.3b shows typical SEM micrographs of deeply etched primary Mg_2Si after addition of 0.4% P. These clearly reveal the transformation of the growth mode from anisotropic dendrite to isotropic polyhedrale.

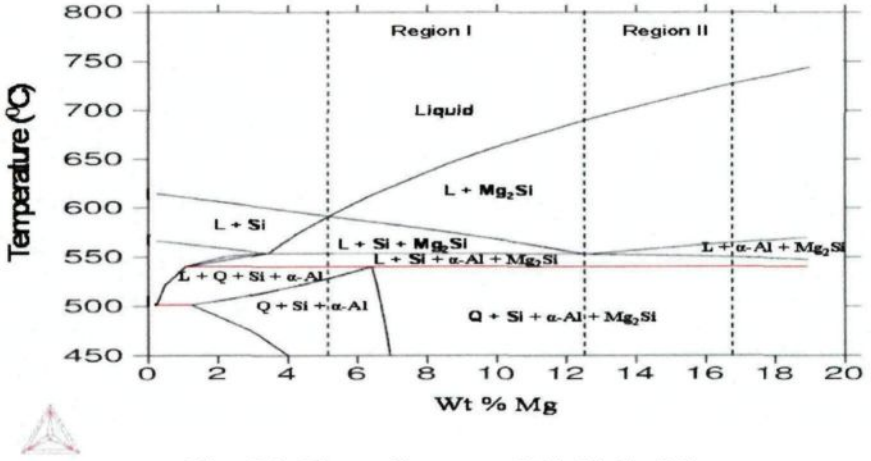

Fig. 6.1: Phase diagram of Al-Si-Cu-Mg system.

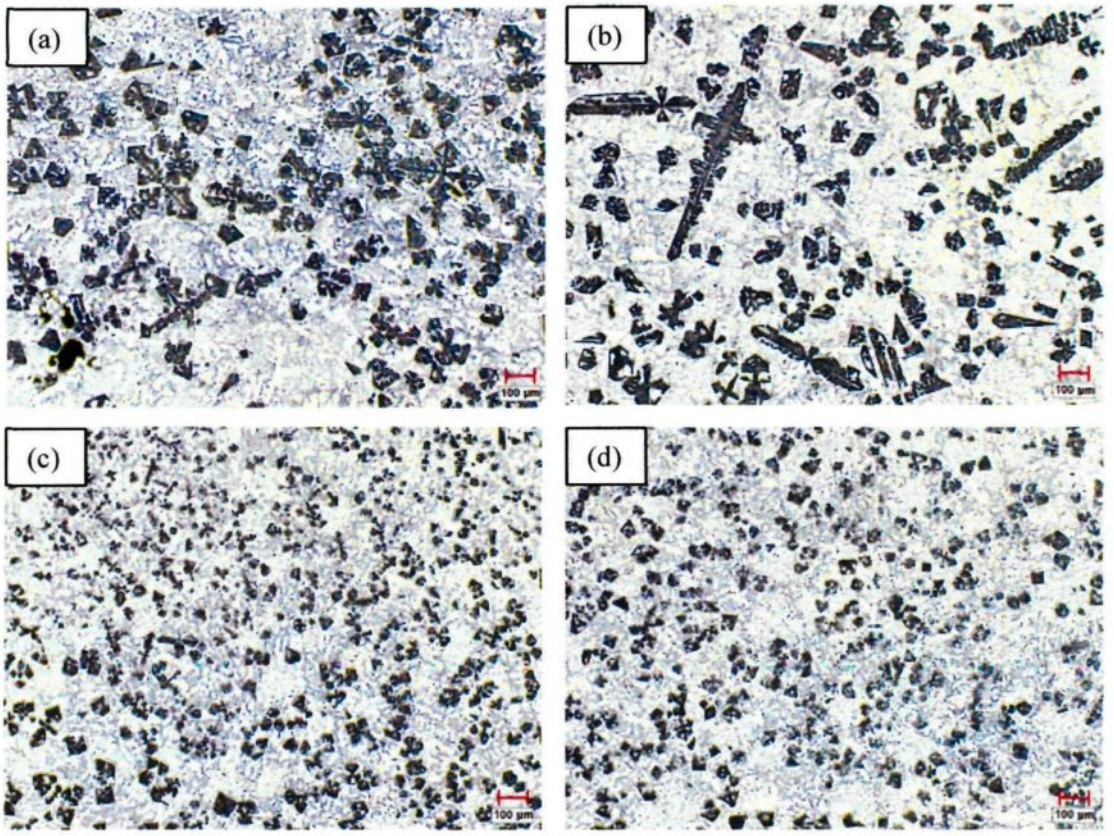

Fig. 6.2: Primary Mg_2Si morphologies of Al-15Si-14Mg-4Cu alloy containing: (a) no addition of P or Sr; (b) 0.08 % Sr; (c) 0.4 % P; (d) 0.08 % Sr and 0.4 % P.

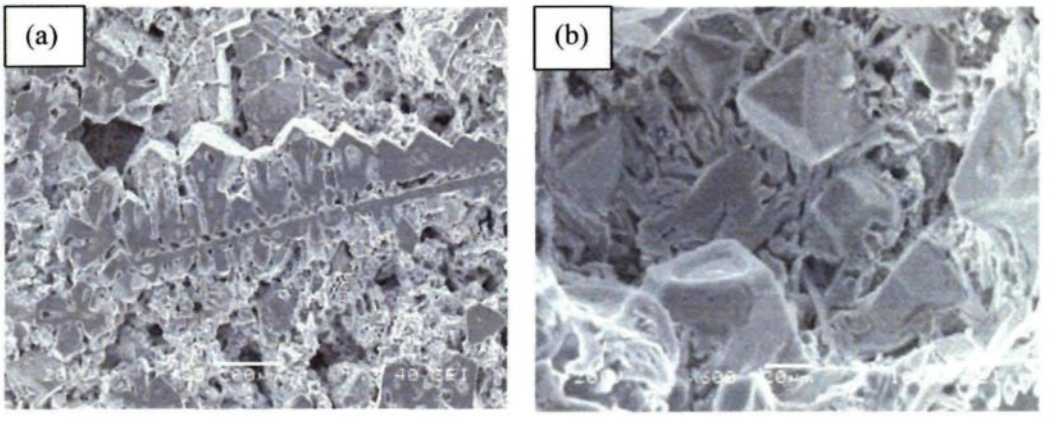

Fig. 6.3: The morphologies of primary Mg_2Si particles (a) unmodified (b) with 0.4% P.

Fig. 6.4 shows the effect of P and Sr on the size of primary Mg_2Si particles. Comparing the results of alloy A (base alloy) and alloy C (with 0.08% Sr), we can observe that Sr does not seem to affect the size of the primary Mg_2Si particles. However, the results for alloy B (0.4% P) and alloy D (0.4% P + 0.08% Sr) clearly illustrate the refinement of the primary Mg_2Si particles in these modified alloys as result of the addition of P. It is reasonable to conclude, therefore, that, the primary Mg_2Si particles are refined and modified significantly by the addition of P only.

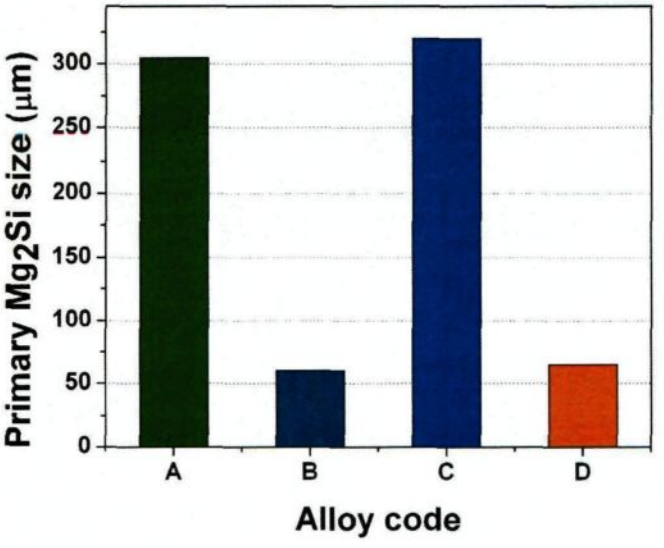

Fig. 6.4: The size of primary Mg_2Si particles in the alloy A (base alloy), alloy B (0.4% P), alloy C (0.08% Sr), and alloy D (0.08% Sr + 0.4% P).

According to the literature [10], the refining mechanism could be the results of two major effects, heterogeneous nucleation and/or a poisoning effect. In hypereutectic Al-Si alloys, phosphorus is well established as a primary silicon refiner, where it effectively refines and changes the morphology of the primary Si particles from a coarse star-like to a fine polyhedral shape. Recent studies have confirmed the nucleation mechanism of primary Si on AlP nuclei [17, 18]. Ho *et al.* [18] reported that AlP and Si are both of diamond cubic

structure with very similar lattice parameters. Consequently, primary Si can nucleate heterogeneously on the AlP particles with a C-C orientation relationship. However, in the absence of AlP there is increasing evidence that the primary Si nucleates and grows on oxide bifilms suspended in the melt [19]. In addition, when the AlP particles and oxide films are in competition, it has been reported that AlP is the preferred nucleant [20]. The action of P with respect to the primary Mg_2Si appears to be similar. In the absence of P, the primary Mg_2Si particles probably precipitate on the oxide film, but in the presence of AlP particles, the oxide is prevented from acting as a substrate, as AlP has a good lattice coherency with Mg_2Si, and can thus act as a nucleant, and thereby refine the primary Mg_2Si phase in Al-Si-Mg alloys [21].

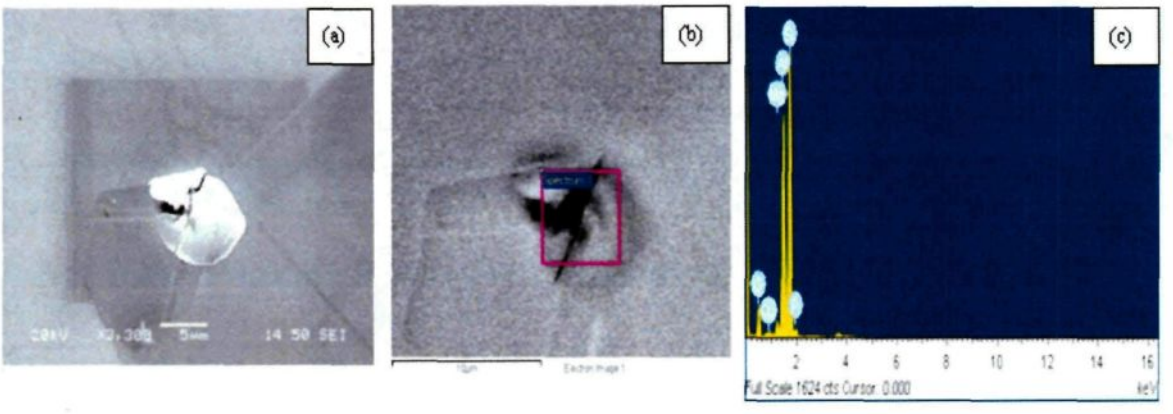

Fig. 6.5: SEM microstructure and EDS analysis of the P-containing phase in the 0.4% P modified alloy: (a) and (b) morphology and (c) EDS of P containing phase.

Fig. 6.5 shows an SEM image of primary Mg_2Si particles in the alloy containing 0.4% P. It is found that the Mg_2Si particles contained a small particle inside, which probably acted as nucleation sites for the primary Mg_2Si phase. Fig. 6.5(a) and (b) shows a typical

result on crystallization center of the nucleus in P-containing alloy by magnified secondary electron image. EDS analysis was used to confirm the chemical composition of the nucleus, and the results are shown in Fig. 6.5c. It was found that this particle probably consists of Al, Mg, Si and P. It is assumed that the Mg and Si peaks result from the primary Mg_2Si particle. According to the spectrum analysis, it would appear that the AlP compound can act as a nucleation site for the primary Mg_2Si phase during solidification.

6.3.2 Effect of P and Sr on eutectic phases

Figure 6.6 (a) and (b) shows an assembly of all cooling curves obtained from the hypereutectic Al-15Si-14Mg-4Cu alloys with different P and Sr contents. The cooling curve of the base alloy is also provided. Since the P and Sr content in the alloy is very low, the cooling curves do not show any peaks related to the formation of the P- and Sr-containing phases. However, the effect of the P and Sr concentrations is clearly illustrated in Fig. 6.6(a) and (b). It is observed in Fig. 6.6a that the formation temperature of primary Mg_2Si is not significantly changed with the addition of P or Sr. However, Sr addition causes a depression of the eutectic temperature. Table 6.2 shows the nucleation temperature (T_N), minimum temperature (T_{Min}), growth temperature (T_G) and the recalescence ($T_N - T_{Min}$). It can be seen that the nucleation temperature (T_N) of the unmodified alloy is 532 °C, and the growth temperature is 533.5 °C. The addition of 0.4% P did not alter the eutectic temperature. However, with the introduction of 0.08% Sr, these temperature decreased by about 11.6 °C and 14 °C, respectively reaching 521.4 °C and 519.7 °C. In addition, when a combination of 0.4% P and 0.08% Sr was added to the Al-15Si-14Mg-4Cu melt, the

nucleation temperature and growth temperature increased slightly, compared with that observed in Al-15Si-14Mg-4Cu alloy containing 0.08% Sr.

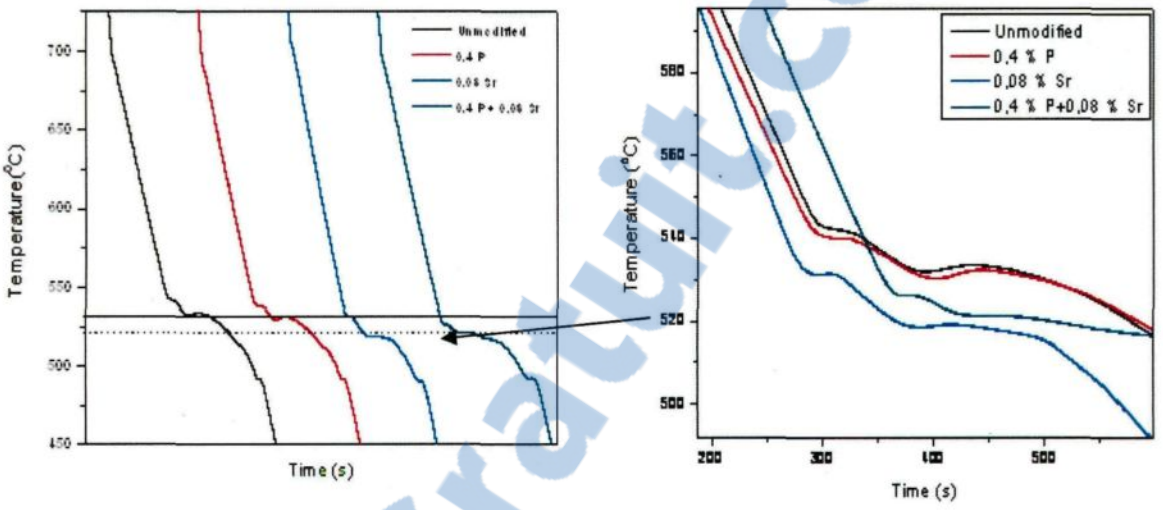

(a (b

Fig. 6.6: (a) Cooling curves of Al-15Si-14Mg-4Cu alloys, and (b) enlarged image of the arrowed area in (a).

Table 6.2 Effect of P and Sr on eutectic temperature of Al-15Si-14Mg-4Cu alloy.

Alloy Code	Alloy	T_N/°C	T_{Min}/°C	T_G/°C	ΔT/°C
1	Base alloy	532	532	533.5	1.5
2	0.4 P	530.5	529.4	531	1.6
3	0.08 Sr	521.4	518	519.7	1.7
4	0.4 P + 0.08 Sr	522.5	521	521.5	0.5

The microstructures of the eutectic matrix of the hypereutectic Al-15Si-14Mg-4Cu alloys with different P and Sr additions are compared in Fig. 6.7. It should be mentioned that the black Chinese script type particles are the eutectic Mg_2Si phase and the dark grey particles are the eutectic Si, while the light grey Chinese script particles correspond to the

π-Fe intermetallic compound. As Fig. 6.7a shows, the unmodified microstructure consists of plate-like Si particles and Chinese script Mg_2Si phase.

With Sr modification, the eutectic melt solidifies as a duplex mixture due to the changes that occur in the silicon and Mg_2Si morphology. As is shown in Figs. 6.7 (b) and 7(d), the addition of 0.08% Sr or a combination of 0.08% Sr and 0.4% P is sufficient to transform the flake-like Si and Chinese script Mg_2Si particles to fibrous morphology. However, with addition of only 0.4% P, the morphology of the eutectic (Si+ Mg_2Si) does not significantly change as shown in Fig. 6.7 c. In addition, it is clear that Sr addition also causes the refinement and modification of the π-$Al_8Mg_3FeSi_6$ intermetallic compounds in hypereutectic Al-Si-Mg-Cu alloy. Therefore it can be said that Sr treatment is effective for the simultaneous modification of both the eutectic Si and the eutectic Mg_2Si phases.

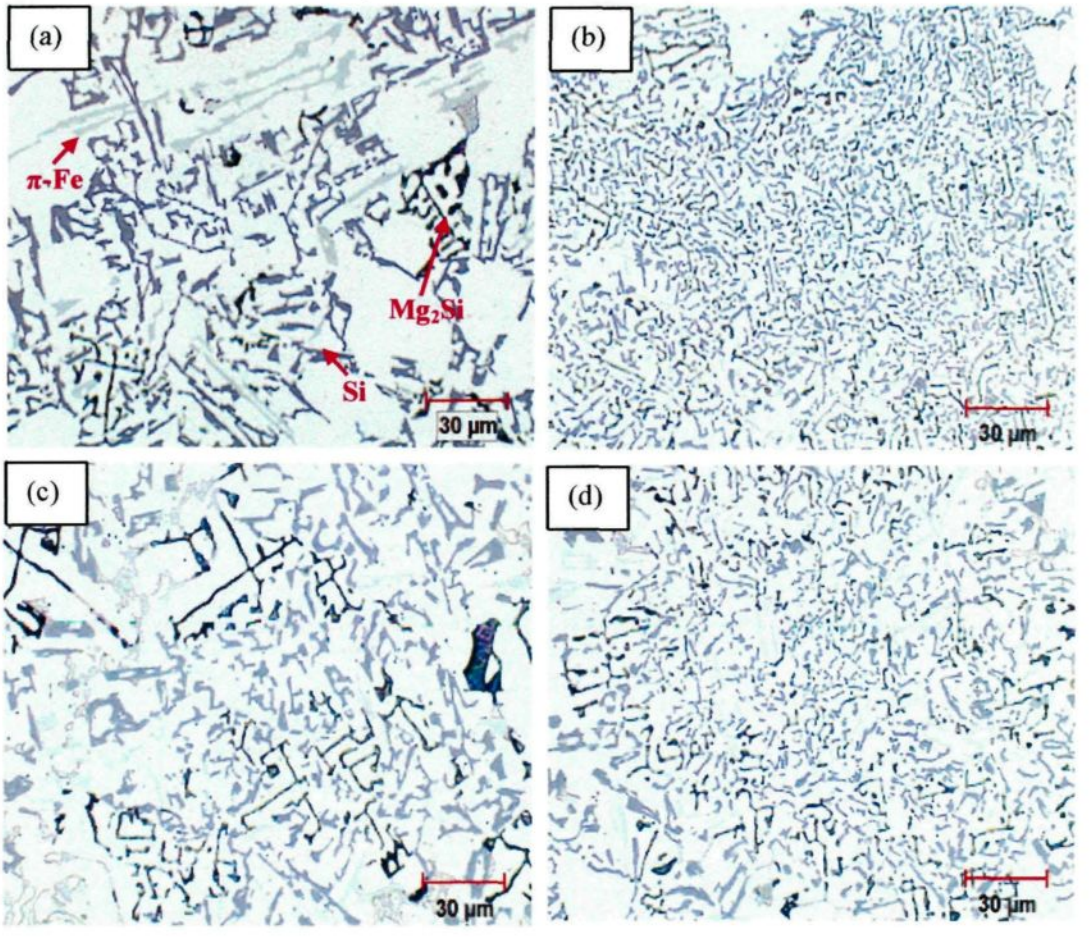

Fig. 6.7: Optical micrographs showing the effect of P and Sr on the eutectic matrix in the (a) unmodified alloy and alloys containing; (b) 0.08 % Sr; (c) 0.4 % P; (d) 0.08 % Sr + 0.4 % P.

6.3.3 Effect of Sr addition on the eutectic Mg_2Si

The optical microstructures of Al-15Si-14Mg-4Cu alloys are displayed in Fig. 6.8, demonstrate a substantial difference in the size and morphology of the eutectic Mg_2Si. As shown in Fig. 6.8a, the eutectic Mg_2Si phase in the unmodified hypereutectic Al-15Si-14Mg-4Cu alloy exhibits a coarse Chinese script morphology. However, after adding 0.04 wt% Sr to alloy, the Chinese script-shaped particles are partially modified by Sr as shown in Fig. 6.8b, but the refinement of the phase is not obvious. Furthermore, it is shown in Fig.

6.8c that the refinement and the modification with the addition of 0.08 wt% Sr is more pronounced than that obtained with 0.04 wt% Sr addition. Comparing Fig. 6.8b-c, it is interesting to observe that, after adding 0.08 wt% Sr to the Al-15Si-14Mg-4Cu alloy, the eutectic Mg_2Si phase in the alloy become very fine, and the morphology changes from initial Chinese script-shaped to a more granular shape, indicating that adding 0.08wt% Sr can effectively refine and modify the eutectic Mg_2Si phase.

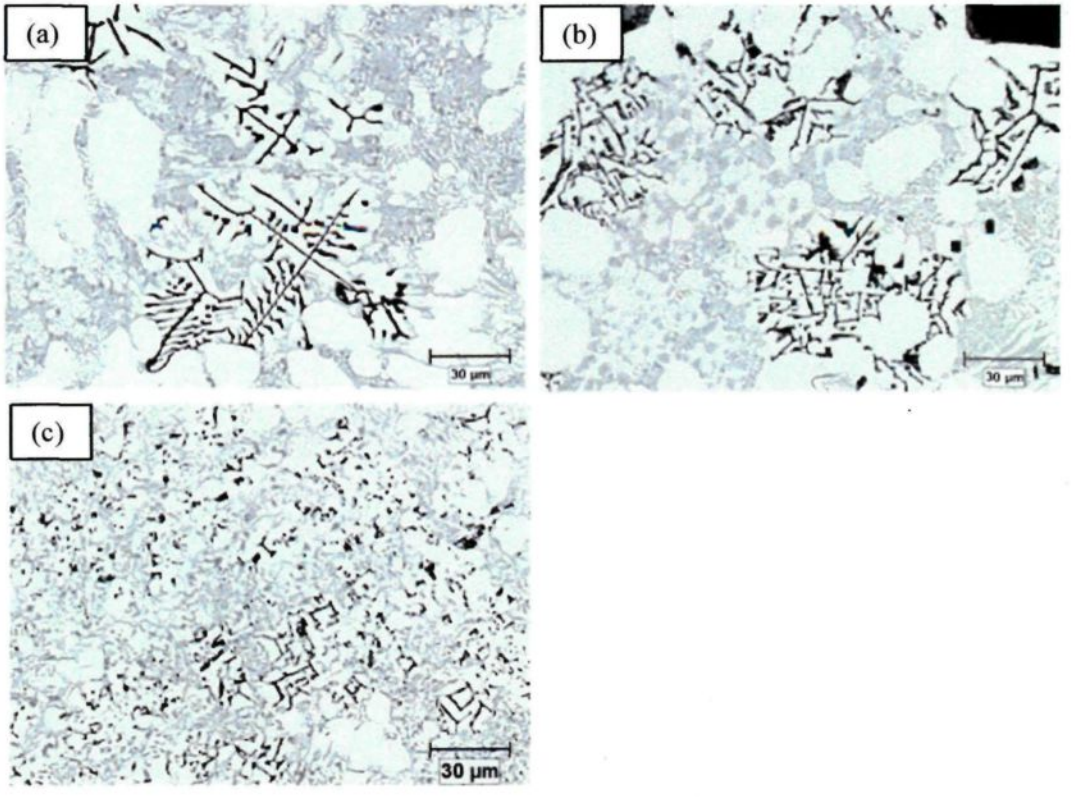

Fig. 6.8: Eutectic Mg_2Si morphologies of Al-15Si-14Mg-4Cu alloy modified with (a) 0 % Sr; (b) 0.04 % Sr; (c) 0.08 % Sr.

The scanning electron micrographs of the eutectic Mg_2Si phase in the unmodified and modified Al-15Si-14Mg-4Cu alloys are clearly shown in Fig. 6.9a, b. With the addition of Sr, the morphology of eutectic Mg_2Si changes from Chinese script shape to a refined fibrous one as shown in Fig. 6.9 b.

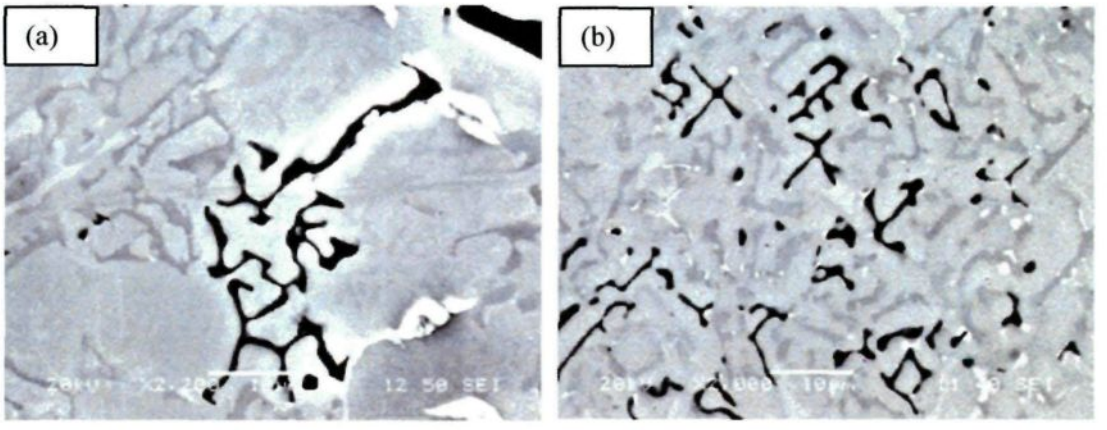

Fig. 6.9 SEM micrographs showing the eutectic Mg_2Si deep etched samples of the Al-15Si-14Mg-4Cu alloy modified with (a) 0 % Sr; (b) 0.08 % Sr.

To quantitatively determine the effects of P and Sr addition on the size and morphology of the eutectic Mg_2Si and Si phases, the particle area and density of these two phases were measured in alloys samples A through D using an image analyzer. Fig. 6.10 and Fig. 6.11 illustrate the results obtained from these measurements. The mean particle area of eutectic Si and Mg_2Si phases as a function of addition of P or/and Sr is displayed in Fig. 6.10. The mean area of Si particles decreases from 3.8 (alloys A and B) to 2.5 μm^2 (alloys C and D) and that of Mg_2Si from 6 (alloys A and B) to 1.7 μm^2 (alloys C and D) respectively. The large decrease of the mean area values of eutectic Si and Mg_2Si phases obviously reveals the refinement of both Si and Mg_2Si phases through Sr addition.

Fig. 6.10 shows the particle density of the two eutectic phases in the unmodified alloy and in the P and Sr-containing alloys. The results indicate that the density of the eutectic Si and eutectic Mg_2Si phase particles are increased with the addition of Sr modifier due to their reduction in size during refinement.

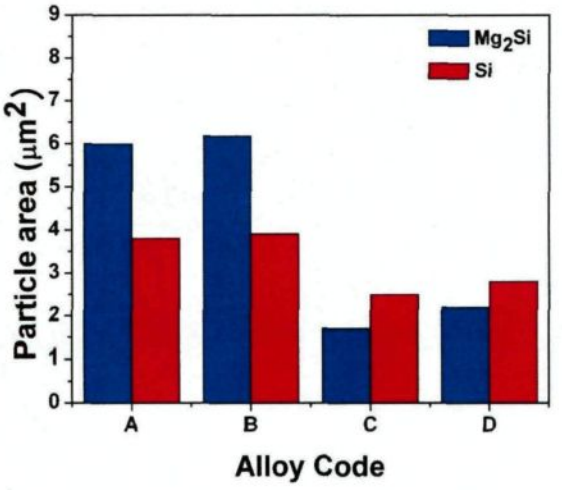

Fig. 6.10: The particle area of eutectic Mg_2Si and Si in the alloy A (no addition of P or Sr), alloy B (0.4% P), alloy C (0.08% Sr), and alloy D (0.08%

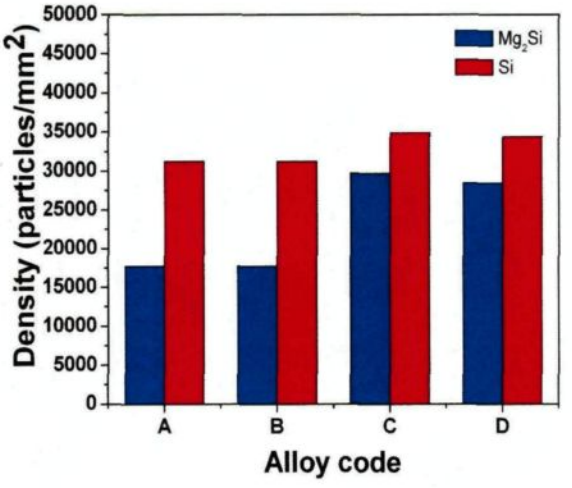

Fig. 6.11: Density of eutectic particles in the alloy A (no addition of P or Sr), alloy B (0.4% P), alloy C (0.08% Sr), and alloy D (0.08% Sr + 0.4% P).

Generally, the eutectic Mg_2Si phase in the unmodified Al-Mg-Si base alloys tends to form as coarse Chinese script-like particles at lower solidification rates [22] as shown in Fig. 6.8a. However, the experimental results indicate that with the addition of Sr the morphology of eutectic Mg_2Si changed from coarse Chinese script to a refined fibrous structure (Fig. 6.8c). Yuan *et al.* [23] examined the effect of Sb on the modification of eutectic Mg_2Si in Mg-5Al-1Zn-1Si alloy and concluded that the modification of the Chinese script Mg_2Si phase was achieved through Mg_3Sb_2 particles which acted as nuclei for the Mg_2Si phase. The morphology of the Mg_2Si phase changed from Chinese script to small polygonal particles. However, the Mg_2Si phase precipitates before the Mg_3Sb_2 phase, because the eutectic temperature for Mg-Si system is higher than the precipitation temperature of Mg_3Sb_2. Consequently, Mg_3Sb_2 cannot act as nucleation site for the nucleation of Mg_2Si. Recently, Mingbo *et al.* [14] reported that the modification and refinement of the Chinese script Mg_2Si phase are related to the effects of Sb, Sn, and Sr on the undercooling. These authors suggested that the refinement and modification of eutectic Mg_2Si phase are closely related to the limited solid solubility of Sr in magnesium and the increase in the undercooling with Sr addition. In addition, Sr enriches the liquid in front of the Mg_2Si growing interface, which restricts Mg_2Si growth during solidification, while the increase in undercooling results in increasing the effective number of potential Mg_2Si nuclei. However, while the exact mechanism responsible for the modification and refinement of the Chinese script Mg_2Si phase has not been confirmed, the formation of Sr-rich intermetallics, such asAl_4Sr, in Sr-modified alloys has been proposed to be a contributing factor [24]. It was reported [24] that the orientation relationship between Al_4Sr

and Mg_2Si has a low disregistry value of 0.69% at $(100)_{Al4Sr}$ // $(100)_{Mg2Si}$, and that the mechanism of modification of the Mg_2Si phase in Sr- containing AZ61-0.7Si alloy may be related to the formation of the Al_4Sr phase which can serve as a heterogeneous nucleus for the Mg_2Si particles. It should be pointed out that no quantitative analysis on the refinement effect of Sr on AZ61-0.7Si alloy was carried out, and therefore, the proposed mechanism of modification cannot be firmly confirmed.

The quantitative analysis (Fig. 6.10 and Fig. 6.11) indicated that an addition of 0.08% Sr or a combined addition of 0.08% Sr + 0.4% P decreases the particle area and increases the density of Mg_2Si phase particles, which might support the heterogeneous nucleation mechanism. In addition, in our experiments Al_2Si_2Sr intermetallic phase was found attached to the eutectic Mg_2Si particles as shown in Fig. 6.12, so that the addition of Sr probably rendered the AlP nuclei ineffective.

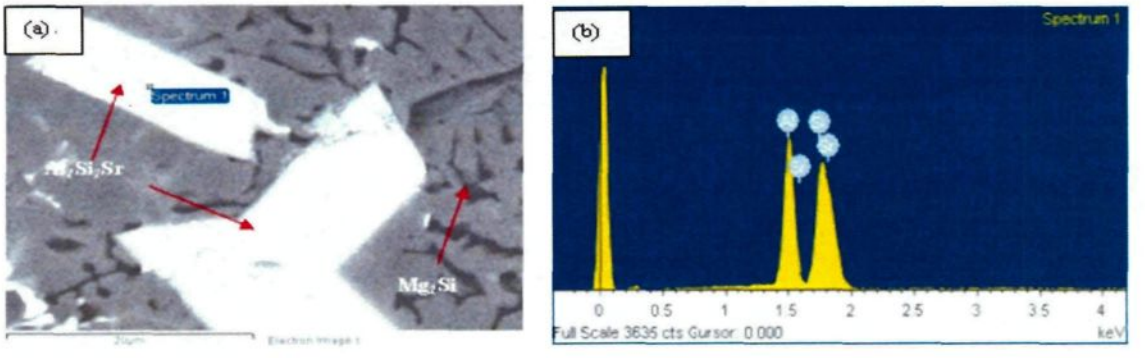

Fig. 6.12 (a) SEM image of the Al_2Si_2Sr intermetallic phase in Sr-modified Al-15Si-14Mg-4Cu alloy and (b) EDX of the Al_2Si_2Sr phase.

6.3.4 Effect of Sr on the formation of π-$Al_8Mg_3FeSi_6$ in Al-15Si-14Mg-4Cu alloy

Figure 6.13a shows the microstructure of the Sr-free sample. This microstructure contains flake-like eutectic Si particles, Chinese script-like eutectic Mg_2Si particles and

coarse π-Chinese script-like intermetallic compound. This figure also demonstrates that the π-Fe phase has a complicated branched structure as indicated in the picture. However, with the Sr addition the eutectic Si and Mg_2Si phases are well refined and the π-phase becomes modified, resulting in and a less branched structure as shown in Fig. 6.13b, c. Fig. 6.13c also shows that the Sr addition transforms the long Chinese script-like π-Fe phase particles into a very fine and branched particles. This can be clearly observed in the SEM images of the deep-etched alloy sample shown in Fig. 6.14. SEM images also show that the π-Fe phase observed as Chinese script-like (Fig. 6.14a) has a twin platelet shape structure with much less branching.

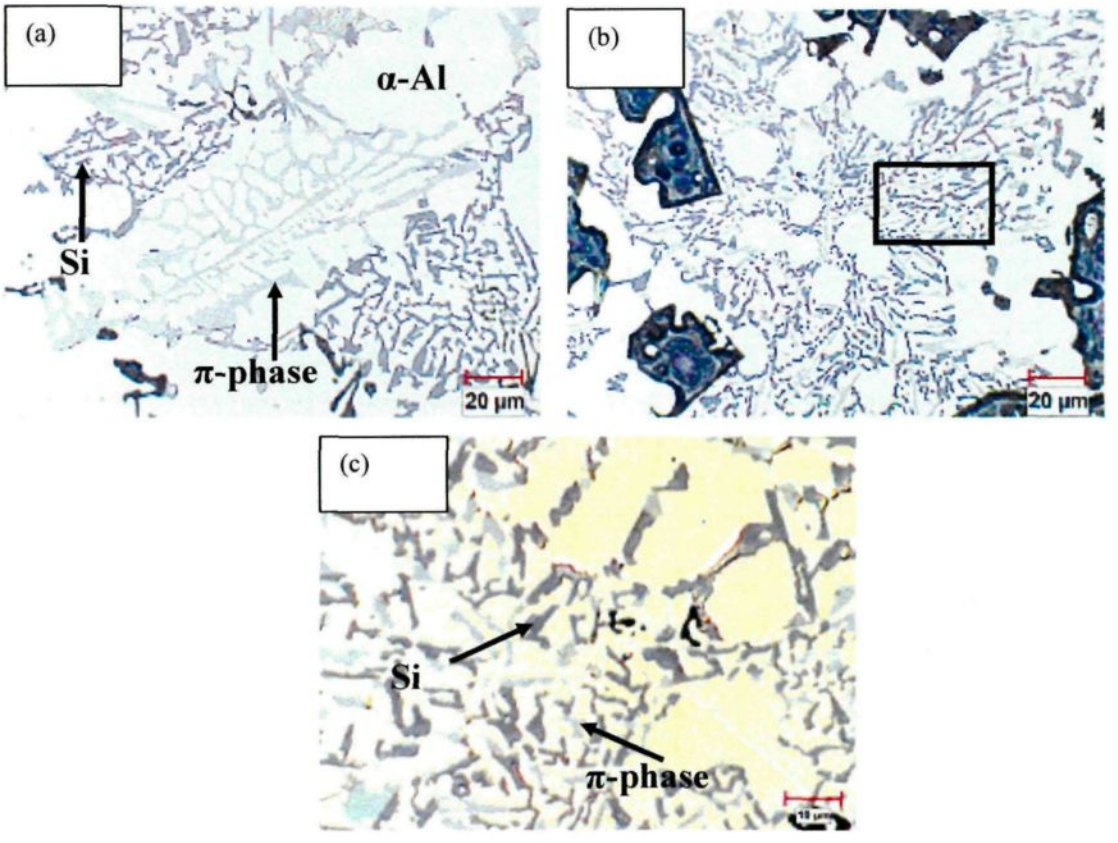

Fig. 6.13 Optical micrographs of: (a) alloy without modifier, (b) alloy with 0.08 pct Sr, (c) high magnification micrograph corresponding to the inset shown in (b).

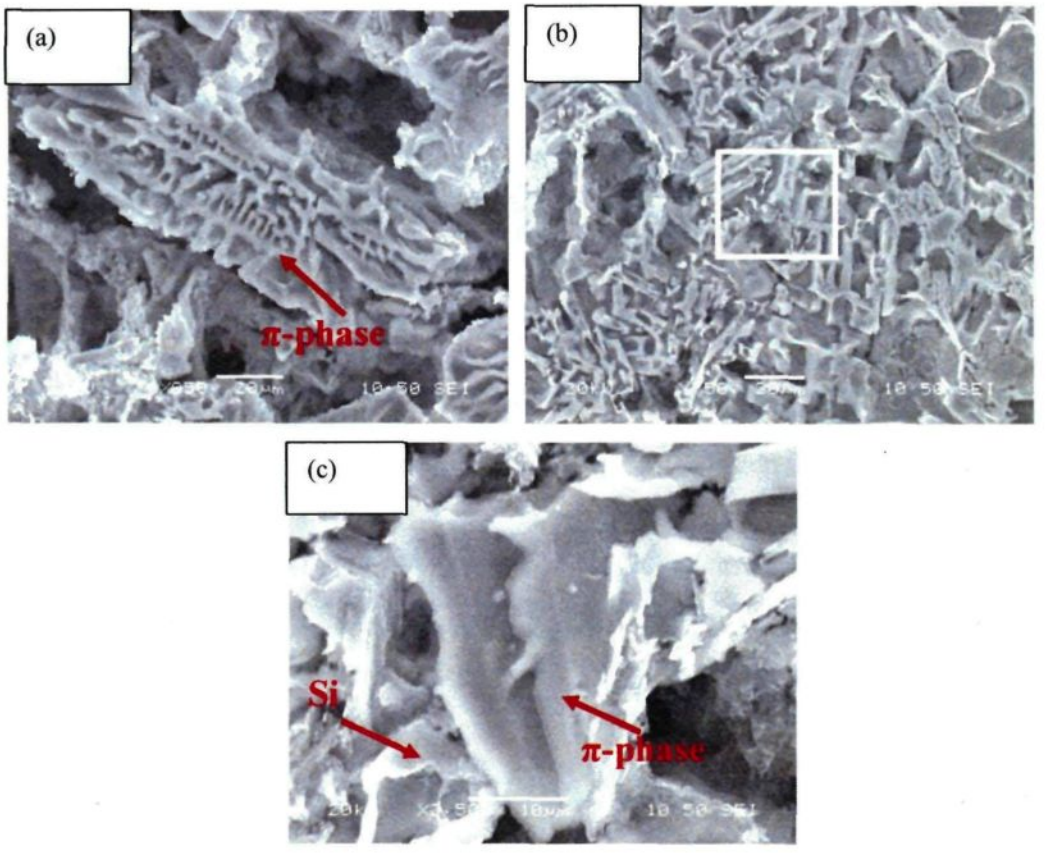

Fig. 6.14 SEM images showing π-Fe morphology in deep etched samples of: (a) alloy without modifier, (b) alloy with 0.08 pct Sr, (c) high magnification image of inset shown in (b).

EBSD and EDS analyses in SEM were used to identify the iron phase in the Sr-free and Sr added Al-15Si-14Mg-4Cu alloys. Table 3 provides the atomic and elemental wt% of Fe-rich phase with the corresponding chemical formulae in both alloys. The chemical composition of the iron intermetallic phase in each alloy represents the average of six EDS measurements performed on the phase particles taken from various areas of the microstructure. EDS analysis of the Fe-rich phases in the unmodified and Sr-modified microstructures revealed the presence of iron, magnesium, aluminium and silicon with no

significant difference in overall composition of the Fe-rich phases in the two alloys. These iron phases can be considered as being the π-$Al_8Mg_3FeSi_6$ phase as shown in Table 6.3.

Table 6.3 Average compositions and chemical formulae of π-phase observed in the studied alloys

Alloy	Phase	Element	wt%	at%	calculated formula	Suggested formula
Base alloy	Fe-rich phase	Al	53.91 ± 3.49	56.13 ± 3.46	$Al_{13.3}Mg_{3.5}FeSi_{5.9}$	$Al_8Mg_3FeSi_6$
		Mg	12.68 ± 1.13	14.69 ± 1.87		
		Fe	8.48 ± 0.64	4.20 ± 0.27		
		Si	24.91 ± 2.02	24.93 ± 2.09		
Sr-modified Alloy	Fe-rich phase	Al	45.32 ± 0.19	47.35 ± 0.40	$Al_{8.8}Mg_{3.5}FeSi_{5.3}$	$Al_8Mg_3FeSi_6$
		Mg	15.88 ± 1.17	18.51 ± 1.68		
		Fe	10.48 ± 0.97	5.36 ± 0.56		
		Si	28.30 ± 1.87	28.64 ± 1.78		

The EBSD results of the iron phase in the unmodified and Sr-modified alloys are shown in Fig. 6.15. All compounds listed in Pearson's Handbook [25] containing iron, silicon, aluminium and/or magnesium were therefore selected as possible phases for identification and their crystallographic data were entered into Channel 5 system software database. EBSD analyses were performed from many different Fe-rich phase particles in the unmodified and Sr-modified alloy samples. The particle in the unmodified alloy (Fig. 6.15a) has classic Chinese script morphology, and an EBSD pattern for this particle is shown in Fig. 6.15b-c. In modified alloys, Fe-rich phase particles did not exhibit Chinese script shape but fine branched shape (Fig. 6.15d). In both Sr-free and Sr-modified alloys, EBSD patterns obtained from these iron phases were consistent with the standard hexagonal π-$Al_8Mg_3FeSi_6$ phase (see Fig. 6.16a-f), which has space group p62m, a = 0.662 nm and c = 0.792 nm, y =120^0 [25].

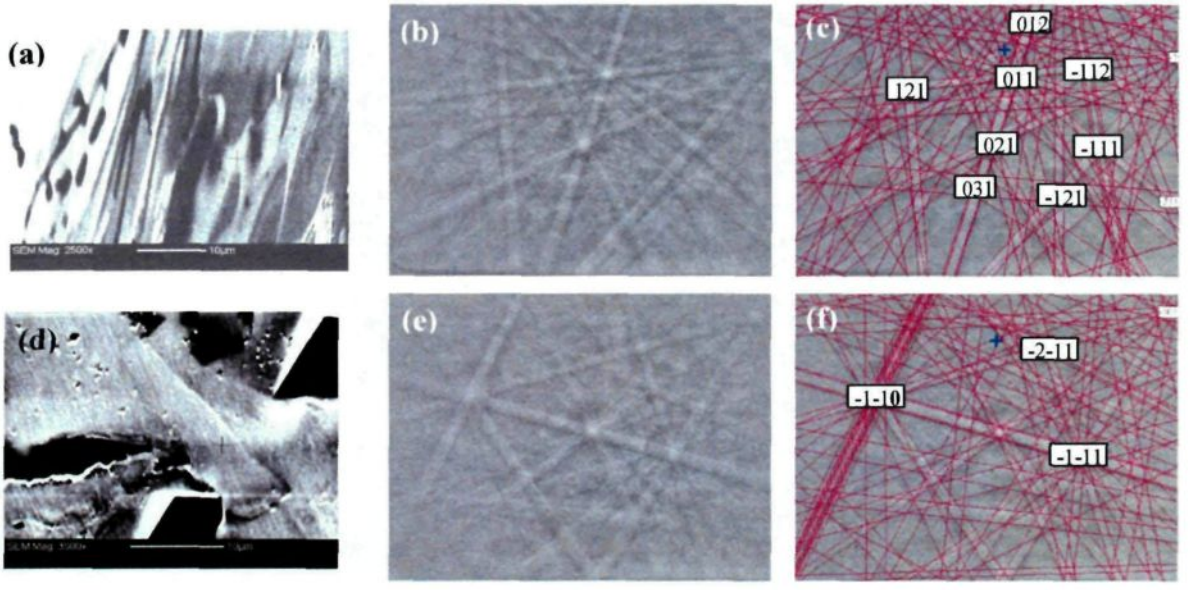

Fig. 6.15 SEM image and representative experimental EBSD patterns with HKL Channel 5 simulations (a-c) unmodified alloy (MAD = 0.209), (d-f) Sr-modified alloy (MAD =0.201).

The image analysis of π-Fe phase results as shown in Fig. 6.16 clearly indicate that the particle area of π-phase decreases and that the density of particles increases by the addition of 0.08% Sr. Thus, Sr is an effective element in modification and refinement of the Chinese script-like π-Fe intermetallic compound.

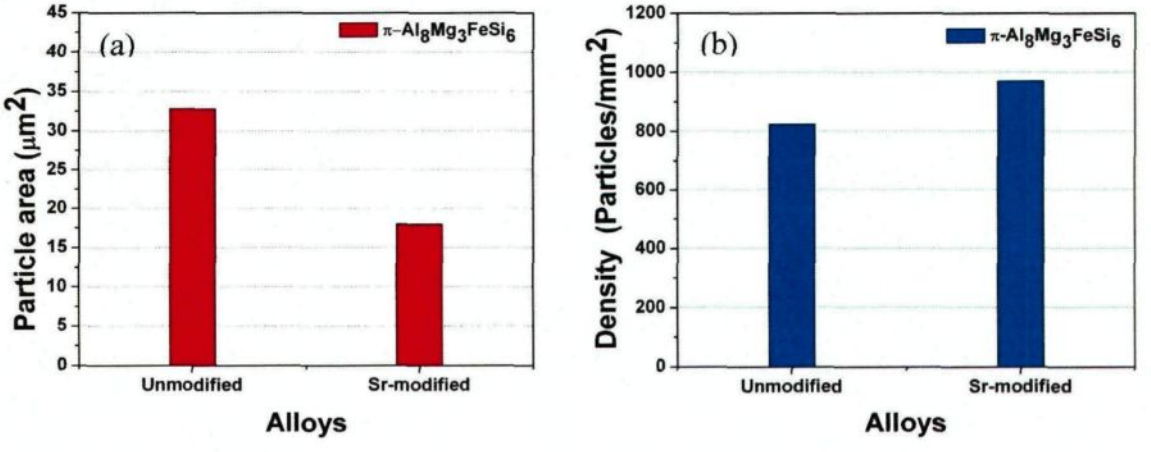

Fig. 6.16 Effect of Sr addition on the (a) particle area of π-phase particles, (b) density of π-phase particles of Al-15Si-14Mg-4Cu alloy.

Generally, the π-Fe phase in unmodified Al-Si-Mg based alloys tends to form coarse Chinese script particles. Therefore, the iron phase in the Al-15Si-14Mg-4Cu alloy content exhibit typical Chinese script shaped morphology (Fig. 6.14a). However, the experimental results showed that the addition of Sr changes the morphology of π-Fe phase from coarse Chinese script to refined twin platelets. In addition, it can be seen that Sr treatment is also effective for simultaneous modification of the eutectic silicon and the π-Fe phase.

The mechanisms of the modification of the π-Fe intermetallic compound by strontium can be explained in terms of the nucleation and growth of the π-phase. The number of the π-$Al_8Mg_3FeSi_6$ particles per unit area correlates with the nucleation mechanism. The increase in the number of the π-$Al_8Mg_3FeSi_6$ particles per unit area indicates that the nucleation process of the π-phase is influenced by Sr addition. A change in the interfacial surface energy by addition of Sr may affect the nucleation process where Sr may reduce the interfacial surface energy between α-Al and π-Fe phases. Mondolfo [26] has reported the same effect for the nucleation of the eutectic Si. He concluded that Na reduces the surface tension of the α-Al phase and thus changes the interfacial surface energy between the α-Al and Si phases which may influence the nucleation of the Si phase. In addition, the number of nucleation sites and the undercooling are two factors which may influence the formation of the π and the eutectic phases during solidification. It was reported that in Al-Si alloys containing P, aluminum phosphide (AlP) can act as an effective nucleation site for the Si phase and the presence of AlP coarsens the eutectic Si [27]. Yaneva *et al.* [28] reported that Sr refines the Si particles and, to a certain degree, the iron intermetallics as well, probably due to the undercooling at the solidification front caused by the Sr addition. Therefore, the

strontium addition has a significant influence on π-Fe phase nucleation by affecting nucleation sites and resulting in undercooling.

On the other hand, the average π-Fe particles area correlates with the growth mechanism. The decreased average particles area of the π-Fe phase in the Sr added alloy indicates that the growth of these intermetallics is greatly suppressed by the Sr addition. This is similar to the well-known effect of Sr in modifying the growth of the eutectic silicon in Al-Si alloys [29]. Samuel *et al.* [30] reported that the preferential nucleation of the *β*-needle-like phase results in branching and formation of large *β*-phase particles. The same nucleation behaviour has been observed for the nucleation of the π-Fe phase. The results indicate that the Sr hinders the preferential nucleation on a parent *β*-phase or on π phase particle, and as a result modification with less branching of these phases can be expected.

6.4 Summary

The effects of individual and combined addition of P and Sr on the microstructure of hypereutectic Al-15Si-14Mg-4Cu alloy were investigated. The observed microstructure of as-cast Al-15Si-14Mg-4Cu alloy consists of coarse dendritic primary Mg_2Si, α-Al, eutectic silicon and Chinese script-like Mg_2Si. With the addition of phosphorus, the morphology of primary Mg_2Si particles changed from dendritic or equiaxed to polygonal and their size decreased from 350 μm to 60 μm. With the addition of Sr, the eutectic Mg_2Si morphology changes from coarse Chinese script-like to a fine fibrous structure, and the modification level increased with increasing level of Sr addition. Furthermore, simultaneous refinement of both primary and eutectic Mg_2Si was achieved with a combined addition of phosphorus and strontium. However, the refinement and modification effects on the eutectic Mg_2Si and eutectic Si with the combined addition of P and Sr are less effective than those of Sr addition alone. In the unmodified alloy, the π-Fe phase was present as a coarse Chinese script structure. However, in the Sr-modified alloys, the morphology of the π-Fe phase changed from Chinese script to a fine twin platelet form. The presence of the π-Fe phase was confirmed by EDS and EBSD analyses.

References

[1] Alireza Hekmat-Ardakan, Xichun Liu, Frank Ajersch, X.-Grant Chen. Wear, 2010, 269: 684-692.
[2] Yavuz Sun, Hagrettin Ahlatci. Materials and Design, 2011, 32: 2983-2987.
[3] J. Zhang, Z. Fan, Y. Q. Wang, B. L. Zhou. Materials Science and Engineering A, 2000, 281: 104-112.
[4] Alireza Hekmat-Ardakan, Frank Ajersch. Acta Materialia, 2010, 58: 3422-3428.
[5] C. T. Wu, S. L. Lee, M. H. Hsieh, J. C. Lin. Metallurgical and Materials Transactions A, 2010, 41 A: 751-757.
[6] Y. G. Zhao, Q. D. Qin, W. Zhou, Y. H. Liang. Journal of Alloys Compounds, 2005, 389: L1-L4.
[7] Y. G. Zhao, Q. D. Qin, Y. Q. Zhao, Y. H. Liang, Q. C. Jiang. Materials Letters, 2004, 58: 2192- 2194.
[8] R. Hadian, M. Emamy, J. Campbell. Metallurgical and Materials Transactions B, 2009, 40B: 822-832.
[9] M. Emamy, R. Khorshidi, A. Honarbakhsh Raouf. Materials Science and Engineering A, 2011, 528: 4337- 4342.
[10] Q. D. Qin, Y. G. Zhao, W. Zhou, P. J. Cong. Materials Science and Engineering A, 2007, 447: 186-191.
[11] Q. D. Qin, Y. G. Zhao, C. Liu, P. J. Cong, W. Zhou. Journal of Alloys and Compounds, 2008, 454: 142-146.
[12] Q. C. Jiang, H. Y. Wang, Y. Wang, Y. Wang, B. X. Ma, J. G. Wang. Materials Science and Engineering A, 2005, 392: 130-135.
[13] A. Srinivasan, S. Ningshen, U. K. Mudali, U. T. S. Pillai, B. C. Pai. Intermetallics, 2006, 15: 1511-1517.
[14] Y. Mingbo, P. Fusheng, C. Renju, S. Jia. Materials Science and Engineering A, 2008, 489: 413-418.
[15] H. Y. Wang, Q. C. Jiang, B. X. Ma, Y. Wang, J. G. Wang, J. B. Li. Journal of Alloys and Compounds, 2005, 387: 105-108.
[16] R. Khorshidi, A. Honarbakhsh Raouf, M. Emamy, J.Campbell. Journal of Alloys and Compounds, 2011, 509: 9026-9033.
[17] Liu. Xiang-Fa, Wu Yu-Ying, Bian Xiu-Fang. Journal of Alloys and Compounds, 2005, 391: 90-94.
[18] C. R. Ho. and B. Cantor. Acta Metallurgica et Materialia, 1995, 43 (8): 3231-3246.
[19] J. Campbell. Casting, Elsevier, New York, NY, 2003: 152-156.
[20] J. Campbell: Intrinsic and Extrinsic Metallurgy, TMS Ann. Congr., Shape casting Symp. 2009, J. Campbell, M. Tiryakioglu, and P. Crepeau, eds.; and G. Sgworth, J. jorstad, and J. Campbell: AFS Int. J. Metalcast. , 2009, 3: 65-77.
[21] C. Li, X. Liu, Y. J. Wu. Journal of Alloys and Compounds, 2008, 465: 145-150.
[22] A. Luo, M. Z. Pekguleryuz. Journal of Material Science, 1994, 29: 5259-5271.
[23] G. Y. Yuan, Z. L. Liu, Q. D. Wang, W. J. Ding. Materials Letters, 2002, 56: 53-58.
[24] Yang. Mingbo, Pan. Fusheng, Shen. Jia, Bai. Liang, Transaction of Nonferrous Metals Society of China, 2009, 19: 287-292.

[25] P. Villars, L. D. Calvert, Pearson's Handbook of Crystallographic Data for intermetallic phases, ASM International, Matarials Park, OH, 1991.
[26] L. F. Mondolfo: Aluminum Alloys: Structure and properties, Butterworths, London, 1978: 678.
[27] P. B. Crosely and L. F. Mondolfo. Modern Castings, 1966, 49: 89-100.
[28] S. Yaneva, N. Stoichev, Z. Kamenova and S. Budurov. Z. Metallkunde, 1984, 75: 395-398.
[29] Lu. Shu-Zu and A. Hellawel. Metallurgical and Materials Transactions A, 1987, 18A: 1721-1733.
[30] A. M. Samuel, F. H. Samuel and H. W. Doty. Journal of Material Science, 1996, 31: 5529-5539.

CHAPTER 7

RHEOLOGICAL BEHAVIOUR AND MICROSTRUCTURE OF SEMI-SOLID AL-SI-CU, AND AL-SI-CU-MG ALLOYS

CHAPTER 7

RHEOLOGICAL BEHAVIOUR AND MICROSTRUCTURE OF SEMI-SOLID HYPEREUTECTIC AL-SI-CU, AND AL-SI-CU-MG ALLOYS

7.1 Introduction

Hypereutectic Al-Si-Cu (A390) alloys are very interesting materials for aerospace and automotive applications due to the excellent properties such as low coefficient of thermal expansion, superior wear resistance, high strength and high hardness [1,2]. On the other hand, hypereutectic Al-Si-Cu-Mg alloys with high Mg contents have been attracting much attention as a promising lightweight material for potential applications in the automotive and aerospace industries due to their relatively low density and excellent wear resistance as compared with A390 alloy [3,4].

However, die casting of hypereutectic Al-Si-Cu alloys has always been difficult due to its high latent heat and consequent long solidification time, resulting in die wear, the segregation of massive primary particles and its unfavorable shrinkage behavior [5-6]. To produce better quality of hypereutectic Al-Si components, semi-solid metal processing may be adapted. The SEED technology is a novel rheocasting process that takes advantages of simple process step directly from liquid metal and a large capability to use all possible material sources (primary, secondary, and in particular process scrap) [7]. Such cost-effective duality makes the SEED rheocasting process attractive and it provides an alternative for conventional die casting and forging in various industrial applications. During the semi-solid slurry making, the variation of the microstructure and processability

of semi-solid slurries can be characterized by rheological tests using the viscosity as the main indicator. A lower viscosity induces better movement of the material through the die and allows intricate thin-wall near net shape components to be cast at lower applied pressures [8].

The rheological behavior of semi-solid metal is strongly dependent on the viscosity of the semi-solid billet and its importance is equivalent to that of fluidity for liquid metal [9]. Viscosity is an indication of semi-solid forming capability in filling the mold and in determining the required force for metal flow. The viscosity of semi-solid metal alloy is dependent on a number of metallurgical parameters including the solid fraction, solid particle size and morphology, particle distribution, chemical composition and pouring temperature [10]. The rheological behavior, which is generally described in term of viscosity, has been investigated using a variety of test techniques [9]. Amongst those, parallel plate compression viscometry has been extensively used to determine the viscosity of semi-solid slurries due to the simplicity of the test procedure [8,11,12]. In this technique, a semi-solid billet is compressed between two parallel plates at constant deformation rate and the apparent viscosity can be estimated by using the Newtonian or Non-Newtonian fluid models. However, the studies related to the rheocasting of hypereutectic Al-Si-Cu-Mg alloys are very scarce in the open literature. The objective of the present study was to characterize the rheological behavior of hypereutectic unrefined Al-17-Si-4Cu (A390), P-refined Al-17-Si-4Cu (A390), Al-15Si-10.5Mg-4Cu, and Al-15Si-13.5Mg-4Cu alloys alloys using parallel plate compression viscometry.

7.2 Materials and Methods

The materials used for this study were two hypereutectic A390 alloys and two Al-Si-Cu-Mg alloys. The hypereutectic A390 alloy was a commercially available material that was directly used in experiments. The Al-15Si 10.5Mg-4Cu and Al-15Si-13.5Mg-4Cu alloys were prepared in the lab using an electric resistance furnace. To refine the primary Si and Mg_2Si phases, a certain amount of Cu-8% P master alloy was added into the both alloy melts. The chemical compositions of the tested alloys are listed in Table 7.1.

Due to difficulties in semi-solid rheoforming for hypereutectic 390 alloys, a new variation of the SEED rheocasting process consisting of isothermal holding and addition of solid metal in the melt was adapted to produce semi-solid slurries of 390 alloy [14]. For Al-15Si-10.5Mg-4Cu and Al-15Si-13.5Mg-4Cu alloys, the conventional SEED rheocasting process was used. The details of semi-solid slurry making can be found in section I and section II of Chapter 3.

Table 7.1 Alloy Codes and Compositions (wt. %)

Alloy #	Elements (wt. %)					
	Si	Mg	Cu	Fe	P	Al
1	17.1	0.55	4.5	0,4	-	Bal.
2	17.1	0.55	4.5	0,4	0,01	Bal.
3	15	10.5	4	0,4	0,4	Bal.
4	15	13.5	4.1	0,4	0,4	Bal.

The working temperatures for compression tests were 560, 558, 552 °C for the A390 alloy, 550, 548, 543 °C for the Al-15Si-10.5Mg-4Cu alloy, and 548 °C, 544 °C, 538 °C for the Al-15Si-13.5Mg-4Cu alloy, which corresponded to solid fractions of 0.4, 0.5 and 0.6 of

the studied alloys, respectively. When the melt temperature at the billet center reached to one of the working temperatures, the billet was quickly taken out of the mould and transversely sectioned at 60 mm from the bottom. The rest of the billet (75 mm in diameter and about 100 mm in height) was transferred and compressed uniaxially in a parallel plate compression machine by applying different dead weights (3.7, 5.6, 8.5 and 10.5Kg which corresponded to initial pressures of 8.5, 13.5, 20.5, 25.3KPa, respectively). The details of the compression test can be found in section III of Chapter 3. The microstructure was studied using an optical microscope.

7.3 Results and discussion

7.3.1 Rheological behaviour and microstructure of semi-solid hypereutectic Al-Si-Cu 390 alloys

7.3.1.1 Cooling curve

The solidus and liquidus temperatures were determined by the thermal analysis technique (DTA). The cooling curve of A390 alloy during solidification is shown in Fig. 7.1. The A390 alloy starts to solidify from liquid to solid near 655 ^{o}C and ends process around 500 ^{o}C. As it can be seen from the cooling curve, the solidification process between liquidus and solidus has three principal recalescence points. This includes primary Si phase precipitation at 655 ^{o}C, the main eutectic reaction at 559 ^{o}C and θ-Al_2Cu intermetallic formation at 500 ^{o}C, respectively. The solid fraction as a function of temperature is also displayed in Fig. 7.1(red curve). The solid fraction curve of A390 alloy was obtained by substituting the cooling curve's first derivative, dT/dt, and zero curve data into the CA-CCA (Computer-Aided Cooling Curve Analysis) program. Fig. 7.1 shows that for A390

alloy the temperatures in the mushy zone with solid contents of 40, 50, and 60% are located at nearly 561.5, 558 and 552 °C, respectively.

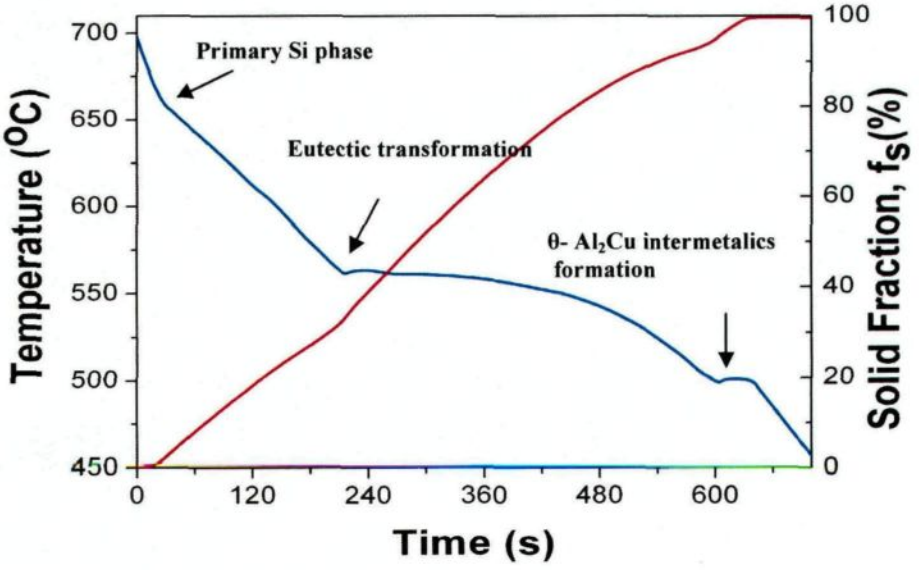

Fig. 7.1 Temperature and fraction solid versus time for A390 aluminum alloy cooled in steel mould.

7.3.1.2 Microstructure

Figure 7.2 illustrates the microstructures of the compressed specimens of the unrefined A390 alloy at different solid fractions. The micrographs shown in Fig. 7.2 are the zones in the center, middle and edge of the deformed billet. The microstructure of the unrefined A390 alloy, deformed at different temperature, consists of some primary Si particles in the matrix, surrounded by α-Al phase which preferentially formed in the liquid around the primary Si crystals. The dark particles are primary Si and the bright phase is α-Al. As shown in Fig. 7.2, when the compression test was carried out at constant strain rates, it was found that the solid particles segregate in the center portion, while the liquid is forced to the

exterior zones of the deformed billet. Fig. 7.2 shows that the degree of liquid segregation increases with increasing liquid fraction because of the lower resistance to flow of the liquid at lower solid fractions, especially at low shear rates. However at higher shear rates this segregation is reduced due to the rapid deformation. This phenomenon was also observed by Yurko and Flemings [15].

To study the effect of phosphorus addition on the microstructure, compressed specimens from the P-refined A390 alloy with 100 ppm P addition were also examined (Fig. 7.3). The microstructure is similar to that of the unrefined alloy where the primary Si particles are surrounded by spherical α-Al in the liquid matrix. However, with the addition of 100 ppm phosphorus to the melt, the primary Si particle size decreased to less than ~ 90 μm compared to ~ 120 μm in the unrefined alloy. The morphology of primary Si changed from coarse platelets with an irregular morphology in Fig. 7.2 to a fine blocky form in Fig. 7.3. Liquid segregation was also observed to increase with solid fraction in this alloy.

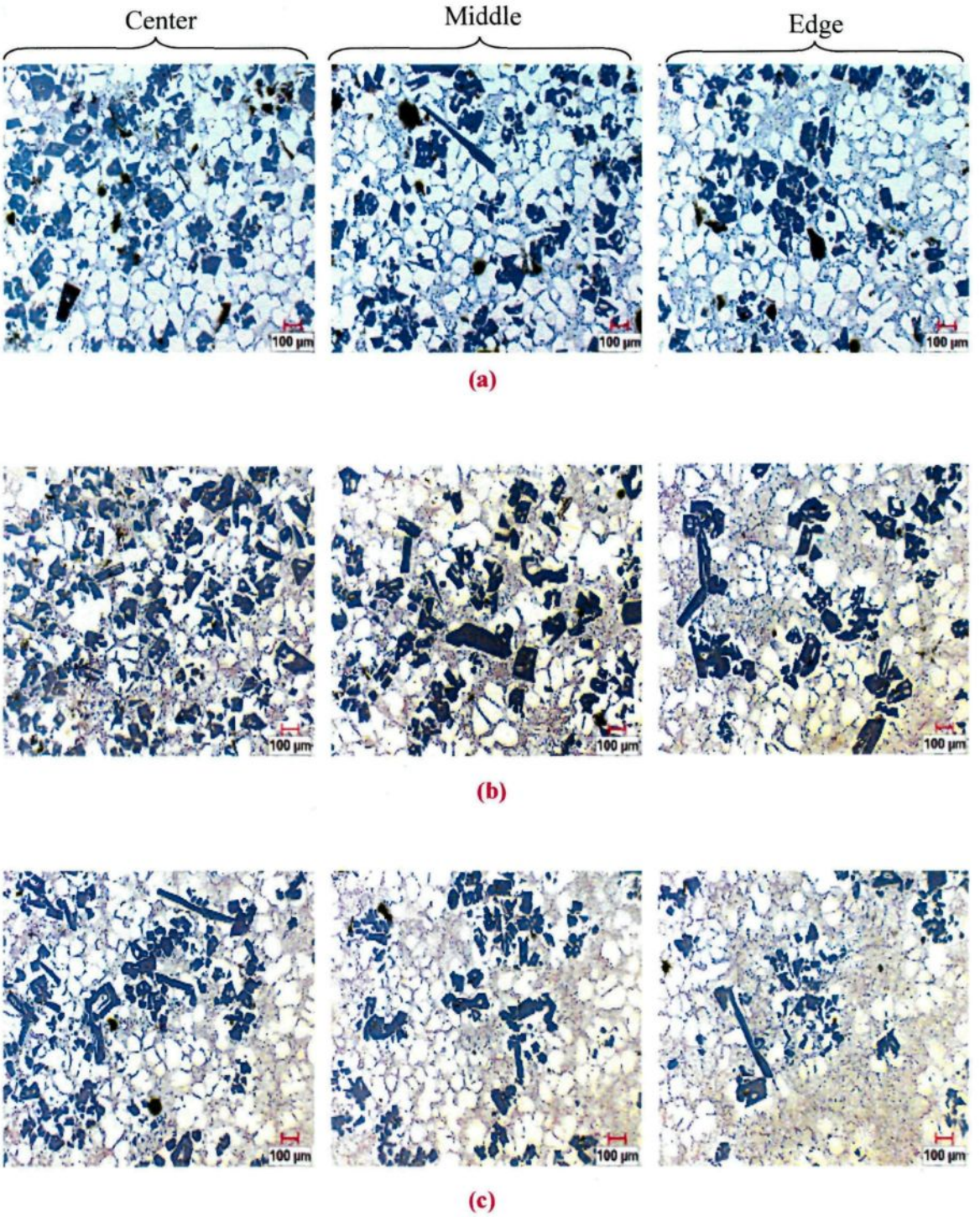

Fig. 7.2 Microstructure of unrefined A390 SSM billets from the center to the edge, deformed at different solid fractions: (a) at 0.6, (b) 0.5, (c) 0.4.

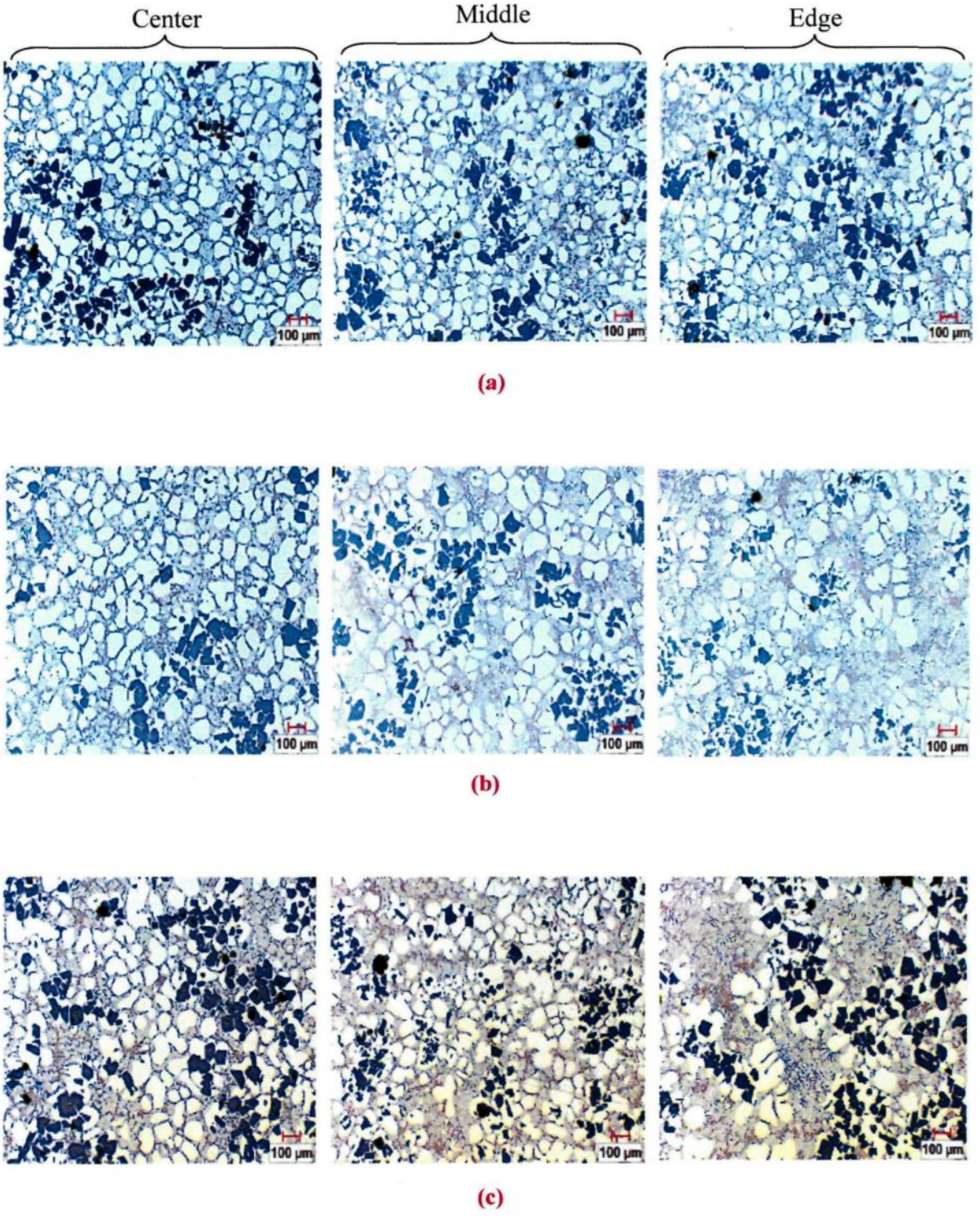

Fig. 7.3 Microstructure of P-refined A390 SSM billets from the center to the edge, deformed at different solid fractions: (a) at 0.6, (b) 0.5, (c) 0.4.

Fig. 7.4 presents the average primary Si particle area obtained for the unrefined and for the P-refined A390 alloys. Comparing the results of unrefined and refined alloys, it is seen that with addition of 100 ppm P, the particle area of the primary Si phase decreases significantly, indicating that adding 100 ppm P can effectively refine the primary Si particles.

Fig. 7.5 compares the sphericity of α-Al particles in the unrefined and P-refined A390 alloys. The primary α-Al particles are either connected with some primary Si particles or dispersed in a matrix of eutectic structure. Primary α-Al particles observed in all samples are very similar with rosette and globular forms (see Fig. 7.2 and 7.3). It can be seen in Fig. 7.5 that the addition of phosphorus did not alter the sphericity of the α-Al particles. Because the morphology and sphericity of α-Al phase in both alloys were not changed, it is believed that the primary α-Al does not have any significant impact on the apparent viscosity of semi-solid billets.

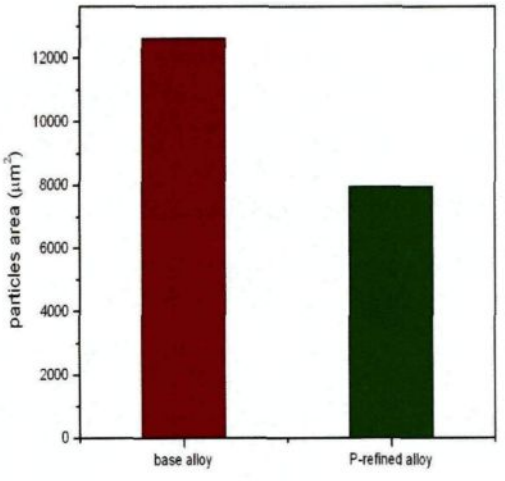

Fig. 7.4 The particles area of primary Si phase as function of phosphorus.

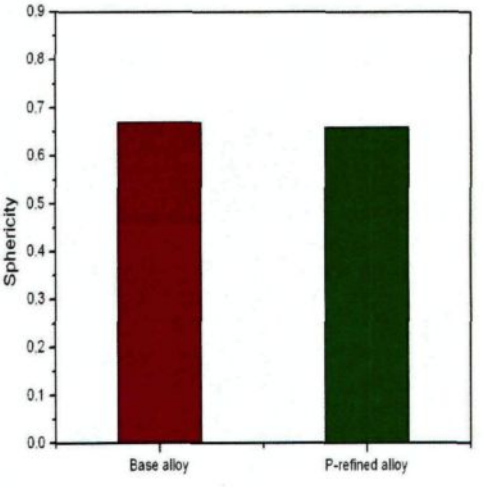

Fig. 7.5 Sphericity of α-Al particles in the unrefined and refined A390 alloys.

7.3.1.3 Engineering strain

Figure 7.6 show typical displacement-time curves obtained from the parallel plate compression tests on the unrefined A390 alloy. In this figure, the displacement has been converted into engineering strain, e, using the following equation;

$$e = 1 - \frac{h}{h_0} \qquad (7\text{-}1)$$

where h_0 and h are the initial and instantaneous heights of the specimen during compression, respectively.

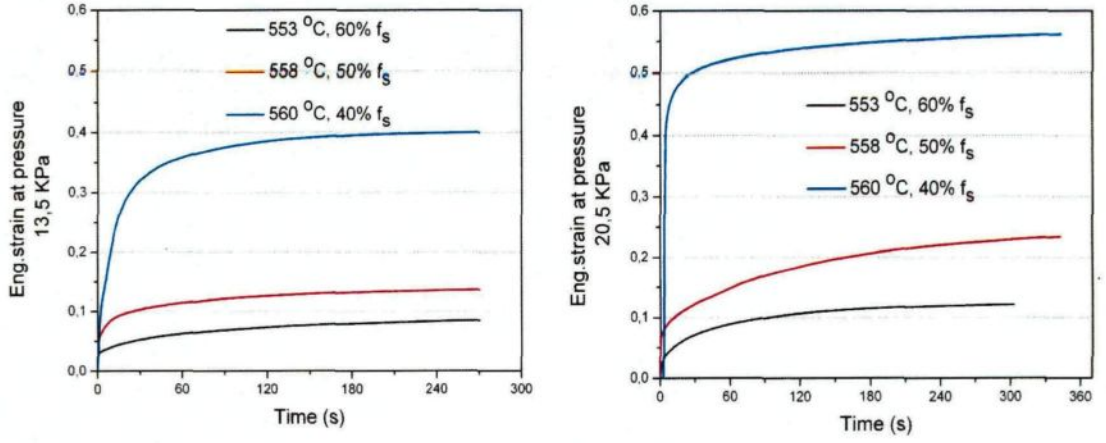

(a) (b)

Fig. 7.6 Typical engineering strain-time curves at different temperatures and pressures, (a) 13.5 KPa, (b) 20.5 KPa.

The results in Fig. 7.6 show the influence of the solid fraction and the initial pressure on the engineering strain of the unrefined A390 alloy. It can be seen that the resistance to deformation increases with increasing solid fraction, because there are more collisions between the solid particles at high solid fraction. In addition, when the initial pressure is

increased from 13.5KPa to 20.5KPa, the engineering strain for all specimens with different temperature is increased as shown in Fig. 7.6b.

7.3.1.4 Rheological analysis

The investigation of the viscosity in the semi-solid state is important to understand the rheological behavior of materials during semi-solid forming. When using parallel plate viscometry (squeezing flow) the simplest way to determine the apparent viscosity of the semi-solid material is to assume that this mixture behaves like Newtonian fluid for each increment of deformation [12]. Assuming that the shear rate value is low and does not vary appreciably within the sample during the compression test, the results can be expressed by the Stefan equation [12]:

$$F = -\frac{3\eta V^2}{2\pi h^5}\left(\frac{dh}{dt}\right) \tag{7-2}$$

The solution of Eq [7-2] was obtained by first integrating from $h = h_0$ at $t = 0$ and $h = h$ at $t = t$.

$$\frac{1}{h^4} - \frac{1}{h_0^4} = \frac{8\pi F t}{3\eta V^2} \tag{7-3}$$

$$\frac{3Vh_0}{8\pi P_0}\left(\frac{1}{h^4} - \frac{1}{h_0^4}\right) = \frac{t}{\eta} \tag{7-4}$$

The corresponding average value of the shear rate at any instant during the compression test is given by:

$$\dot{\gamma}_{av} = -\sqrt{\frac{V}{\pi}}\left(\frac{dh/dt}{2h^{2.5}}\right) \tag{7-5}$$

where η, V, h_0, h, F and t are the viscosity (Pa.s), volume of specimen (mm^3), initial height (mm), instantaneous height (mm), applied dead force (N), and deformation time (s), respectively.

A typical plot of strain-time data during the quasi steady state condition of deformation is shown in Fig. 7.7. The viscosity is calculated from the inverse slope of this plot. Table 7.2 summarizes the results of experiment data for two materials, including calculated values of apparent viscosity, temperatures, fractions solid, initial pressures and shear rates. The values of viscosity were determined from the deformation-time curves after a period of 100 seconds, when a quasi-steady state deformation regime is observed. It can be observed that before this period the deformation is highly non-linear. The values of the viscosities were calculated with error limits that were determined from the slopes at 100 seconds and at the end of the deformation.

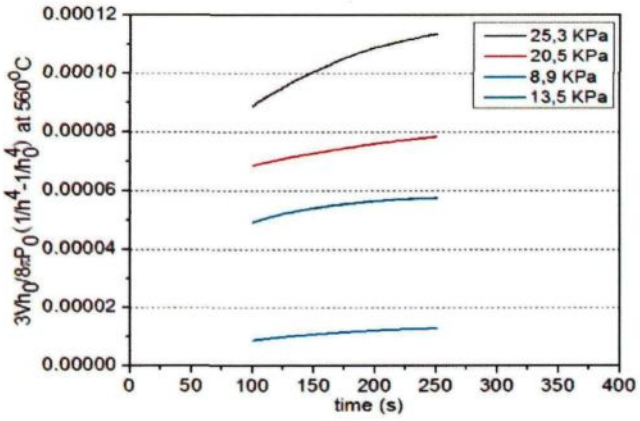

Fig. 7.7 Typical plot of [$(3Vh_0/8\pi P_0)$ $(1/h^4 - 1/h_0^4)$, Pa^{-1}], against time for the unrefined samples at 560 °C.

7.3.1.5 Effect of shear rate and solid fractions

Figure 7.8 shows the variation of the apparent viscosity as a function of shear rate and at various temperatures corresponding to various solid fractions of unrefined and refined A390 alloys, plotted in a log-log scale. Results showed a clear shear-thinning behaviour with increasing shear rate. It can be seen that the viscosity of both alloys decreases significantly with increasing shear rate for the same conditions of temperature and shear time. However, as the solid fraction increased, the viscosity of both alloys increased gradually. The shear thinning behaviour of unrefined and P-refined A390 alloys was attributed to the decrease of the agglomerate size of the solid particles by rupture of the solid bridges for increasing shear rates. This decrease of the size leads to the release of the entrapped liquid, thus reducing the viscosity. Ito *et al.* [13] have studied the effect of various shear rates on the rheology behaviour of Al-Si alloys. The authors confirmed that the concept of agglomerated particles is completely justified through metallographic observations. In fact, solid bridges can easily form between particles producing a low angle boundary, which is not wetted by the liquid. However, when the shear rate increases, the bridge network can easily break down. As expected, the viscosity of both alloys increases with increasing solid fraction as shown in Fig. 7.8. This can be explained in terms of particle interactions. At high solid fraction, particles are unable to move large distances in the melt because particles are in contact with each other. However, as the solid fraction decreases, the reduction of the number of contacts among the particles reduces the inner friction among solid particles, resulting in the reduction of viscosity.

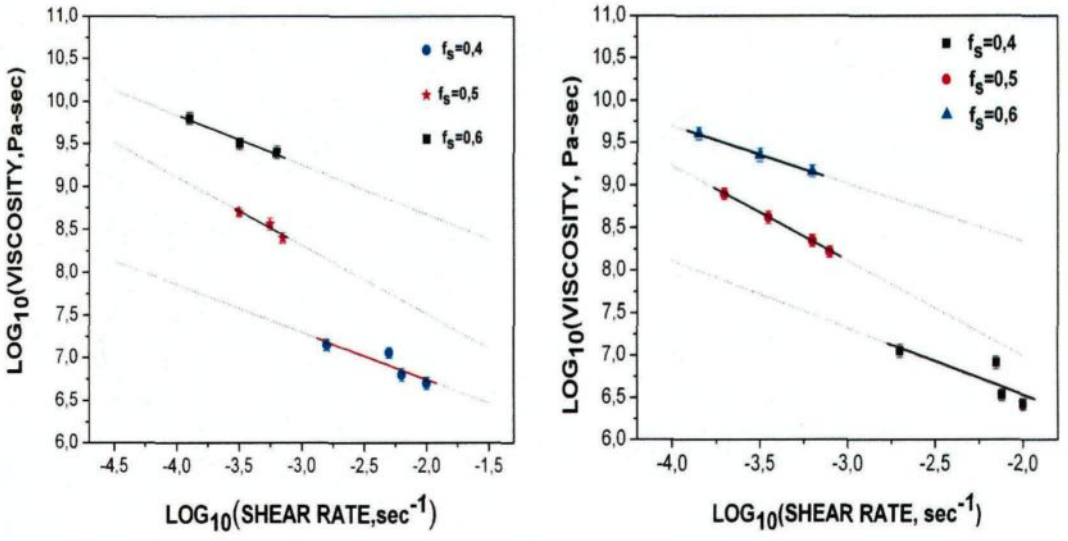

(a) (b)

Fig. 7.8 Calculated apparent viscosity against average shear rates for the unrefined and refined A390 alloys, at different initial pressures for each fraction solid: (a) unrefined alloy, (b) P-refined alloy.

7.3.1.6 Effect of P refining

The addition of P to refine primary Si particles is an important factor which influences the viscosity of semi-solid A390 alloy. Fig. 7.9 shows the variation of viscosity for unrefined and refined A390 alloys, at different temperatures corresponding to different solid fractions. The viscosity measured at a given solid fraction of the P-refined A390 alloy was orders of magnitude less than that of base A390 alloy. The P-refined alloy possesses a much smaller particle size of primary Si than the unrefined alloy as shown in Figs. 7.2 and 7.3. The superior rheological properties of the refined A390 alloy are attributed to the reduction in primary Si particle size. The addition of phosphorus results in finer primary Si, leading to more solid liquid interfacial area, where the interparticle liquid film facilitates the solid particles to slip over each other. When the particle size decreases, the interfacial

area increases which promotes particle sliding. Consequently, the small primary Si particles offer less resistance to deformation.

In addition to the particles size, the morphology of the solid grains plays an important role on the rheological behaviour of materials. Deformation is mainly brought about by grain rearrangement in equiaxed microstructures through sliding and rolling. However, microstructures consisting of dendrites or elongated grains are deformed by plastic deformation. Materials with a dendritic or elongated microstructure cannot be deformed by grain rearrangement due to the significant geometric interference of the solid phases that results in plastic deformation in the solid grains. This leads to a much higher viscosity compared to materials with an equiaxed microstructure.

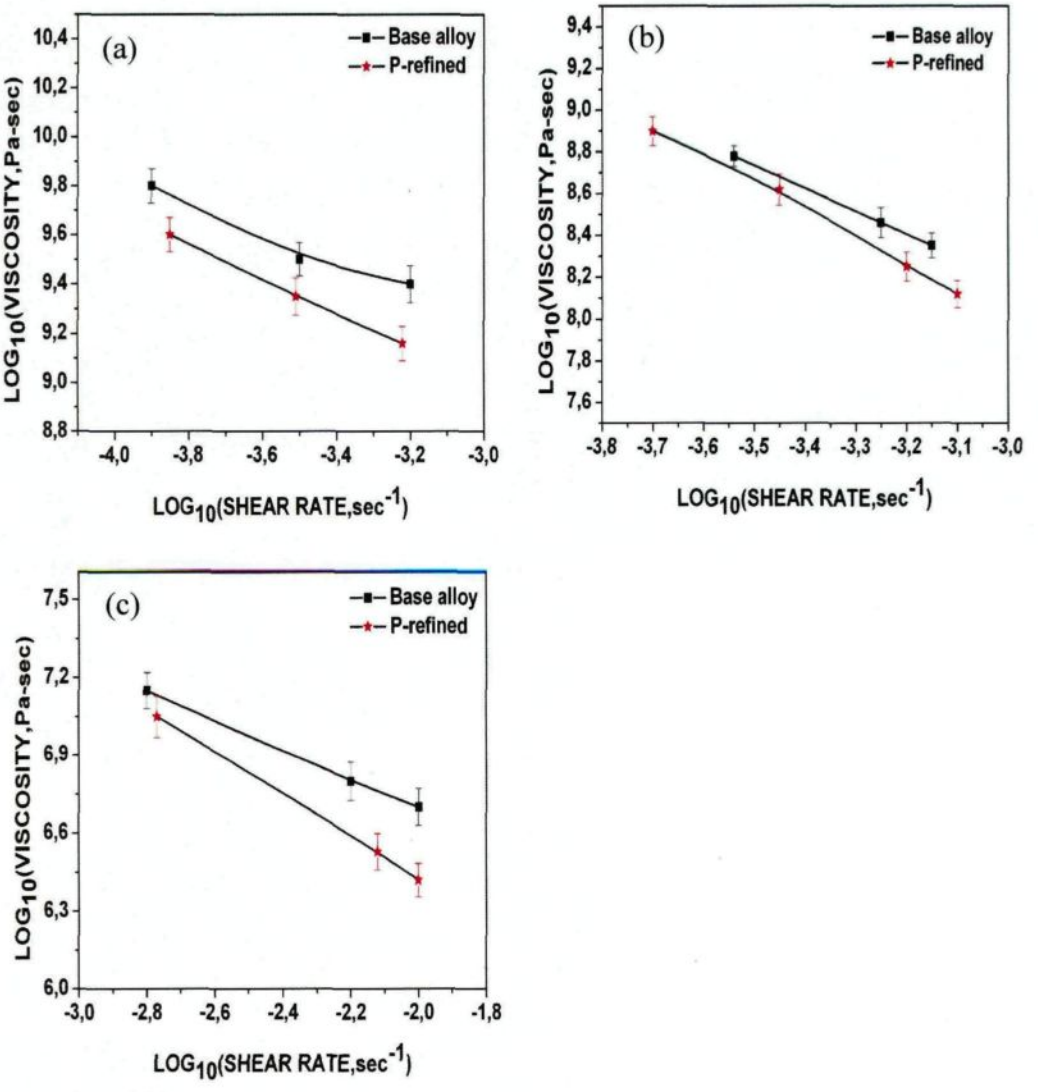

Fig.7.9 Effect of Phosphorus addition on the apparent viscostity of A390 alloy at different temperatures, (a) 552 °C, (b) 558 °C , (c) 560 °C, corresponding to solid fractions of 60 %, 50 %, and 40 % respectively.

Table.7.2: Experimental Data of unrefined and P-refined 390 alloys

Experiment Number	Temperature,°C	Fraction solid, f_s	Initial Pressure,KPa	Log $\dot{\gamma}$ s^{-1}	Log η Pa-s
Unrefined alloy					
1	552 ± 1	0.6	8.9	-	-
2	552 ± 1		13.5	-3.9	9.8 ± 0.07
3	552 ± 1		20.5	-3.5	9.51± 0.06
4	552 ± 1		25.5	-3.2	9.42 ± 0.075
5	558 ± 1	0.5	8.9	-	-
6	558 ± 1		13.5	-3.54	8.7 ± 0.05
7	558 ± 1		20.5	-3.25	8.56 ± 0.072
8	558 ± 1		25.5	-3.15	8.45 ± 0.06
9	560 ± 1	0.4	8.9	-2.8	7.15 ± 0.07
10	560 ± 1		13.5	-2.3	7.06 ± 0.05
11	560 ± 1		20.5	-2.2	6.8 ± 0.075
12	560 ± 1		25.5	-2	6.7 ± 0.07
P-refined alloy					
13	552 ± 1	0.6	8.9	-	-
14	552 ± 1		13.5	-3.85	9.6 ± 0.07
15	552 ± 1		20.5	-3.5	9.35 ± 0.075
16	552 ± 1		25.5	-3.21	9.16 ± 0.07
17	558 ± 1	0.5	8.9	-3.7	8.9 ± 0.07
18	558 ± 1		13.5	-3.45	8.62 ± 0.076
19	558 ± 1		20.5	-3.2	8.25 ± 0.074
20	558 ± 1		25.5	-3.1	8.12 ± 0.065
21	560 ± 1	0.4	8.9	-2.7	7.05 ± 0.08
22	560 ± 1		13.5	-2.15	6.91 ± 0.06
23	560 ± 1		20.5	-2.12	6.53 ± 0.07
24	560 ± 1		25.5	-2	6.42 ± 0.065

7.3.2 Rheological behaviour and microstructure of semi-solid hypereutectic Al-Si-Mg-Cu alloys

7.3.2.1 Microstructure

Figure 7.10 presents the microstructure of the compressed Al-15Si-10.5Mg-4Cu alloy which comprises many small primary Mg_2Si particles connected to some primary Si particles and α-Al grains, and the rest Al-Si eutectic matrix. It can be seen that most α-Al grains were developed in globular or rosette form. In these optical micrographs, the dark polygonal particles are primary Mg_2Si with a mean size of 50 μm, and the gray blocky particles are primary Si particles with an average size of 150 μm. The white globular particles are α-Al grains with an average size of 90 μm. Micrographs obtained from the center, middle and edge regions show that liquid segregation occurred in the compressed semi-solid billet. As the compression of billets was carried out, the solid particles (α-Al, primary Mg_2Si and Si) are compacted and collide at the center of the billet, while the residual eutectic liquid moved laterally towards the edge and accumulated at the region near the mold wall, due to the shear force imposed on the tested specimen.

On the other hand, the microstructure of Al-15Si-13.5Mg-4Cu alloy consists of a large portion of primary Mg_2Si co-existing with globular α-Al grains as shown in Figure 7.11. In these optical microimages, the dark polygonal particles are primary Mg_2Si, and the white globular particles are α-Al grains. Due to the increase in Mg content, primary Si particles disappear. Optical microstructures from the center to edge of semi-solid billets clearly indicate a liquid segregation in the compressed specimen.

A close observation of the microstructures in Fig.7.10 shows that the primary Mg_2Si particles in Al-15Si-10.5Mg-4Cu alloy did not distribute uniformly and that the primary Si particles with surrounded Mg_2Si particles had a tendency to form clusters. However, the cluster formation in Al-15Si-13.5Mg-4Cu alloy was more severe, where a number of primary Mg_2Si enclosed by α-Al grains combined together to form large clusters (Fig. 7.12). In semi-solid forming, the cluster with multi-particles will act a whole mass during the solid-liquid movement, which greatly increases the resistance of fluid flow compared to individual particles. It is expected that larger clusters would have more detrimental effect on the rheological properties of semi-solid billets.

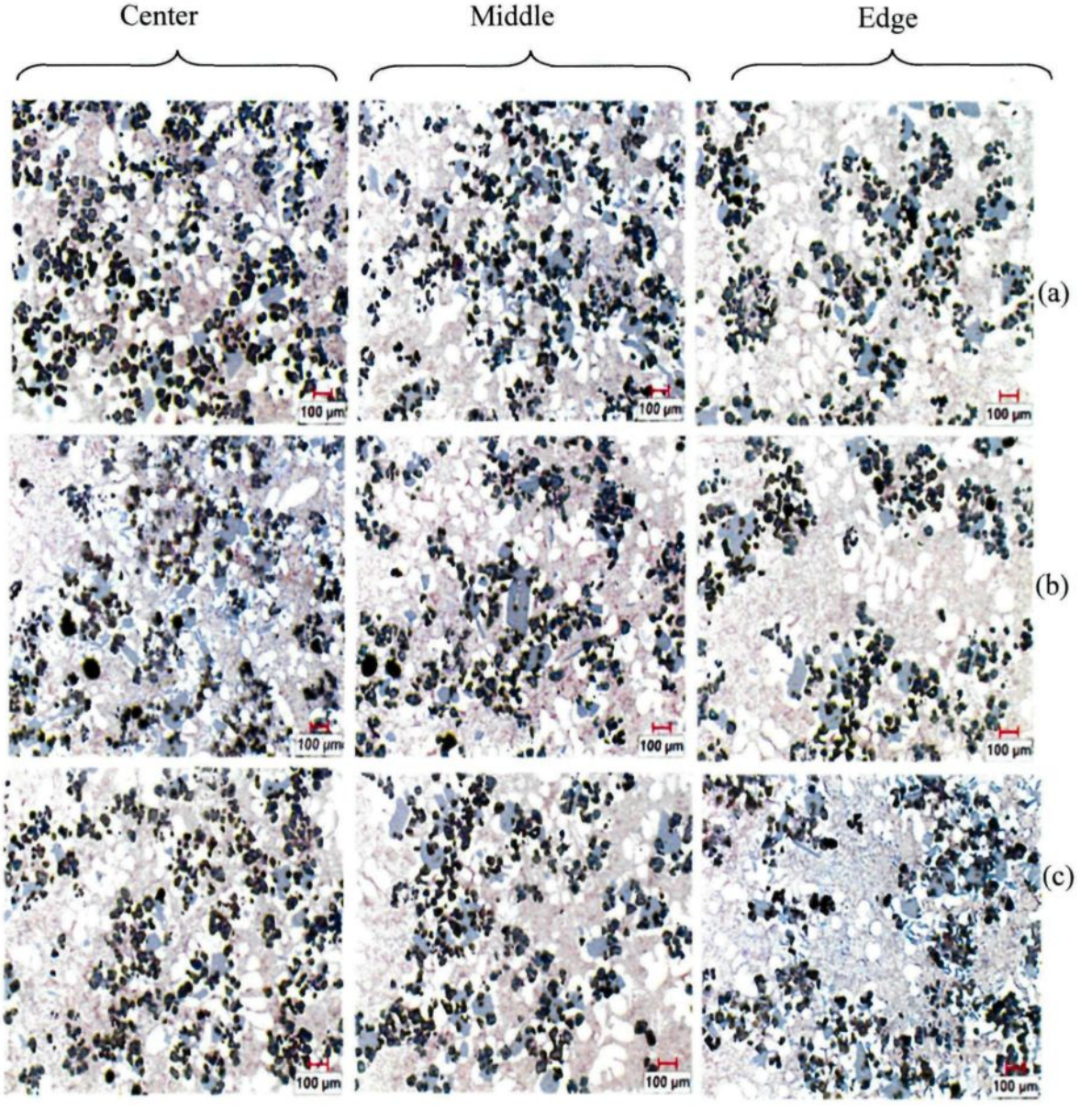

Fig. 7.10 Microstructure of Al-15Si-10.5Mg-4Cu SSM billets from the center to the wall deformed at different solid fractions: (a) at 0.6, (b) 0.5, (c) 0.4.

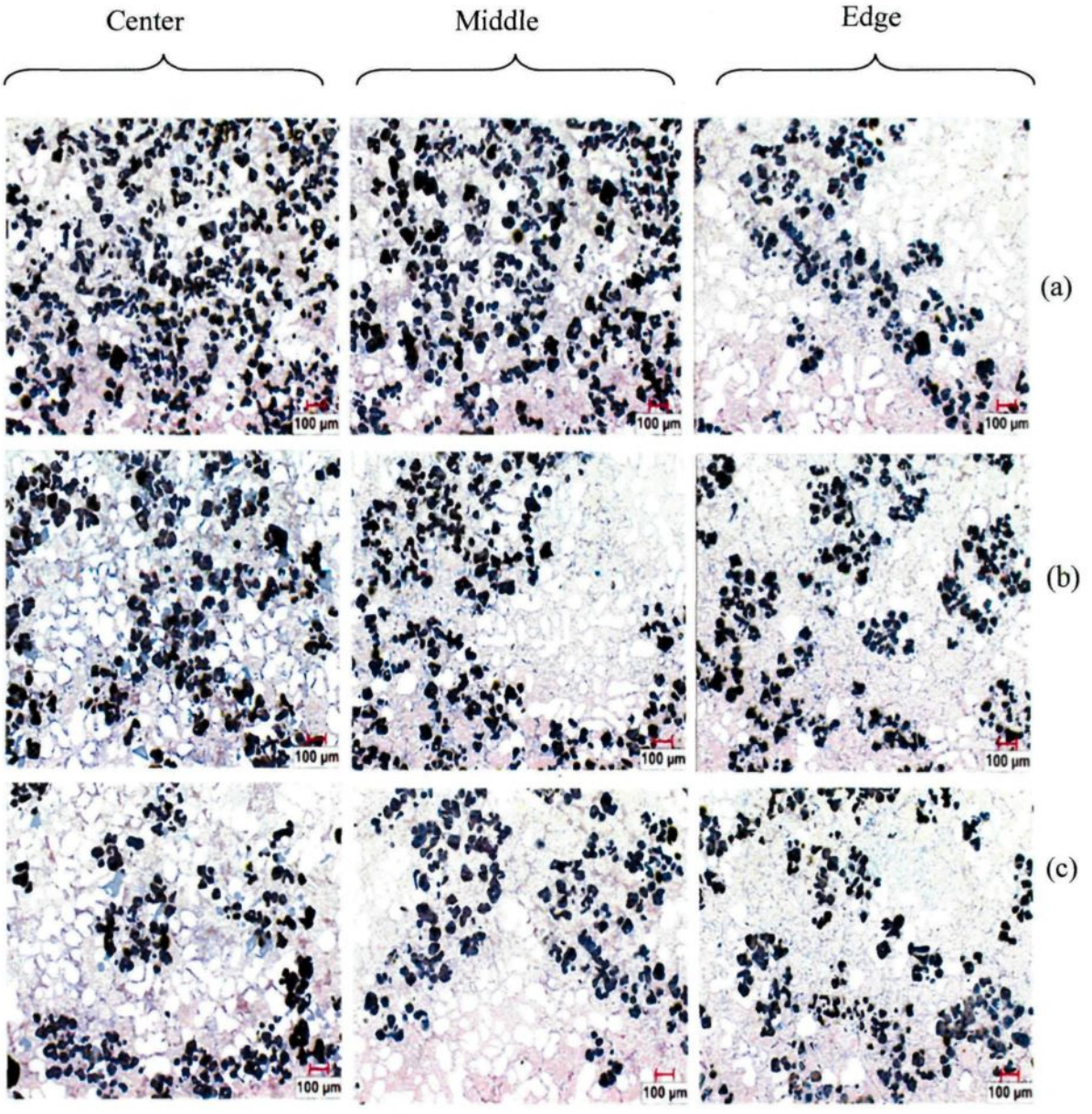

Fig. 7.11 Microstructure of Al-15Si-13.5Mg-4Cu SSM billets from the center to the wall deformed at different solid fractions: (a) at 0.6, (b) 0.5, (c) 0.4.

7.3.2.2 Engineering strain

The deformation mechanism of semi-solid alloys in parallel plate deformation includes three stages. First, during the first stage of engineering strain, the billet flow almost without any resistance to applied pressure. This is attributed to the easy movement of the primary particles within the residual liquid and without collision. The extent of this region is dependent on the particles size and applied pressure. In the second stage, there is some degree of resistance to flow due to the collision of solid particles and formation of clusters. Finally, the billet deforms steadily with a constant slope in the third stage, which means that the solid-liquid mixture has reached a state where it deforms as a single phase. The third stage or so called quasi steady state segment of the engineering strain-time graph is further developed to calculate viscosity values of the compressed specimens.

Figure 7.12, which shows the strain changes with time for the two alloys, and also illustrates the effect of solid fraction on the deformability of the billets under a given constant applied pressure. The graphs presented in Fig.7.11a and b is typical strain-time behaviour for the Al-15Si-xMg-4Cu alloys containing 10.5 and 13.5% Mg deformed at various solid fractions. The change in the billet deformability due to the Mg addition is clearly evident. Comparing the strain of the Al-15Si-10.5Mg-4Cu and Al-15Si-13.5Mg-4Cu alloys, the alloy containing 10.5% Mg deforms much more easily. Therefore, the addition of higher Mg level to the Al-15Si-xMg-4Cu alloy results in lower deformation and engineering strain in all trials.

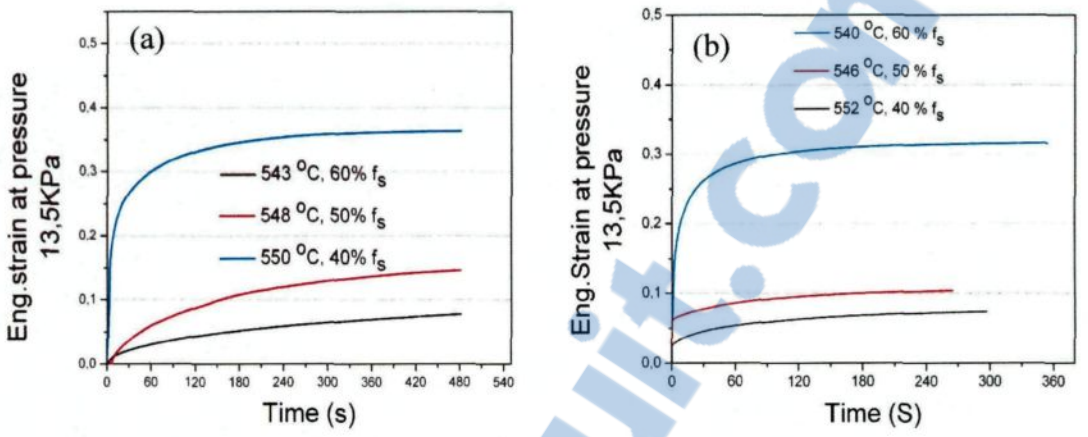

Fig.7.12 Strain-time graphs obtained at different temperatures of (a) Al-15Si-10.5Mg-4Cu alloy, and (b) Al-15Si-13.5Mg-4Cu alloy.

7.3.2.3 Rheological behavior

In addition to the effect of two different materials, two primary variables (solid fraction and shear rate) were also studied during compression experiments. Assuming the compressed specimen behaving like a Newtonian fluid, the resulting engineering strain-time data were mathematically treated to calculate the viscosity of deformed billets using a method established by Laxmanan and Flemings [12].

Figure 7.14 presents the apparent viscosity evolution for Al-15Si-13.5Mg-4Cu and Al-15Si-10.5Mg-4Cu alloys at different solid fractions and shear rates. It can be seen that the highest Mg containing alloy possesses a higher viscosity for the range of solid fractions and shear rates investigated. As shown in Fig. 7.13, the Al-15Si-13.5Mg-4Cu alloy exhibits a higher tendency to form large clusters, which can significantly increase the flow resistance. Consequently, the increase of the apparent viscosity is probably attributed to the increase the number and size of clusters in the semi-solid billets.

On the other hand, the viscosity of both alloys, at a given solid fraction, decreases remarkably with increasing shearing rate, indicating a shear thinning or so-called pseudoplastic behavior. This pseudoplastic behavior of both alloys was attributed to the decrease of the agglomerate size of the solid particles when the shear rate increases by rupture of the solid bridges between the solid particles. Figure 7.14 also demonstrates that the viscosity of both alloys increases with increasing solid fraction. At high solid fraction (Fig. 7.14a), due to the small space and large fraction between solid particles, the mechanical restraints among particles interact with each other resulting in the reduced ability of deformation. When the solid fraction decreases (Fig. 7.14 b and c), the liquid flows more freely through the inter-particles spaces. Consequently, the rotation and movement of the solid particles can take place quite freely, leading to a significant reduction of the viscosity. Table 7.3 summarizes the results of experiment data for two materials, including calculated values of apparent viscosity, temperatures, fractions solid, initial pressures and shear rates. The solid fraction of the both alloys was calculated using Scheil-Gulliver method.

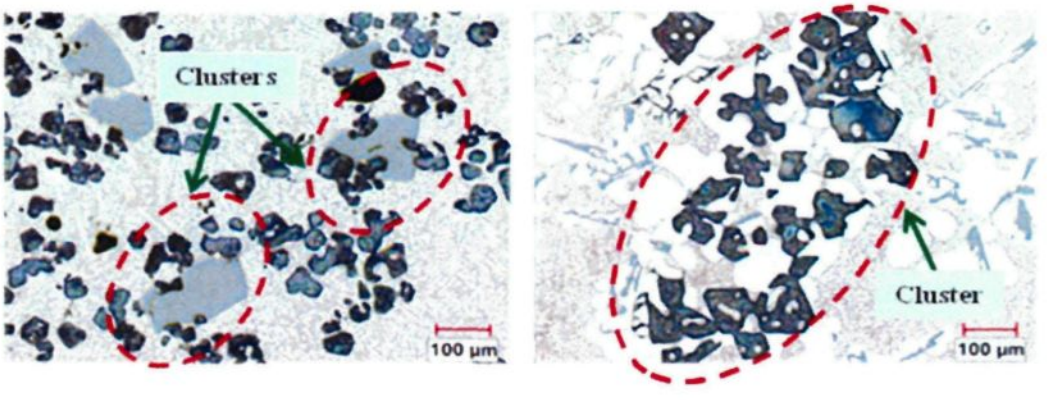

Fig. 7.13 Microstructure of deformed billets showing cluster formation, (a) alloy containing 10.5% Mg and (b) alloy containing 13.5% Mg.

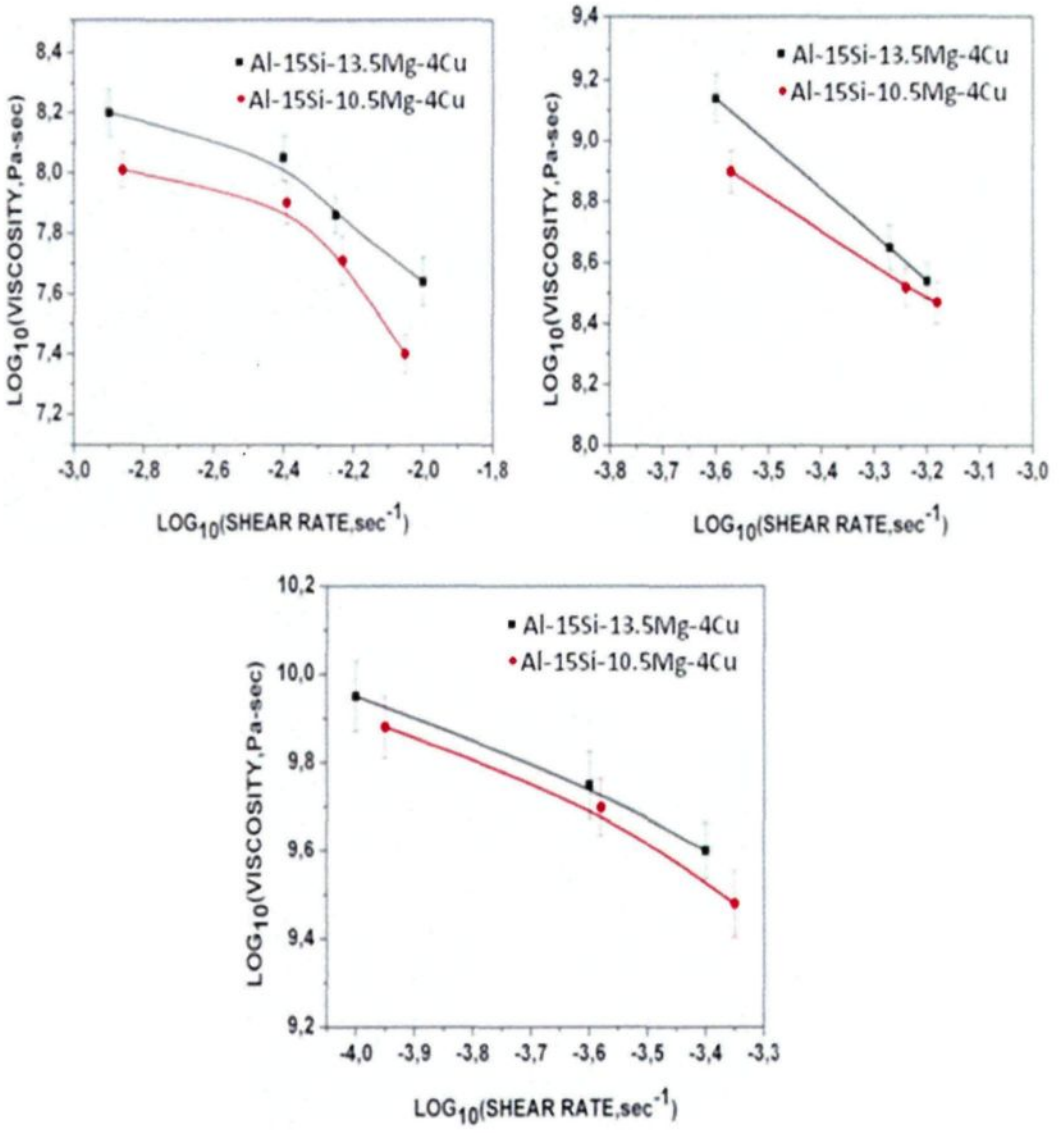

Fig. 7.14 Plots viscosity – shear rate curves of Al-15Si-10.5Mg-4Cu, and Al-15Si-13.5Mg-4Cu alloys with different solid fractions of (a) 40 %, (b) 50 %, (c) 60 %.

Table.7.3 Experimental Data of alloys containing 10.5% and 13.5% Mg

Experiment Number	Temperature,°C	Fraction solid, f_s	Initial Pressure,KPa	Log $\dot{\gamma}$ s^{-1}	Log η Pa-s
Al-15Si-13.5Mg-4Cu alloy					
1	543 ± 1	0.6	8.9	-	-
2	543 ± 1		13.5	-4	9.95 ± 0.08
3	543 ± 1		20.5	-3.6	9.75± 0.076
4	543 ± 1		25.5	-3.4	9.6 ± 0.065
5	548 ± 1	0.5	8.9	-	-
6	548 ± 1		13.5	-3.6	9.14± 0.08
7	548 ± 1		20.5	-3.27	8.65 ± 0.074
8	548 ± 1		25.5	-3.20	8.55± 0.06
9	543 ± 1	0.4	8.9	-2.9	8.2 ± 0.08
10	543 ± 1		13.5	-2.4	8.05 ± 0.075
11	543 ± 1		20.5	-2.25	7.86 ± 0.06
12	543 ± 1		25.5	-2	7.64 ± 0.08
Al-15Si-10.5Mg-4Cu alloy					
13	538 ± 1	0.6	8.9	-	-
14	538 ± 1		13.5	-3.95	9.88 ± 0.07
15	538 ± 1		20.5	-3.58	9.7 ± 0.075
16	538 ± 1		25.5	-3.35	9.48 ± 0.075
17	544 ± 1	0.5	8.9	-	-
18	544 ± 1		13.5	-3.57	8.9 ± 0.07
19	544 ± 1		20.5	-3.24	8.52 ± 0.065
20	544 ± 1		25.5	-3.18	8.47 ± 0.07
21	548 ± 1	0.4	8.9	-2.86	8.01 ± 0.06
22	548 ± 1		13.5	-2.39	7.9 ± 0.07
23	548 ± 1		20.5	-2.23	7.71 ± 0.08
24	548 ± 1		25.5	-2.05	7.4 ± 0.065

7.3.3 Discussion

7.3.3.1 Comparison of the apparent viscosity of four alloys

Figure 7.15 compares the apparent viscosity evolution of the four alloys, unrefined A390, refined A390, Al-15Si-10.5Mg-4Cu and Al-15Si-13.5Mg-4Cu alloys, at different solid fractions and shear rates. It can be seen that the high Mg containing alloy possesses a higher viscosity for the range of solid fractions and shear rates investigated. There is one order of magnitude difference between the apparent viscosity of two A390 alloys and the viscosity of the alloys containing 10.5 and 13.5 % Mg at the low solid fraction of 40% (Fig. 15a). This difference reduces remarkably with increasing solid fraction (Fig. 7.15b and c).

In A390 alloys where the size of primary silicon particles was decreased by adding grain refiner, the apparent viscosity values were found to be reduced. The unrefined structures reveal a higher apparent viscosity than grain refined alloy. Consequently, it can be concluded that the primary Si particle size has an important effect on the rheological behaviour in the semi-solid A390 alloys. In the case of Al-15Si-10.5Mg-4Cu and Al-15Si-13.5Mg-4Cu alloys, phosphorus was also added to refine the primary Mg_2Si particles. However, the apparent viscosity of the both alloys was higher than that of unrefined and refined A390 alloys. This behaviour can be attributed probably to the size of the particles agglomeration.

As shown in Fig. 7.13 the Al-15Si-13.5Mg-4Cu alloy exhibits a higher tendency to form large clusters, which can significantly increase the flow resistance. Joly *et al.* [15] have introduced the notion of liquid retention between particles. At the start of solidification

when the solid fraction is not important, the density and the average size of particles are constraints to the deformation of the slurry. However, as solidification progresses, the remaining liquid becomes less important and part of it is entrapped between coarser particles.

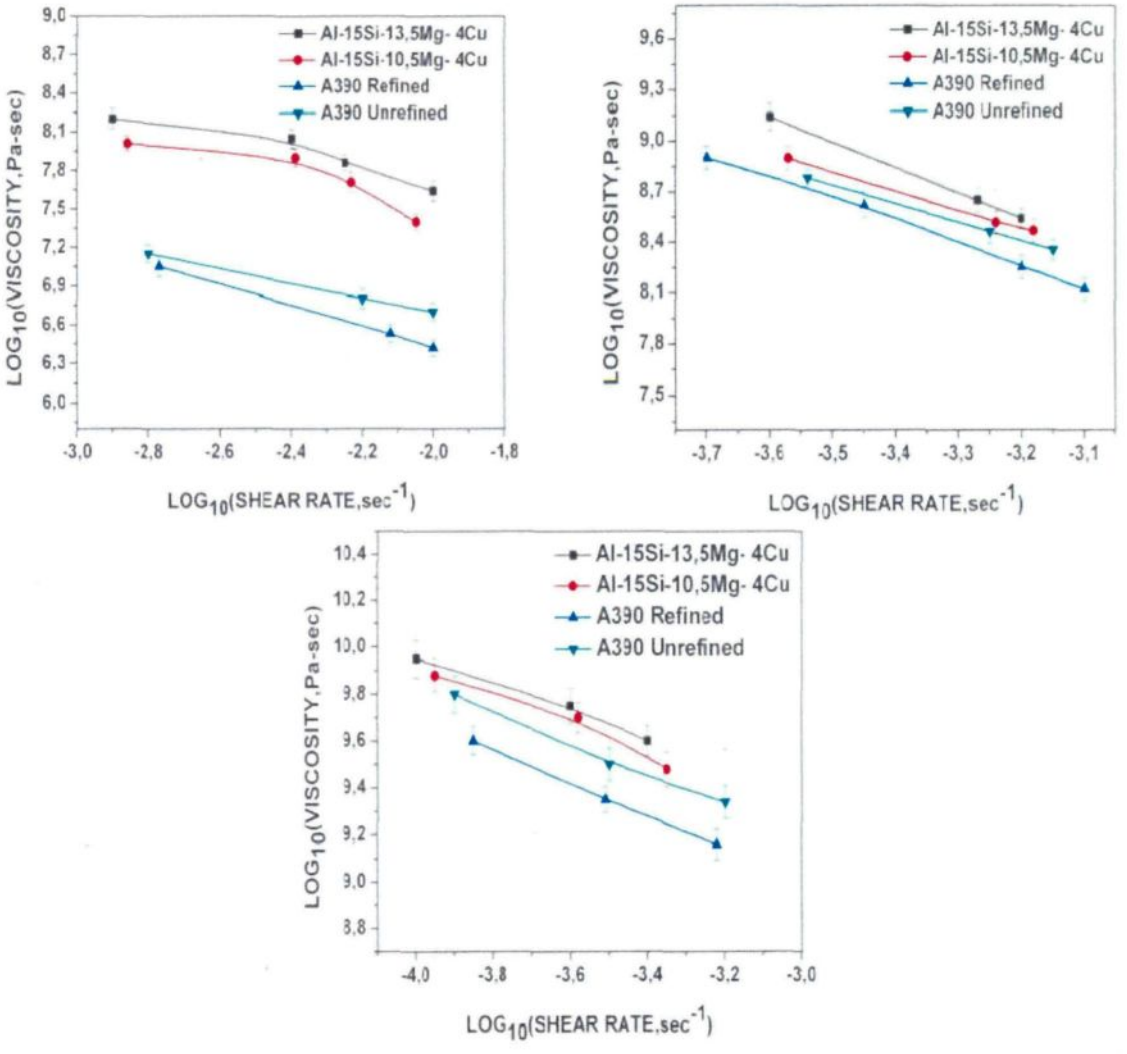

Fig. 7.15 Plots viscosity – shear rate curves of unrefined A390, refined A390, Al-15Si-10.5Mg-4Cu, and Al-15Si-13.5Mg-4Cu alloys with different solid fractions of (a) 40 %, (b) 50 %, (c) 60 %.

7.3.3.2 Quantitative characterization

Figure 7.16 shows the effective solid volume fraction of the four alloys. The effective solid volume fraction has an important effect on rheological behaviour in the semi-solid state of the rheocast products. It is well known that there is always some liquid inside the aggregates, which act the same as solid particles. Consequently, the effective solid volume fraction should be the sum of the initial solid volume fraction and the volume fraction of the liquid phase that cannot move freely inside the aggregations. It is clearly shown in Fig. 7.16 that the effective solid volume fraction increased slightly with increasing primary silicon particle size. Furthermore, addition of 10.5 % Mg or 13.5% Mg to the hypereutectic Al-Si-Cu alloys increases the effective solid volume fraction. At higher Mg content, the slurry has more and larger clusters with entrapped liquid. During the compression test these clusters would coalesce to form larger ones in which the liquid was still entrapped inside. Furthermore, the effective volume fraction of solid increases as the cluster size and volume fraction increases. Consequently, the increase in apparent viscosity as the Mg content increases is due to the increase of the cluster size and cluster volume fraction.

Figure 7.17 illustrates the particle distribution profile from the center to the wall of the deformed billets at pressure of 20.5 KPa and 50 % solid fraction. The volume fraction of solid particles (Si and α-Al in A390 alloys, Mg_2Si with Si and α-Al in Al-15Si-10.5Mg-4Cu alloy, Mg_2Si and α-Al in Al-15Si-13.5Mg-4Cu) at the edge of the specimens decreased because of liquid flow from the center to the edge of the deformed billets.

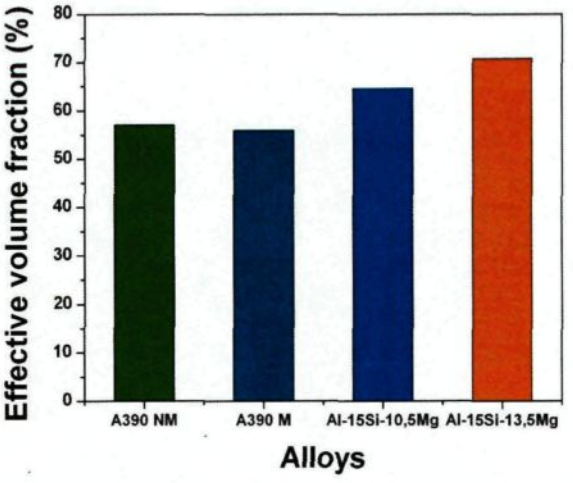

Fig. 7.16 Effective solid volume fraction of hypereutectic Al-Si-Mg-Cu SSM alloys

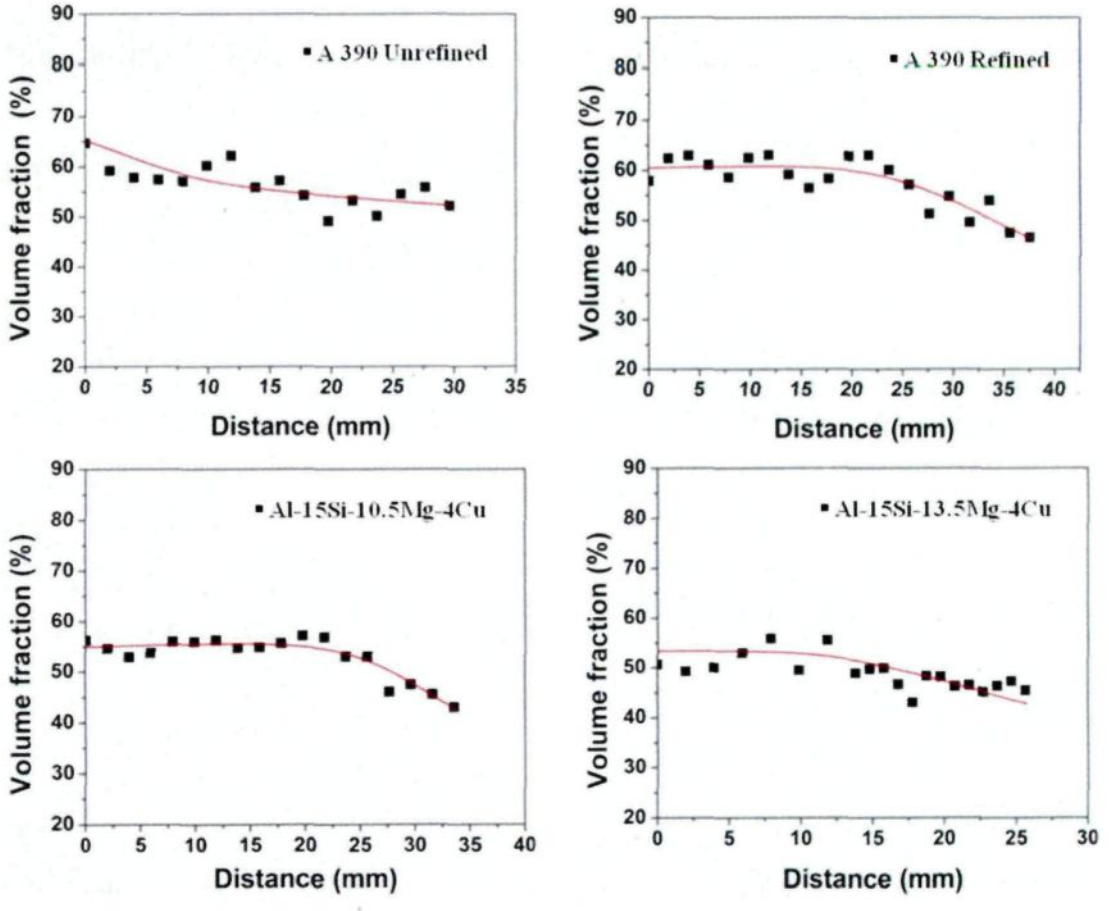

Fig. 7.17 Particles distribution profile in the four alloys obtained at 50 % solid fraction and pressure of 20.5 KPa

As observed from the microstructure, during the compression of semi-solid billets for all four alloys (Fig. 7.2, 7.3, 7.10 and 7.11), the solid particles remained in the center of the semi-solid billets, while the liquid was more or less forced to the edge of deformed billets. The image analysis results of solid particle distribution (Fig. 7.17) agree well with the above mentioned microstructural observations.

7.3.3.3 Comparison with literature

Figure 7.18 compares the apparent viscosities of both unrefined and P-refined A390 alloys in present work with those reported in the literature. It can be seen that the apparent viscosity of both alloys is higher than that found by Yurko and Flemings. [15] for A356 alloy. The large difference in apparent viscosity observed between the hypoeutectic 356 and hypereutectic 390 alloys is due to the presence of the high content of Si in the hypereutectic 390 alloys, which changes the solidification sequence and results in the formation of primary Si phase. On the other hand, it is seen from Fig. 7.18 that good agreement is observed between the results of Lashkari *et al.* [16] and the current results. In addition, Fig. 7.18 indicated that the apparent viscosity of the thixoformed 390 alloy [16] is similar to that of the rheoformed 390 alloy (present work).

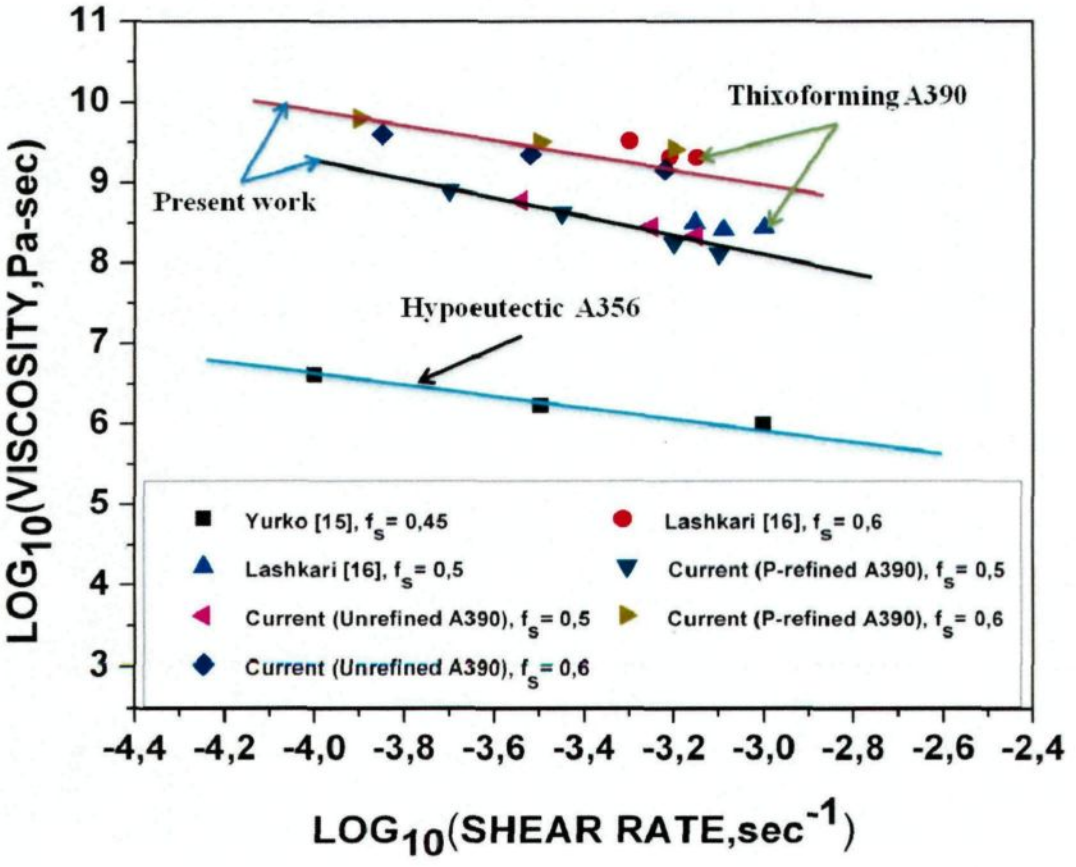

Fig. 7.18 Comparison of the apparent viscosities reported in the literature with the current results.

7.4 Summary

The effects of solid fraction, shear rate, and composition on the rheological behaviour and microstructure of hypereutectic Al-Si-Cu and Al-Si-Mg-Cu aluminum alloys were studied using compression tests. From the results obtained, the main conclusions may be summarized as follows.

1. The apparent viscosity of the four alloys (A390, P-refined A390, Al-15Si-10.5Mg-4Cu, and Al-15Si-13.5Mg-4Cu) decreases with decreasing solid fraction. Furthermore, the apparent viscosity of the four alloys decreases with increasing shear rate, indicating a shear thinning behaviour.

2. The refined A390 alloy has the lowest apparent viscosity due to the small primary particles and cluster size. The apparent viscosity increases in the order of unrefined A390, Al-15Si-10.5Mg-4Cu and Al-15Si-13.5Mg-4Cu alloys for all solid fractions and shear rates investigated.

3. The apparent viscosity is also influenced by Mg addition. For higher Mg contents, the solid particles have a tendency to form large clusters with entrapped liquid. The apparent viscosity increases as the Mg content increases.

4. A segregation phenomenon was observed in the four alloys during semi-solid deformation between parallel plates, in which the solid particles segregate in the center of semi-solid billets, while the liquid is forced to flow toward the edge of the deformed billets.

References

[1] L. Lasa, J. M. Rodriguez-Ibabe. Scripta Materialia, 2002, 46: 477-481.
[2] G. Timmermans G, L. Froyen, J. Van Humbeeck. Journal of Material Science, 2000, 35 3289-3299.
[3] A. Hekmat-Ardakan, F. Ajersch. Acta Materialia, 2010, 58: 3422-3428.
[4] A. Hekmat-Ardakan, F. Ajersch, X.-G. Chen. Wear, 2010, 269: 684-692.
[5] D. Saha, D. Apelian, R. Dadgupta. AFS Transaction, 2004, 112: 4-57.
[6] S. Midson, J. Keist, J. Svare. Semi-solid metal processing of aluminum alloy A390, in: SAE 2002 World Congress, Detroit, USA, 2002: 394.
[7] D. Doutre, J. Langlais, and S. Roy, The SEED process for semi-solid forming, In: The 8th International Conference on Semi-Solid Processing of Alloys and Composites (S2P 2004), Limassol, Cyprus, 2004: 397-408.
[8] S. Nafisi, O. Lashkari, R. Ghomashchi, F. Ajersch, A. Charette. Acta Materialia, 2006, 54: 3503-3511.
[9] O. Lashkari, R. Ghomashchi. Journal of Matererial Prococessing Technology, 2007,182: 229-240.
[10] D. Brabason, D. J. Browne, A. J. Carr. Materials Science and Engineering A, 2003, 356: 69-80.
[11] S. C. Hogg, H. V. Atkinson, P. Kapranos. Metallurgical and Materials Transaction A, 2004, 35A: 899-910.
[12] V. Laxmanan, M.C. Flemings. Metallurgical and Materials Transaction A, 1980, 11:1927-1937.
[13] Y. Ito, M. C. Flemings, J. A. Cornie. in Nature and properties of semi-solid materials, ed. By J.A. Sekhar, J. Dantzig, (The Minerals, Metals and Materials Society, Warrendale, Pa 1991: 3.
[14] P. A. Joly, R. Mehrabian. Journal of Materials Science, 1976, 11: 1393-1418.
[15] J. A. Yurko, M. C. Flemings. Metallurgical and Materials Transaction A, 2002, 33: 2737-2746.
[16] O. Lashkari, F. Ajersch, A. Charette, X.-Grant Chen. Materials Science and Engineering A, 2008, A492: 377-382.

CHAPTER 8

CONCLUSIONS AND RECOMMENDATIONS

FOR FUTURE WORK

CHAPTER 8

CONCLUSIONS AND RECOMMENDATIONS FOR FUTURE WORK

8.1 Conclusions

The results and discussion of this thesis consist of four distinct parts. The first part (Chapter 4) deals with the feasibility of semi-solid processing of hypereutectic Al-Si-Cu 390 alloys using a novel rheoforming process. In this part, a combination of the SEED process, isothermal holding using insulation and addition of solid alloy during swirling was introduced as a novel method to improve the processability of semi-solid slurry. The second part (Chapter 5) deals with the solidification and microstructural identification of hypereutectic Al-Si-Mg containing high amount of Mg. In the third part (Chapter 6), P and Sr refinement and modification effects on the microstructure of hypereutectic Al-15Si-14Mg-4Cu alloy were investigated. The fourth part (Chapter 7) deals with the effect of primary particle size and Mg addition on the rheological behaviour and microstructure of hypereutectic Al-Si-Cu and Al-Si-Mg-Cu alloys at low rates of deformation. The main conclusions drawn from each part are given below.

Part 1 Semi-solid hypereutectic Al-Si-Cu 390 alloys using rheoforming process

1. A new variation of the SEED rheocasting process, consisting of isothermal holding and addition of solid metal at the centre of the melt was developed to produce semi-solid slurries of hypereutectic Al-17Si-4Cu (A390).

2. Experiments with the above approach show that excellent microstructures of hypereutectic Al-Si-Cu A390 alloys were achieved. It was demonstrated that primary silicon particle sizes of less than 80 microns can be obtained in the alloy by addition of 100 ppm phosphor.
3. The microstructure of the semi-solid A390 alloy, produced by the new SEED rheocasting process, reveals an adequate amount of non-dendritic α-Al globules surrounded by liquid, which greatly improves the processability of the semi-solid slurries.

Part 2 Solidification and microstructure evolution of hypereutectic Al-15Si-xMg-4Cu alloy with high Mg contents

4. The effect of the addition of magnesium on the solidification behaviour and microstructure of hypereutectic Al-Si-Mg-Cu alloy was investigated using ThermoCalc software, thermal analysis and microstructure exanimation. The calculated phase diagram showed the existence of two regions separated by a critical composition at 12.52% Mg. The temperature of the liquidus, binary reaction temperatures, compositions and microstructure are dependent on the Mg content.
5. Thermodynamic calculations using ThermoCalc software revealed the occurrence of six reactions during the solidification of the Al-Si-Mg-Cu alloys investigated, comprising (i) formation of *primary* Mg_2Si, two *pre-eutectic* binary reactions which produced (ii) Mg_2Si + Si or (iii) Mg_2Si + α-Al, (iv) the *main ternary eutectic* reaction with the formation of Mg_2Si + Si + α-Al, and two

post-eutectic quaternary reactions showing the formation of (v) the Q-$Al_5Mg_8Cu_2Si_6$ phase and (vi) the θ-Al_2Cu phase.

6. Although the ThermoCalc equilibrium phase diagram predicts the formation of the θ-Al_2Cu phase only up to 7 wt% Mg levels, the use of Scheil (non-equilibrium) conditions in calculating the solidification path show the presence of the θ-Al_2Cu phase at higher Mg levels.
7. It was found that the results obtained from the thermodynamic calculation using ThermoCalc are in good agreement with thermal analysis data and the extensive microstructural observations. It was shown that the thermodynamic calculation using ThermoCalc is a useful technique that can help us to understand and predict the solidification path of a new alloy system.

Part 3 Effect of P and Sr on the microstructure of hypereutectic Al-15Si-14Mg-4Cu alloy

8. The effects of grain refiner and modifier on the Al-15Si-14Mg-4Cu alloy have been tested in this work. It was found that the mean size of primary Mg_2Si decreases from about 350 μm to less than 60 μm and the morphology changes from coarse dendritic or equiaxed to polygonal shape.
9. The morphology of the eutectic Mg_2Si phase changes from coarse Chinese script to fine fiber-like form, while that of the eutectic Si phase changes from coarse acicular shape to a fine fibrous form. With the addition of Sr or Sr + P, the morphology of π-$Al_8Mg_3FeSi_6$ phase changed from Chinese script to twin platelet shape.

10. The thermal analysis results reveal that the addition of Sr or Sr and P reduces the temperature of eutectic nucleation and growth.

Part 4 Rheological behaviour and microstructure of semi-solid hypereutectic Al-Si-Cu and Al-Si-Mg-Cu alloys

11. The rheological behaviour and microstructure were investigated using a parallel plate viscometer for the following four alloys: a) A390 alloy, b) P-refined A390 alloy, c) Al-15Si-10.5Mg-4Cu alloy, and d) Al-15Si-13.5Mg-4Cu alloy. The apparent viscosity of these slurries was dependent on the shear rate, and the volume fraction of solid, including primary Si and/or primary Mg_2Si and α-Al phases.

12. The apparent viscosity of the four alloys decreases with increasing shear rate, indicating a shear thinning behaviour. Furthermore, the viscosity of all alloys increases with an increase of solid fraction.

13. The comparison of the apparent viscosity between unrefined A390 and refined-A390 alloys indicated that the P-refined alloy has a lower viscosity for the range of shear rates and solid fractions investigated. P-refinement results in the formation of finer primary Si particles which generate in greater solid-liquid interfacial area. The inter-particle liquid film thus facilitates the solid particles to slip over each other.

14. The comparison of the apparent viscosity of the four alloys indicated that the alloy with the highest Mg content resulted in a higher apparent viscosity for the range of shear rates and solid fractions investigated.

8.2 Recommendations for future works

1. Optimization of the novel SEED process parameters (temperature of holding, swirling speed and time, holding time, weight and composition of the solid addition) to produce a semi-solid A390 alloy with superior quality structure having more globular α-Al and less segregation of Si particles.
2. Investigate the effect of semi-solid processing and grain refinement and die casting parameters on the mechanical properties of semi-solid A390 high pressure die castings using the modified rheoforming SEED process.
3. Hypereutectic Al-Si-Mg-Cu alloys with high Mg addition are considered as in-situ aluminum matrix composites containing a large amount of primary Mg_2Si particles and seem to be potential candidates to replace hypereutectic Al-Si alloys in engine block applications. It would be interesting to study the influence of the refinement of primary Mg_2Si particles and the modification of eutectic phases on the mechanical properties of hypereutectic Al-15Si-xMg-4Cu using the conventional casting method (for example, sand and permanent mold casting).
4. In this study, the rheological properties and microstructure of semi-solid Al-Si-xMg-Cu slurries have been extensively studied. For potential industrial application, it would be worthwhile to further investigate the mechanical properties of squeeze cast, new rheocast Al-15Si-xMg-4Cu alloys and to correlate these properties with the microstructure.